

Study on Intensity of Singular Stress Field at the Fiber Entry Point in Pull-Out Test and Micro- bond Test Used for Fiber Reinforced Composites

(繊維強化複合材料の引抜試験とマイクロボンド試験における繊維入口部に生じる特異応力場の強さに関する研究)

By

CHEN Dong

Department of Mechanical Engineering

Kyushu Institute of Technology

Acknowledgments

I would like to express thanks to my supervisor, Professor Nao-Aki Noda, for his constant encouragement and guidance. I am also grateful to Dr. Yoshikazu Sano, who has been giving valuable advices on my research and japanese studies.

I am thankful to Mr. Yasushi Takase, who helped me a lot.

I appreciate it very much, that Mr. Yinsa Huang picked me up from the airport and accommodate me when I arrived Japan for the first time.

I would like to express my thanks to Professor Tatsujiro MIYAZAKI from University of the Ryukyus for his helpful advice on various technical issues discussed in this study. I am also thankful to the members of our research group, Mr Rei TAKAKI, Mr Biao WANG, and Ms Akane INOUE for their generous support for this study.

I appreciate it that Prof. Taiyan Qin and Prof. Chunhui Xu taught me programming and introduced me this doctoral study experience.

I am thankful to my friends, Kejun Hu, Rong Li, Fei Ren, Guowei Zhang, Hiromasa Sakai, Xi Liu, Yunpeng Huang, Yunting Huang, Yunong Shen, Hongfang Zhai, Jian Song, Sirui Wang, Geng Gao, Zifeng Sun who helped me a lot.

Finally, I am grateful for the financial support provided by Japanese Government (Monbukagakusho: MEXT), which made it possible for my study in Japan, is gratefully acknowledged.

Abstract

Wide application of fiber composite technology in various fields is based on taking advantage of the high strength and high stiffness of fibers. In fiber composites, both the fiber and the matrix retain their original physical and chemical identities, yet together they produce a combination of mechanical properties that cannot be achieved with either of the constituents acting alone. Many different alternative test set-ups and experimental techniques have been developed in recent years to gain more insight into the basic mechanisms, dominating the properties of the fiber/matrix interface. Among these experimental tests, Pull-out test and Micro-bond test are most widely used. A lot of analytical studies have been done to clarify pull-out phenomena in pull-out test and micro-bond test, but no studies are available for the intensity of singular stress field (ISSF) at the singular points that cause crack initiation.

This intensity should be analyzed to evaluate the fiber/matrix interface properly. Previously, the finite element method and proportional method were used to evaluate the ISSF of butt joint and lap joint. These methods are used to study the ISSF in pull-out test and micro-bond test. This thesis is composed of total of 5 chapters and organized as follows.

Chapter 1, gives an introduction of the pull-out test and micro-bond test and other experiments that used to evaluate the fiber/matrix interface in composites. Also gives an introduction of the finite element method and proportional method, which are mainly used in this study. Then the research purpose of this thesis is introduced, focusing on clarification of the pull-out mechanism of the fiber/matrix interface, and analysis of the ISSFs of different geometry and material combinations in pull-out test and micro-bond test.

In Chapter 2, deals with a partially-embedded single-fiber under pull-out force in comparison with a single fiber embedded in matrix focusing on two distinct singular stress fields. Glass fiber/epoxy of pull-out test is mainly studied in this chapter. Then, the intensities of the singular stress fields (ISSFs) are compared at the fiber end named Point A* and the fiber/surface intersection named Point E*. To analyze the ISSFs accurately, a body force method (BFM) is used as the reference problem.

In Chapter 3, the intensity of singular stress field (ISSF) is analyzed at the fiber entry/exit

points in micro-bond test. The obtained ISSFs at the fiber entry point in micro-bond test are compared to the single fiber pull-out under the same fiber geometry. The results show that care should be taken for the previous micro-bond test geometry since the ISSF varies sensitively depending on the testing geometry. To control the initial fiber/matrix debonding and evaluate the bonding behavior correctly, suitable testing geometries are proposed in micro-bond testing.

In Chapter 4, ISSF of carbon fiber/epoxy is analyzed for verifying the conclusions obtained in Chapter 2 and Chapter 3. The fiber end named Point A* is easier to debond, if the bonded length is short. The fiber entry named Point E* is easier to debond, if the bonded length is long. This is same for Glass fiber/epoxy and Carbon fiber/epoxy. However, the bonded length when Point A* and Point E* is equal severe is different for different material combination. As the reference solution, a single fiber embedded in matrix is also calculated under arbitrary material combinations by using the body force method (BFM). By using this reference, the ISSFs in pull-out test is evaluated in the alpha-beta space. For Glass fiber/epoxy, the ISSF of Pull-out at Point E* is about 0.75 of that at Point E in micro-bond test. This ratio is verified for Carbon fiber/epoxy and Aramid fiber/epoxy.

Finally, Chapter 5 provides the major conclusions, the most significant outcomes and contributions and suggestions for future works.

論文要旨

繊維強化複合材料は、金属と比べて比強度が高く、価格も低いため、建設・海洋産業、航空宇宙技術・輸送分野・産業機器などに広く用いられている。強化繊維として、炭素繊維、ガラス繊維およびアラミド繊維のような非金属強化材料がよく用いられている。これら繊維強化複合材料において、強化繊維と母材間の界面強度特性が重要であるため、引抜き試験及びマイクロボンド試験が、多くの研究者に用いられており、その実験結果が議論されている。しかし、それらの試験において、界面の特異応力場には、ほとんど注意が払われておらず、繊維と母材の界面に平均応力が使用されているため、正確な議論がなされていない。したがって、そのマイクロボンド試験では、不適切と思われる試験条件が使用されており、実験結果に大きなばらつきがみられる。また、引抜き試験とマイクロボンド試験の関係が明確でなく、両者の実験結果を比較することができないなどの問題がある。

そこで、本論文では、引抜き試験とマイクロボンド試験における繊維母材間の界面に生じる特異応力場の強さ (ISSF) に注目して解析を行った。そして、ISSF に及ぼす試験寸法の影響や、二つの試験方法の関係、ならびに、設計上の指針についてまとめた。本論文は、以下の 5 つの章から構成なる。

第 1 章では、複合材料の繊維と母材の界面接着強度の評価に使用される引抜き試験とマイクロボンド試験、および関連する他の実験の概要を述べるとともに、これらの試験において繊維入口部に生じる特異応力場について説明した。その特異応力場の強さ ISSF の解析のため、本研究で使用する有限要素法 (FEM) と比例法、ならびに、ISSF に基づく接着強度の評価方法について述べた。また、引抜き試験における埋め込み端部の解析には、基準問題として 2 次元長方形介在物問題の特異応力場を用いればよいことを示した。また、引抜き試験とマイクロボンド試験における、繊維と母材の界面に生じるはく離のメカニズムや、試験寸法の影響および材料の組み合わせが異なる場合における 2 つの試験での ISSF の変化について述べた。

第 2 章では、ガラス繊維強化複合材料 (Glass/Epoxy) の引抜き試験について、繊維と母材の界面に生じる 2 つの異なる特異応力場に注目し、埋め込み端部 (点 A*) と繊維入口部 (点 E*) に生じる ISSF を比較した。点 A* と点 E* の ISSF の厳しさを比較するうえ

で、両者の特異応力場は特異性が異なるので、ISSFのみで直接比較することはできない。そこで、本論文では、繊維のはく離に最も影響すると考えられる特異点近傍の異材接合界面の、引張応力分布に注目した。点A*、E*における垂直応力で壊れやすさを比較すると繊維埋込部長さが短いとき、点A*が点E*より壊れやすく、繊維埋込部長さが長いとき、点E*が点A*より壊れやすいことを明らかにした。

第3章では、ガラス繊維強化複合材料(Glass/Epoxy)のマイクロボンド試験における、繊維退出部(点A)および繊維入口部(点E)のISSFについて述べた。マイクロボンド試験における、繊維入口部(点E)でのISSFは、同じ繊維寸法における第2章で述べている引抜試験の繊維入口部(点E*)のISSFと比較できる。その結果、埋込部長さがISSFに与える影響はマイクロボンド試験でも引抜試験と同様の傾向を示すことを明らかにした。また、引抜試験のISSFはいずれの埋込部長さにおいてもマイクロボンド試験のISSFのおよそ0.7倍の大きさとなることを示した。マイクロボンド試験におけるナイフエッジ寸法の影響について議論した結果、マイクロボンド試験のISSFはこの寸法によって敏感に変化することと、多くのマイクロボンド試験で不適切な試験寸法が採用されていることを指摘した。試験の際に繊維と母材のはく離を制御し結合挙動を正しく評価するために、マイクロボンド試験における適切な試験寸法を提案した。

第4章では、ガラス繊維強化複合材料で得られた結論が他の強化繊維でも成り立つか検証した。具体的には、任意の材料組合せに対して繊維入口部に生じる特異応力場の強さを求めるための基準問題とISSF解析の手順を示した。そして、炭素繊維強化複合材料(Carbon/Epoxy)やアラミド繊維強化複合材料(Aramid/Epoxy)等におけるISSFを検討した。その結果、これらの材料組み合わせにおいてもガラス繊維強化複合材料(Glass/Epoxy)と同様のナイフエッジ寸法の影響が現れることを示した。さらに、マイクロボンド試験と引抜試験の関係についての議論を行っており、たとえば、炭素繊維強化複合材料(Carbon/Epoxy)の場合、引抜試験のISSFはマイクロボンド試験のISSFの約0.60倍となることを明らかにした。

第5章は総括であり、本研究で得られた主要な結論を要約した。

Contents

Acknowledgments	i
Abstract	ii
論文要旨	iv
Contents	vi
Nomenclature	viii
Chapter 1 Introduction.....	1
1.1 Research Backgrounds	1
1.2 Intensity of singular stress field (ISSF)	4
1.3 Proportional method by using finite element method (FEM).....	5
1.4 Reference Solution Obtained by Using Reciprocal Work Contour Integral Method (RWCIM).....	6
Chapter 2. Intensity of Singular Stress Field in Pull-out test.	9
2.1 Introduction	9
2.2 Singular stress fields and the ISSF at the fiber end	11
2.3 Singular stress field and the ISSF at the fiber entry point	18
2.4. Results and discussion.	24
2.5. Conclusions	30
Chapter 3 Intensity of Singular Stress Field in Micro-bond Test.	32
3.1 Introduction	32
3.2. Modelling to analyze intensity of singular stress filed (ISSF)	34

3.3. Results and Discussion	38
3.4. Conclusions	47
Appendix 3.A: Modelling of a single fiber pull-out embedded in a semi-infinite region.	48
Appendix 3.B: An example of FEM mesh and stress distributions for the micro-bond test.	48
Chapter 4 Material Combination Effects on ISSFs in Pull-out Test and Micro-bond Test..	52
4.1 Carbon fiber/Epoxy vs. Glass fiber/Epoxy.....	52
4.1 ISSF at Point A in pull-out test	52
4.2 ISSF at Point E in Pull-out test.....	55
4.3 ISSF in micro-bond test for Carbon fiber/Epoxy in comparison with Glass fiber/Epoxy	60
4.4 ISSFs under Arbitrary Material Combination for a Single Rectangle Fiber in an Infinite Plate Subjected to Remote Tension.....	63
4.5 ISSFs under Arbitrary Material Combination for a Single Fiber Subjected to Pull- out Force from a Semi-Infinite Plate	66
4.6 Conclusions	69
Chapter 5 Conclusions.....	70
Reference.....	72

Nomenclature

FEM	Finite element method
ISSF	Intensity of singular stress field
IFSS	Interfacial shear strength based on average shear stress
Point A	Fiber exit point for micro-bond test
Point E	Fiber entry point for micro-bond test
Point A*	Fiber buried end for pull-out test
Point E*	Fiber entry point for pull-out test
l_M	Size of the matrix for pull-out test
l_b, l_{in}	Fiber bonded length
l_g	Knife gap opening
D	Width of the fiber in 2D analysis, fixed as $D = 20\mu\text{m}$
P	Total pull-force on the free end of fiber
θ_C	Contact angle of matrix and fiber
r_i	Distance from Point i ($i = A, E, E^*$) along the interface
E_F	Young's modulus of fiber
E_M	Young's modulus of matrix and droplet
ν_F	Poisson's ratio of fiber
ν_M	Poisson's ratio of matrix and droplet
G_F	Shear modulus of fiber
G_M	Shear modulus of matrix and droplet
α, β	Dundurs' parameters
$\lambda, \lambda_1, \lambda_2$	Singular index
σ_x^i	Stress in the x -direction at Point i ($i = A, E, E^*$)
$\sigma_{x,FEM}^i(r_i)$	Stress distribution along r_i in FEM analysis.
K_{σ,λ_1}^i	ISSF at Point i ($i = A, E, E^*$) corresponding to λ_1
K_{σ,λ_2}^i	ISSF at Point i ($i = A, E, E^*$) corresponding to λ_2
K_{σ}^i	ISSF at Point i ($i = A, E, E^*$)
e_{min}	Minimum element size in FEM modelling
$\Delta\theta_C$	Change of θ_C after deformation
$u_y^i(0)$	Displacement in the y -direction at Point i
x	Distance from Point i the x -direction along the surface
$u_y^i(x)$	Displacement in the y -direction along the surface from Point i

Chapter 1 Introduction

1.1 Research Backgrounds

Wide application of fiber composite technology in various fields is based on taking advantage of the high strength and high stiffness of fibers. In fiber composites, both the fiber and the matrix retain their original physical and chemical identities, yet together they produce a combination of mechanical properties that cannot be achieved with either of the constituents acting alone ^{1),2)}. As shown in Fig. 1.1(a) is a typical structure of fiber reinforced composite (FRC). Fig. 1.1(b) illustrate a typical fault that will appear in the FRC and influence the quality of FRC.

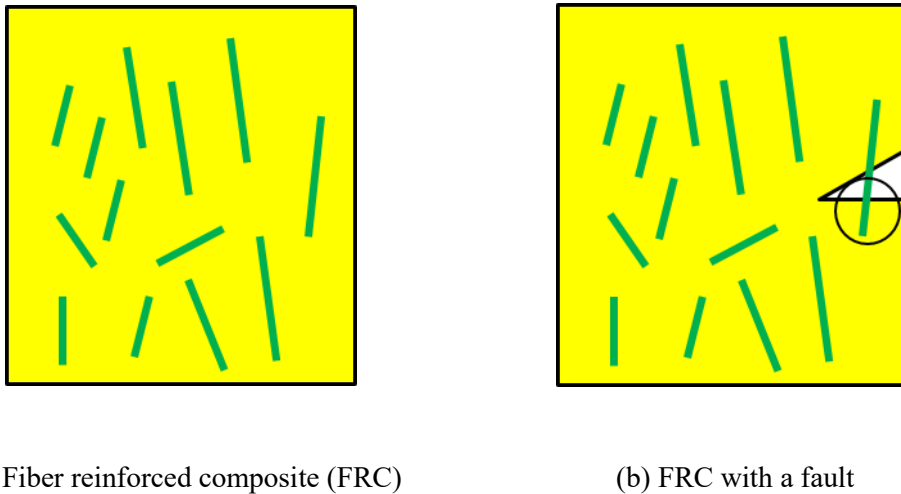


Fig. 1.1 Schematic of fiber reinforced composite

Many different alternative test set-ups and experimental techniques have been developed in recent years to gain more insight into the basic mechanisms, dominating the properties of the fiber/matrix interface. One of the most popular is the pull-out test as shown in Fig. 1.2. The other one is micro-bond test as shown in Fig. 1.3. These test methods are very useful to evaluate the quality of the FRC.

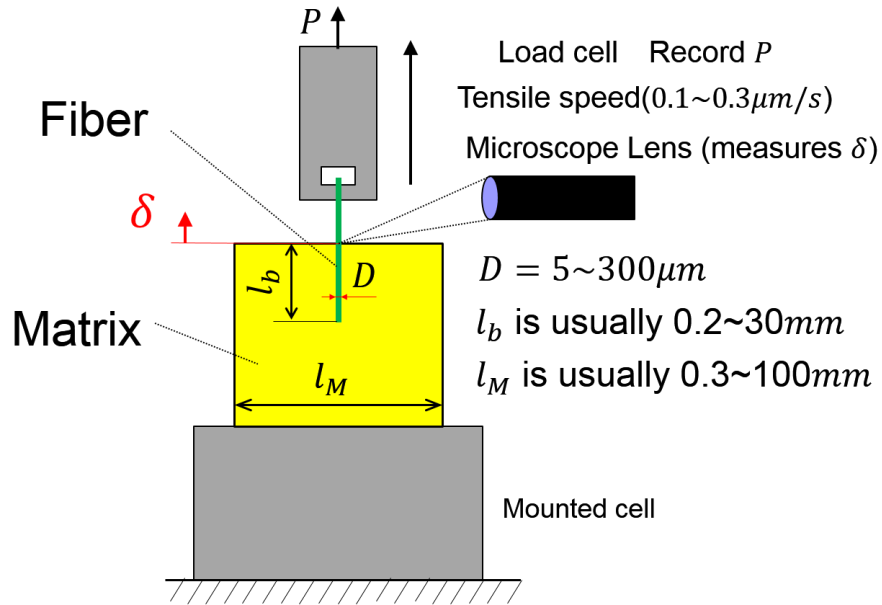


Fig. 1.2 Schematic of pull-out test

In the pull-out test, a single fiber or bar partially embedded in resin is pulled out from the surrounding matrix and the corresponding relation between load $P(\delta)$ and displacement δ is recorded³⁾. Typical relation between the pull-out load vs. displacement contains three typical zones, that is, linear elastic zone, crack extension zone and fiber extruding zone⁴⁾.

The pull-out test has been used as an advantageous micromechanical test used to characterize interfacial fiber/matrix bonding. To pull out the fiber, since the debonding strength should be smaller than the tensile strength of the fiber, high adhesion systems require very small embedding lengths l_{in} ($< 100 \mu\text{m}$)²⁾. However, the small embedding lengths sometimes make the test unusable because the pull-out force has to break the adhesion at the fiber end. The effect of the embedded length on the debonding stress at the fiber end should be clarified especially in the range of short embedded length around $l_b = 5D$.

Micro-bond test as shown in Fig. 1.3 is easier to conduct compared to pull-out test. In the Preparation of the specimen, matrix is deposited on to the surface of fiber in the form of one or more discrete microdroplets. The droplets will form concentrically around the fiber in the shape of ellipsoids. And retain their shape after appropriate curing. The droplet dimensions can only be measured after cured. The bonded length l_b of fiber are dominated not only by the fiber,

but also dominated by the quantity of matrix. For Glass fiber and Carbon fiber (50~300 μm) Kevlar (50~500 μm). In micro-bond test, large bond length is difficult.

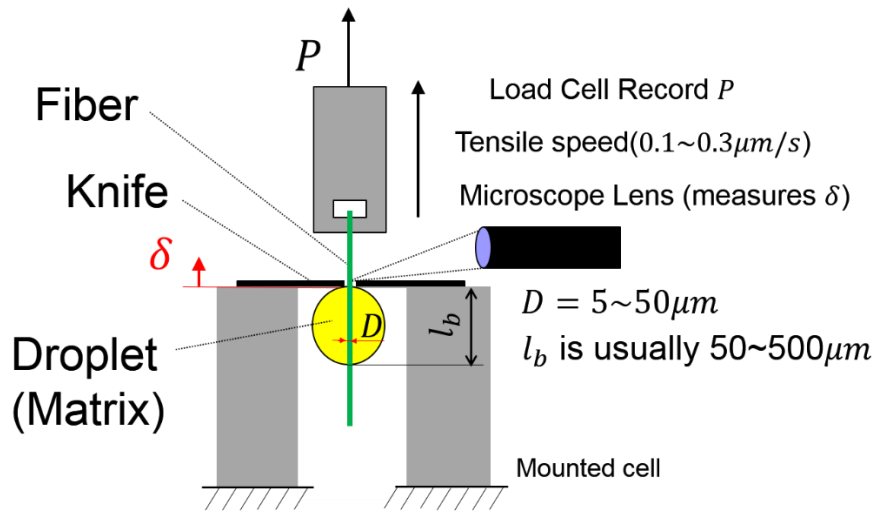


Fig. 1.3 Schematic of micro-bond test

Push out test and Fragmentation test as shown in Fig. 1.4 is also widely used in different evaluation of FRC. Push-out test are usually conducted on thin slices of unidirectional composite plates. As shown in the figure, the yellow parts represent the matrix and the green part represents fiber, the fiber is pushed out from the matrix. Fragmentation tests are usually conducted on single-filament model composites to measure the interfacial shear strength. As shown in the figure, the green parts represent fiber and the yellow part represents matrix. In this experiment, there is only one fiber or several fibers lined up in a line. The load is applied to both ends of the whole sample.

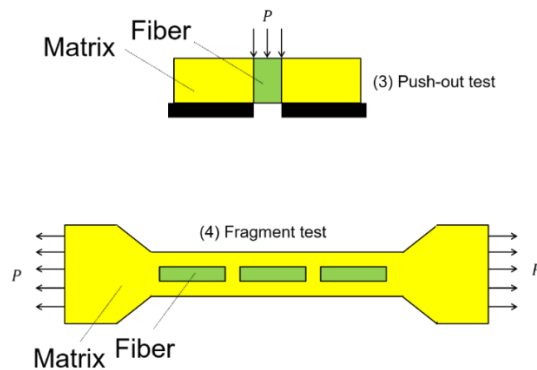


Fig. 1.4 Push-out test and fragment test.

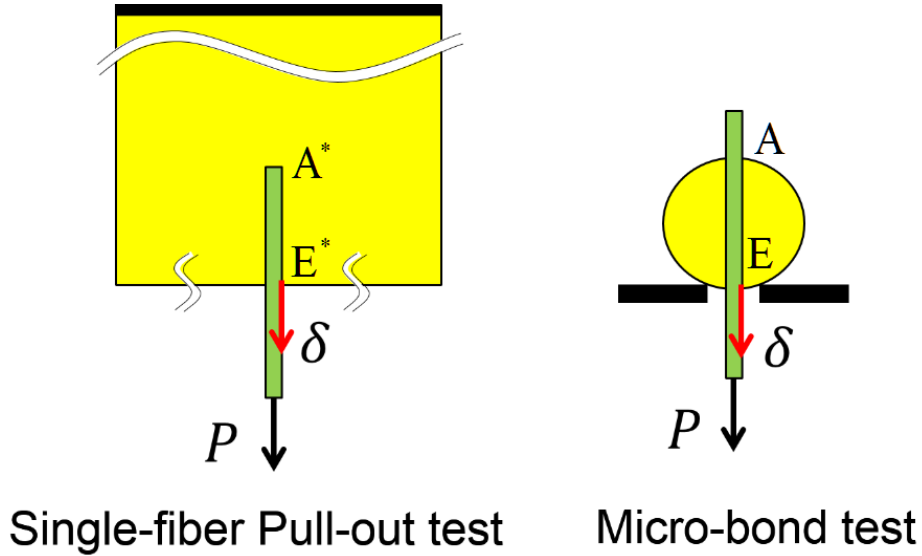


Fig. 1.5 Modelling of pull-out test and micro-bond test

The authors' recent studies have shown that the ISSFs are useful for evaluating the interface strength because they control the adhesive strength for butt and lap joints ⁵⁻¹¹). Therefore, this paper will focus on the ISSFs of a single fiber partially embedded in a matrix under pull out force by using the 2D model as shown in Fig. 1.5. Then, the effect of fiber embedded length on the ISSFs will be investigated and the severities at the fiber end Point A and at the fiber entry Point E will be compared by considering their fiber interface stress distributions. The final goal of this study is to clarify the fiber pull out mechanism toward designing suitable fiber reinforced composites. In this research, the intensity of singular stress fields in the pull-out test and micro-bond test will be studied.

1.2 Intensity of singular stress field (ISSF)

The normal singular stress, which may cause debonding at the entry point, can be expressed as follows: ¹²⁾

$$\sigma_x^i = \frac{K_{\sigma, \lambda_1}^i}{r_i^{1-\lambda_1}} + \frac{K_{\sigma, \lambda_2}^i}{r_i^{1-\lambda_2}}, \quad (i = A, E, E^*) \quad (1.1)$$

Here λ_1 and λ_2 are singular indexes, which can be calculated by solving the following characteristic equations ^{13),14)}. Singular indexes at Point E and Point E* in Fig. 1.5 are same,

but singular indexes at Point A and Point A* in Fig. 1.5 are different. In micro-bond test, Point A and Point E have same singular indexes. Therefore, the ISSFs at Point A, Point E and Point E* can be compared. But they cannot be directly compared with Point A*.

$$\begin{aligned}
 & 4\sin^2(\pi\lambda)\left\{\sin^2\left(\frac{\pi\lambda}{2}\right)-\lambda^2\right\}\beta^2+4\lambda^2\sin^2(\pi\lambda)\alpha\beta \\
 & \quad +\left\{\sin^2\left(\frac{\pi\lambda}{2}\right)-\lambda^2\right\}\alpha^2+4\lambda^2\sin^2(\pi\lambda)\beta \\
 & +2\left\{\lambda^2\cos(2\pi\lambda)+\sin^2\left(\frac{\pi\lambda}{2}\right)\cos(\pi\lambda)+\frac{1}{2}\sin^2(\pi\lambda)\right\}\alpha \\
 & \quad +\sin^2\left(\frac{3\pi\lambda}{2}\right)-\lambda^2=0
 \end{aligned} \tag{1.2}$$

Here, α , β denote bi-material parameters of Dundurs¹⁵⁾, and G_F and G_M are shear modulus, which can be transformed from Young's modulus E_F , E_M and Poisson's ratios ν_F , ν_M . Subscripts M, F represent the matrix and the reinforcing fiber, respectively. In this study, analysis is carried out under plane strain.

$$\begin{aligned}
 \alpha &= \frac{G_F(\kappa_M + 1) - G_M(\kappa_F + 1)}{G_F(\kappa_M + 1) + G_M(\kappa_F + 1)}, & \beta &= \frac{G_F(\kappa_M - 1) - G_M(\kappa_F - 1)}{G_F(\kappa_M + 1) + G_M(\kappa_F + 1)}, \\
 \kappa_i &= \begin{cases} (3 - \nu_i)/(1 + \nu_i) & (\text{Plain stress}) \\ (3 - 4\nu_i) & (\text{Plain strain}) \end{cases} \quad (i = M, F)
 \end{aligned} \tag{1.3}$$

1.3 Proportional method by using finite element method (FEM)

Finite element method (FEM) analysis should be well conducted and may require experience and skills for engineering applications¹⁶⁾⁻²⁴⁾. In this analysis, a mesh independent proportional method is used to calculate the ISSF K_σ^i defined in equation (1.1). The ISSF can be calculated from the ratio of FEM stress $\sigma_{x,i}^{FEM}(r_i)$ as shown in equation (1.4)^{12)-14),25)}.

$$\frac{K_\sigma^i}{K_\sigma^j} \cong \frac{\sigma_{x,FEM}^i(r_i)}{\sigma_{x,FEM}^j(r_j)}, \quad (i, j = A, E, E^*) \tag{1.4}$$

For example, although the stress distribution $\sigma_{x,FEM}^E(r_E)$ varies depending on the FEM

mesh size, the FEM stress ratio $\sigma_{x,FEM}^E(r_E)/\sigma_{x,FEM}^{E*}(r_{E^*})$ is almost the same independent of mesh size. This is because the same mesh pattern is applied to the singular stress region to cancel the FEM error. The FEM stress ratio can be regarded as the real stress ratio although the FEM stress cannot express the real singular stress. Since the stress ratio can be obtained accurately, the ISSF of unknown problem can be obtained from the ISSF of reference solutions with the ratio as shown in equation (1.4).

1.4 Reference Solution Obtained by Using Reciprocal Work Contour Integral Method (RWCIM)

The ISSFs $K_{\sigma,\lambda_1^E}^E, K_{\tau,\lambda_1^E}^E$ at the fiber entry Point E in pull-out can be calculated by using the proportional method explained in Section 1.3 from the FEM stress ratios as shown in equation (1.4) which is $\frac{K_{\sigma,\lambda_1^E}^E}{K_{\sigma,\lambda_1^E}^{E*}} = \frac{\sigma_{FEM,\lambda_1^E}^E}{\sigma_{FEM,\lambda_1^E}^{E*}}, \frac{K_{\sigma,\lambda_2^E}^E}{K_{\sigma,\lambda_2^E}^{E*}} = \frac{\sigma_{FEM,\lambda_2^E}^E}{\sigma_{FEM,\lambda_2^E}^{E*}}$ To obtain the reference solution $K_{\sigma,\lambda_1^E}^{E*}, K_{\tau,\lambda_1^E}^{E*}$

The RWCIM may be suitable. This method is based on the concept of Betti's Law, pioneered by Stern et al. ¹⁹⁾. Carpenter et al. ²⁶⁾ and Sinclair et al. ²⁷⁾ adapted this method to the general opening crack problem. By mean of Williams' eigenfunction expansion method, displacement and stress in the vicinity of the interface corner edge can be expressed as ^{26),28)}:

$$\sigma_{ij} = \sum_{k=1}^{\infty} K_k f_{ij}(\theta, \lambda_k) r^{\lambda_k - 1} \quad (1.5)$$

$$u_i = \sum_{k=1}^{\infty} K_k g_i(\theta, \lambda_k) r^{\lambda_k} \quad (1.6)$$

Here, λ_k is singular index obtained by solving equation (1.2) in Section 1.2. For most of the material combinations the singular indexes λ_i^E have two real roots λ_1^E and λ_2^E corresponding to two different singular fields ²⁹⁾. Here, K_k is ISSF corresponding to singular index λ_k , obtained by RWCIM discussed in this section. As shown in Fig. 1.6, symbol r is the radial distance away from Point E. Eigenfunctions f_{ij} and g_i depend on λ_k and θ . When $\theta = 0$, and use K_{σ,λ_k} to denote $K_k f_{\theta}(\theta, \lambda_k)$, equation (1.5) is expressed as equation (1.1). Denote by u_i the displacement field and σ_{ij} the traction vector on a contour $C = C_1 + C_2 + C_3 + C_4 + C_5 + C_6 + C_\varepsilon$, as shown in Fig. 1.6, equation (1.7) ²⁶⁾ is obtained from Betti's Law:

$$\oint_C (\sigma_{ij} u_i^* - \sigma_{ij}^* u_i) ds = 0. \quad (1.7)$$

Here, u_i^* and σ_{ij}^* correspond to any other such solution. Contour C_ε is a three-quarter circle contour with a radius ε . Separate the contour into C_ε and $C_R = C_1 + C_2 + C_3 + C_4 + C_5 + C_6$, equation (1.7) becomes ³⁰⁾:

$$I_\varepsilon = \int_{C_\varepsilon} (\sigma_{ij} u_i^* - \sigma_{ij}^* u_i) ds = - \int_{C_R} (\sigma_{ij} u_i^* - \sigma_{ij}^* u_i) ds. \quad (1.8)$$

Then, the integral I_ε can be calculated from the path independent contour C_R , without need for accurate data in the vicinity of the Point E in FEM calculation. ISSF K_k corresponding to singular index λ_k can then be obtained. Combined with f_{ij} for σ and τ respectively, expressed as $K_{\sigma, \lambda_1^E}^E, K_{\sigma, \lambda_2^E}^E, K_{\tau, \lambda_1^E}^E, K_{\tau, \lambda_2^E}^E$. Worth mentioning that, for the integral path C shown in Fig.1.6, contours C_1 and C_2 locate along the stress-free surface, and therefore, the integrals along these contours are zero.

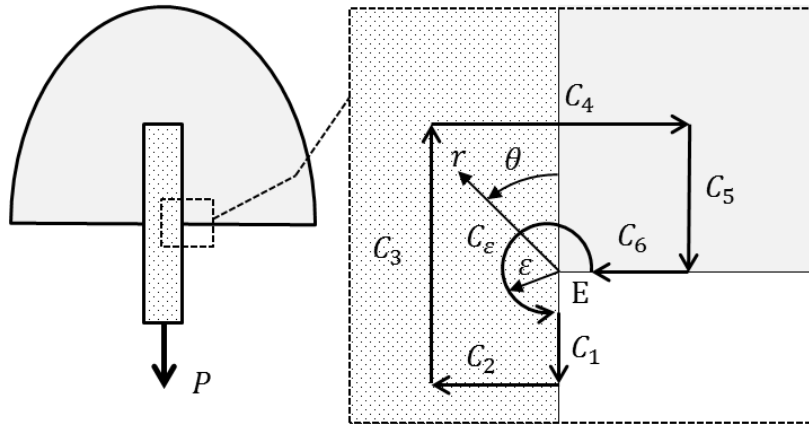


Fig. 1.6. Integral path C for RWCIM ($C = C_1 + C_2 + C_3 + C_4 + C_5 + C_6$).

Plane strain condition is selected for carrying out the linear elastic analyses in MSC Marc software. Around the interface corner edge eight-node elements are utilized, while for other regions away from the interface corner edge, four-node elements are selected.

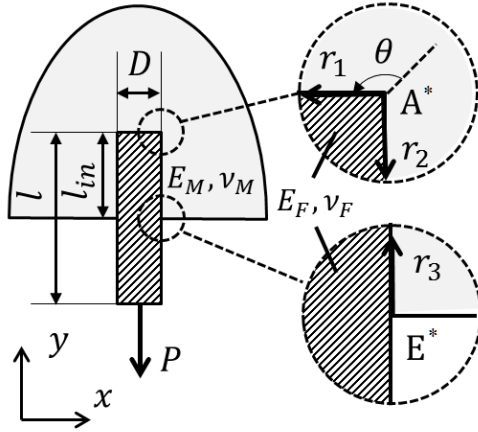
RWCIM can be used to provide the reference ISSFs. However, RWCIM requires a large number of calculations for complex operations with matrix as well as numerical integrations

Chapter 1

along the path. The proportional method in Section 1.3 to calculate the ISSFs (from a reference solution of the ISSF) is just as accurate as the RWCIM, when calculating the first term, being more convenient and practical. In this method, comparison between two models can be made from the FEM stress ratios, easily.

Chapter 2. Intensity of Singular Stress Field in Pull-out test.

2.1 Introduction

$$\begin{cases} \sigma_y^{A^*}(r_1) = \frac{K_{\sigma, \lambda_1^{A^*}}^{A^*}}{r_1^{1-\lambda_1^{A^*}}} + \frac{K_{\sigma, \lambda_2^{A^*}}^{A^*}}{r_1^{1-\lambda_2^{A^*}}} \\ \tau_{yx}^{A^*}(r_1) = \frac{K_{\tau, \lambda_1^{A^*}}^{A^*}}{r_1^{1-\lambda_1^{A^*}}} + \frac{K_{\tau, \lambda_2^{A^*}}^{A^*}}{r_1^{1-\lambda_2^{A^*}}} \end{cases} \quad \begin{cases} \sigma_x^{A^*}(r_2) = \frac{K_{\sigma, \lambda_1^{A^*}}^{A^*}}{r_2^{1-\lambda_1^{A^*}}} - \frac{K_{\sigma, \lambda_2^{A^*}}^{A^*}}{r_2^{1-\lambda_2^{A^*}}} \\ \tau_{xy}^{A^*}(r_2) = \frac{K_{\tau, \lambda_1^{A^*}}^{A^*}}{r_2^{1-\lambda_1^{A^*}}} - \frac{K_{\tau, \lambda_2^{A^*}}^{A^*}}{r_2^{1-\lambda_2^{A^*}}} \end{cases}$$


$$\begin{cases} \sigma_x^{E^*}(r_3) = \frac{K_{\sigma, \lambda_1^{E^*}}^{E^*}}{r_3^{1-\lambda_1^{E^*}}} + \frac{K_{\sigma, \lambda_2^{E^*}}^{E^*}}{r_3^{1-\lambda_2^{E^*}}} \\ \tau_{xy}^{E^*}(r_3) = \frac{K_{\tau, \lambda_1^{E^*}}^{E^*}}{r_3^{1-\lambda_1^{E^*}}} + \frac{K_{\tau, \lambda_2^{E^*}}^{E^*}}{r_3^{1-\lambda_2^{E^*}}} \end{cases}$$

Fig. 2.1 Two-dimensional pull-out model for partially embedded fiber with the singular stress fields along the local coordinates r_1, r_2, r_3 . The intensities of the singular stress fields

(ISSFs) are denoted by $K_{\sigma, \lambda_1^{A^*}}^{A^*}$ etc. ^{31)–33)}.

Fig. 2.1 shows a two-dimensional single fiber partially embedded considered in this study. The shaded (slashed) part represents a rectangular-shaped fiber whose Young's modulus is denoted by E_F and whose Poisson's Ratio is denoted by ν_F . The grey portion represents the matrix having a semi-infinite region whose Young's modulus is denoted by E_M and whose Poisson's Ratio is denoted by ν_M . Subscripts M, F represent the matrix and reinforcing fiber, respectively. Assume that perfectly bonded fiber/matrix interface whose material properties vary in a stepwise manner across the interface. A uniform tensile stress is distributed at the free end of the fiber, and the total force is P . The embedding length l_b represents the distance from

the surface of the matrix to the buried end of fiber. Notation D represents the diameter of the fiber, i.e. the width of the fiber in this 2D analysis. Point E^* is used to represent the interface on the surface of the matrix. Similarly, Point A^* represents the interface corner at the fiber end. Notations E_F , ν_F , E_M , ν_M represent the Young's modulus and Poisson's ratio of fiber and matrix, respectively. Singular interface stress fields^{31)–33)}, which will be explained in the next section, are indicated in Fig. 2.1 around Point A^* and Point E^* . They are controlled by the intensity of the singular stress fields (ISSFs, denoted by K_{σ}^A , λ_1^A etc.)^{31)–33)}.

Many researchers have been working on fiber pull-out experiments. For example, Scheer et al.³⁴⁾ experimentally investigated interfacial peeling of reinforcing fibers, focusing on the energy release rate. Zhandarov et al.^{35),36)} investigated the pull-out force versus displacement. The $P(\delta)$ curve of pull-out test and $P(\delta)$ curve of micro-bond tests is similar, i.e. crack propagation may start from the fiber entry Point E^* ^{34)–36)}. Marotzke C. et al.³⁷⁾ investigated the influence of thermally induced stresses and interfacial friction on the interfacial debonding process, focusing on the energy release rate. Wang C. et al.³⁸⁾ and K.-H. Tsai et al.³⁹⁾ investigated the process of fiber pull-out test, focusing on peeling and friction slip, it is observed that crack initiate at the fiber bonded end Point A^* during the fiber pull-out test^{38),39)}. In a rod pull out test that very similar to fiber pull-out test, Atkinson, et al.²⁰⁾ observed crack initiation sometimes occur at Point A^* and sometimes occur at Point E^* in Fig. 2.1.

In the previous pull-out experiments, the interface strength was discussed between the fiber and the matrix without paying attention to the intensity of singular stress field (ISSF). As shown in Fig. 2.1, however, due to the singular stress fields crack initiation sometimes occurs at Point A^* , sometimes occur at Point E^* . Then, the crack may propagate causing final failure. Therefore, to evaluate the mechanical strength of the composites, it is necessary to know the ISSFs at these two points. In the previous studies, the shear-lag theory was widely used to discuss the shear stress distribution of the fiber interface. However, this theory is simply based on one-dimensional fiber model assuming the fiber interface transmits only the shear stress^{40)–42)}; and therefore, this theory cannot express the singular stress fields. In other words, a lot of analytical studies have been done to clarify pull-out phenomena^{21),24),43)}, but no studies are available for

the ISSF.

The authors' recent studies have shown that the ISSFs are useful for evaluating the interface strength because they control the adhesive strength for butt and lap joints ⁵⁾⁻¹¹⁾. Therefore, this paper will focus on the ISSFs of a single fiber partially embedded in a matrix under pull out force. Then, the effect of fiber embedded length on the ISSFs will be investigated and the severities at the fiber end Point A* and at the fiber entry Point E* will be compared by considering their fiber interface stress distributions. The final goal of this study is to clarify the fiber pull out mechanism toward designing suitable fiber reinforced composites.

2.2 Singular stress fields and the ISSF at the fiber end

In this study the finite element method (FEM) is applied to calculating the ISSFs. Since the FEM stress values are usually affected by the mesh size, in the previous study ^{44),45)} the same mesh pattern is applied around the singular points for unknown and reference problems. Then, it was found that the FEM stress ratio of the unknown and reference problem is constant independent of the mesh size. Therefore, the FEM stress ratio is equal to the ISSF ratio because the FEM mesh error can be eliminated by considering FEM stress ratio and applying the same mesh (Detail is discussed in Table 2.2a and b). By choosing the reference problem as an exact solution available, the ISSF of the unknown problem can be obtained by multiplying the FEM stress ratio and the ISSF of the exact solution. Regarding fiber end Point A*, a single fiber in an infinite plate can be chosen as the reference problem. The analysis method used in this study can be called the proportional method since the method is based on the proportional FEM stress fields ^{12),25),46)-49)}. This mesh-independent technique is a convenient ISSF calculation method, and the obtained ISSFs are denoted by $K_{\sigma, \lambda_1^A}^A$ etc. ³¹⁾⁻³³⁾.

Fig. 2.1 shows the two-dimensional model of fiber pull-out problem considered in this paper. Here, a 2D rectangular shape is used to represent the fiber focusing on the singular stress fields at Point A* and Point E*. Although cylindrical shape may be more suitable for representing the fiber, the non-singular term caused by the circumferential strain must be removed and the

analysis becomes complicated ^{8),9)}. Therefore, this modelling should be considered after considering the rectangular modelling.

Table 2.1 shows mechanical properties of the Fiber/Matrix considered in this study. The base material Epon 828 can be obtained by curing a bisphenol A type liquid epoxy resin with m-phenylenediamine. In the previous study, for example, a pull-out test was conducted for a single glass-fiber whose diameter $D = 21\mu\text{m}$ from the matrix Epon 828 ⁴⁴⁾. Since the aspect ratio l_b/D mainly controls the pull-out behavior, $D = 20\mu\text{m}$ is assumed as shown in Table 2.1 and Fig. 2.2. Here, l denotes the total fiber length and l_b the denotes the embedded length; then, $l_b/D = 5$ means $l_b = 100\mu\text{m}$. To obtain the ISSF at the fiber end, model as shown in Fig. 2.2(b) is used as a reference problem. This is because the exact solution is available for the problem as shown in Fig. 2.2(b) ^{31),50)-52)}, which is a rectangular fiber fully embedded in an infinite plate and the total length of the fiber is $2l_b$. Symbol σ_∞ in Fig. 2.2 denotes the uniform tensile stress on the boundary of the infinite plate.

Table 2.1. Mechanical properties of Glass fiber/Epoxy

	Fiber	Matrix (Droplet)
Material	Glass fiber	Epoxy
Young's Modulus (GPa)	75	3.3
Poisson's Ratio	0.17	0.35
Dundurs' Parameter	$\alpha = 0.9071$	
	$\beta = 0.2016$	
Singular Index at Point A*	$\lambda_1^{E*} = 0.7632$	
	$\lambda_2^{E*} = 0.6218$	
Singular Index at Point E*	$\lambda_1^{E*} = 0.6592$	
	$\lambda_2^{E*} = 0.9992$	

In this study, the ISSFs at Point A* and Point E*, for the problem as shown in Fig. 2.1, are mainly discussed by varying l_b . Then, the x-y coordinate system as shown in Fig. 2.1 is used. The y-direction corresponds to the axial direction of the fiber, and the x-direction corresponds to the radial direction of the fiber. Notation r_1 denotes the distance from Point A* in the x-direction, and r_2 denotes the distance from Point A* in the y-direction. Then, $r_1 = 0$ and $r_2 = 0$ means Point A*. Notation r_3 denotes the distance from Point E* in the y-direction, and $r_3 = 0$ represents Point E*.

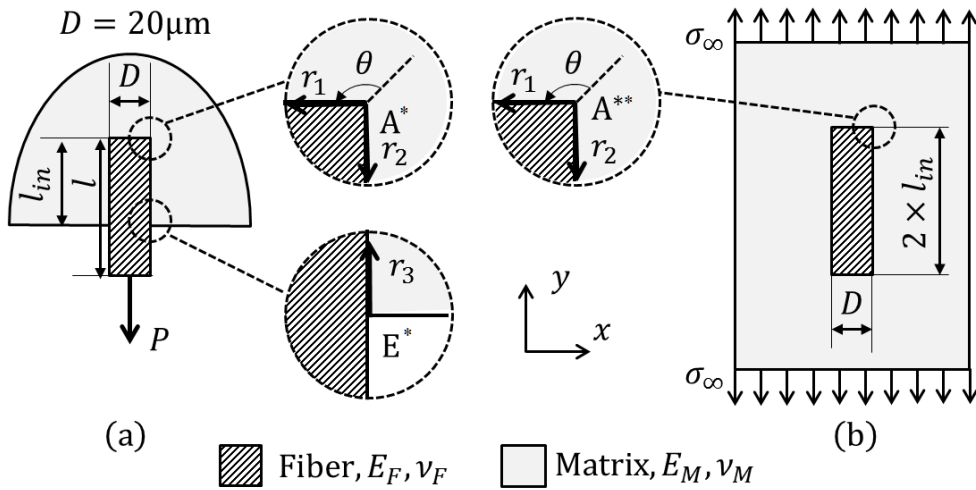


Fig. 2.2. 2D modelling: (a) a single rectangular fiber pull-out from a semi-infinite plate; (b) a single rectangular fiber in an infinite plate under remote tension used as the reference solution.

Note that the singular stress field at Point A^* in Fig. 2.2(a) is similar to the singular stress field at Point A^* of the reinforcing fiber in the matrix shown in Fig. 2.2(b). The ISSF of Point A^* in Fig. 2.2(b) can be calculated by the body force method (BFM)^{31),50)–52)}. The BFM is a powerful analytical method to obtain accurate solutions, which can be virtually regarded as exact solutions.

Till recently, a lot of studies have considered Dundurs' composite parameters of typical engineering materials. Suga et al. investigated the parameters and mechanical compatibility of various material joints⁵³⁾. Yuuki⁵⁴⁾ showed the variations of the parameters in the $\alpha - \beta$ space for the materials combinations among metal, ceramics, resin, and glass. Here, α , β denote Dundurs bimaterial parameters¹⁵⁾ defined by equation (1.3) in Chapter 1. In this study, analysis is carried out under plane strain assumption. Singular indexes λ_1^A and λ_2^A at the corner A can be calculated by solving equations (4.2a) and (4.2b), respectively^{50),55)}. For the material combination Glass Fiber/Epoxy in Table 2.1, $\alpha = 0.9071$, $\beta = 0.2016$), $\lambda_1^A = 0.7632$ and $\lambda_2^A = 0.6218$.

The ISSF at Point A^* in Fig. 2.2(b) was discussed in^{31),51),55)}. It should be noted that equations (2.1) and (2.2)^{44),55)} express the singular stress at Point A^* in Fig. 2.2(b) and also

Point A* in Fig. 2.2(a). Here, $K_{\sigma, \lambda_1^A}^A$, $K_{\sigma, \lambda_2^A}^A$ denote ISSFs for normal stress at Point A* and $K_{\tau, \lambda_1^A}^A$ and $K_{\tau, \lambda_2^A}^A$ denote ISSFs for shear stress. ISSFs $K_{\sigma, \lambda_1^A}^A$ and $K_{\tau, \lambda_1^A}^A$ correspond to Mode I deformation and ISSFs $K_{\sigma, \lambda_2^A}^A$ and $K_{\tau, \lambda_2^A}^A$ correspond to Mode II deformation.

$$\begin{cases} \sigma_y^A(r_1) = \frac{K_{\sigma, \lambda_1^A}^A}{r_1^{1-\lambda_1^A}} + \frac{K_{\sigma, \lambda_2^A}^A}{r_1^{1-\lambda_2^A}} \\ \tau_{yx}^A(r_1) = \frac{K_{\tau, \lambda_1^A}^A}{r_1^{1-\lambda_1^A}} + \frac{K_{\tau, \lambda_2^A}^A}{r_1^{1-\lambda_2^A}} \end{cases} \quad (2.1)$$

$$\begin{cases} \sigma_x^A(r_2) = \frac{K_{\sigma, \lambda_1^A}^A}{r_2^{1-\lambda_1^A}} - \frac{K_{\sigma, \lambda_2^A}^A}{r_2^{1-\lambda_2^A}} \\ \tau_{xy}^A(r_2) = \frac{K_{\tau, \lambda_1^A}^A}{r_2^{1-\lambda_1^A}} - \frac{K_{\tau, \lambda_2^A}^A}{r_2^{1-\lambda_2^A}} \end{cases} \quad (2.2)$$

For the singular stress field at Point A*, the interface corner of different materials, the indexes of the singular stress field are different depending on the mode I and mode II deformation³¹⁾. In order to determine the ISSFs, it is necessary to consider the two distinct mode I and mode II singular stress fields at the same time. The shear stress along the interface of fiber and matrix has been widely discussed by using the shear-lag theory^{34),36),40)-42)}, which is simply based on a one-dimensional model and cannot express singular stress fields.

At the vicinity of Point A*, the stress distribution corresponding to Mode I deformation is denoted by $\sigma_I^A(r)$, as shown in equation (2.3). It is proportional to $1/r^{1-\lambda_1^A}$. And the stress distribution corresponding to Mode II deformation, denoted by $\sigma_{II}^A(r)$, is proportional to $1/r^{1-\lambda_2^A}$. These singular stress fields together determine the stress distributions along the interfaces near Point A*. Each ISSF can be defined as parameters $K_{I, \lambda_1^A}^A$ and $K_{II, \lambda_2^A}^A$ as shown in equation (2.4). In this equation, we can put $r = r_1 = r_2$.

$$\begin{cases} 2\sigma_I^A(r) = \sigma_y^A(r_1) + \sigma_x^A(r_2) \\ 2\sigma_{II}^A(r) = \sigma_y^A(r_1) - \sigma_x^A(r_2) \end{cases} \quad (r = r_1 = r_2) \quad (2.3)$$

$$\begin{cases} K_{I,\lambda_1^A}^A = \lim_{r \rightarrow 0} [\sigma_I^A(r) \cdot r^{1-\lambda_1^A}] \\ K_{II,\lambda_2^A}^A = \lim_{r \rightarrow 0} [\sigma_{II}^A(r) \cdot r^{1-\lambda_2^A}] \end{cases} \quad (2.4)$$

The ISSFs $K_{\sigma,\lambda_1^A}^A$ and $K_{\tau,\lambda_1^A}^A$ in equation (2.1) can be determined from the ISSF $K_{I,\lambda_1^A}^A$. For Fig. 2.2, the ISSFs $K_{\sigma,\lambda_1^A}^A$ and $K_{\tau,\lambda_1^A}^A$ are proportional to $K_{I,\lambda_1^A}^A$ and the ISSFs $K_{\sigma,\lambda_2^A}^A$ and $K_{\tau,\lambda_2^A}^A$ are proportional to $K_{II,\lambda_2^A}^A$.

The normalized stress intensity factors F_I^* and F_{II}^* can be acquired on the basis of BFM^{15),51)–55)}. And the definition of F_I^* and F_{II}^* of the reference problem were expressed as shown in equation (2.5)⁵¹⁾, in which $\sigma_\infty = 1$ is tension stress at the boundary of the infinite matrix, as shown in Fig. 2.2(b).

$$\begin{cases} F_I^* = K_{I,\lambda_1^A}^* / [\sigma_\infty \sqrt{\pi} (D/2)^{1-\lambda_1^A}] \\ F_{II}^* = K_{II,\lambda_2^A}^* / [\sigma_\infty \sqrt{\pi} (D/2)^{1-\lambda_2^A}] \end{cases} \quad (2.5)$$

Therefore, the normalized stress intensity factors of the fiber pull-out problem, as shown in Fig. 2.2(a), are defined similarly as follows:

$$\begin{cases} F_I = K_{I,\lambda_1^A}^A / [(P/D) \sqrt{\pi} (D/2)^{1-\lambda_1^A}] \\ F_{II} = K_{II,\lambda_2^A}^A / [(P/D) \sqrt{\pi} (D/2)^{1-\lambda_2^A}] \end{cases} \quad (2.6)$$

By using the proportional method^{12),25),46)–49)} mentioned above, F_I and F_{II} for the pull-out problem can be calculated from the ISSFs F_I^* and F_{II}^* of the reference problem. As is shown in equation (2.7). Here, $\sigma_{I,FEM}^A(r)$ and $\sigma_{I,FEM}^{A*}(r)$ represent the stress distributions corresponding to Mode I deformation in FEM analysis as mentioned above. Similarly, $\sigma_{II,FEM}^A(r)$ and $\sigma_{II,FEM}^{A*}(r)$ correspond to Mode II deformation.

$$\frac{F_I}{F_I^*} = \frac{\sigma_{I,FEM}^A(r)}{\sigma_{I,FEM}^{A*}(r)}, \quad \frac{F_{II}}{F_{II}^*} = \frac{\sigma_{II,FEM}^A(r)}{\sigma_{II,FEM}^{A*}(r)}. \quad (2.7)$$

The Finite Element Method (FEM) has been widely used for many engineering applications

¹⁶⁾–¹⁸⁾. Regarding fiber reinforced composite analyses, Stern et al. ¹⁹⁾ developed a path independent integral formula for the computation of the intensity of the stress singularity by using FEM. Atkinson et al. ²⁰⁾, Povirk et al. ²¹⁾, and Freund et al. ²²⁾ conducted fiber pullout simulation studies by using a circular rigid cylinder. Hann et al. ⁵⁶⁾ investigated the effect of contact angle, loading position and loading type in micro-bond test by using FEM. Ash et al. ⁵⁷⁾ investigated the effect of bead geometry and knife angle in micro-bond test via FEM. Zhang et al. ²³⁾ studied the effects of interfacial debonding and sliding on fracture characterization of unidirectional fibre-reinforced composites by using FEM. Brito-Santana et al. ⁵⁸⁾ studied influence of the debonding between fiber and matrix in micro scale via the FEM. FEM is widely used in studies in fiber reinforced composites ^{59)–65)}. Ahmed et al. ^{66)–70)} studied sensing, low loss and birefringent etc. by using FEM. In this analysis software MSC Marc is used to express the pull-out model for Fig. 2.1 and 2.2(a), and the reference model for Fig. 2.2(b). Stress distributions along the interfaces (r_1, r_2) are calculated by applying the same mesh pattern to the pull-out model and reference model. Thus stress ratio $\left[\sigma_{I,FEM}^A(r) / \sigma_{I,FEM}^{A*}(r) \right]$ and $\left[\sigma_{II,FEM}^A(r) / \sigma_{II,FEM}^{A*}(r) \right]$ can be calculated between the pull-out model and the reference model. This method was used in ^{7)–11),44),45)}.

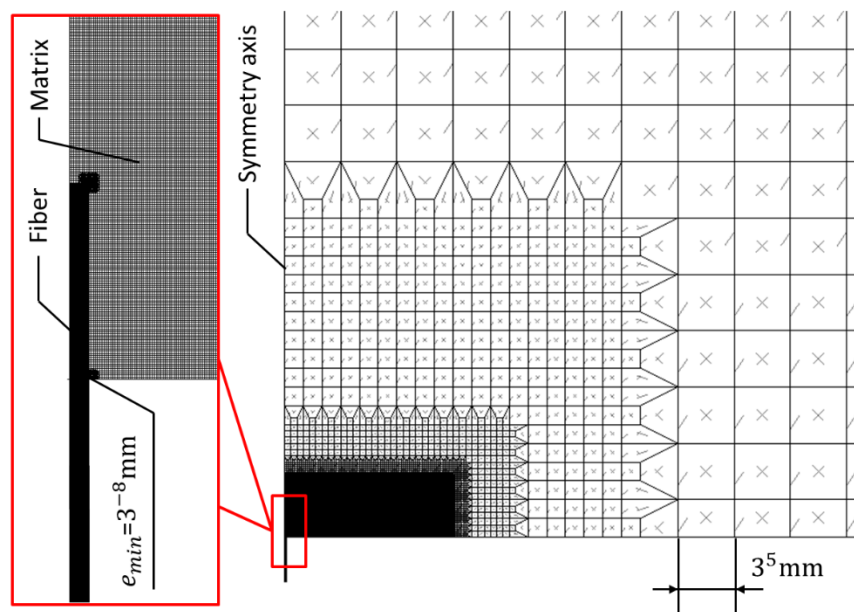


Fig. 2.3. FEM mesh pattern

As is shown in equation (2.3), $\sigma_{I,FEM}^A(r)$ is calculated from the stress distributions $\sigma_y^A(r_1)$ along the interface r_1 and $\sigma_x^A(r_2)$ along the interface r_2 by using the pull-out model (Fig. 2.2(a)). Similarly, $\sigma_{I,FEM}^{A*}(r)$ is calculated from the stress distributions $\sigma_y^{A*}(r_1)$ along the interface r_1 and $\sigma_x^{A*}(r_2)$ along the interface r_2 by using the reference model (Fig. 2.2(b)). Material properties for the fiber and matrix are set to be same for the reference model and pull-out model, respectively. In other words, material properties of fiber in Fig. 2.2(b) and inclusion in Fig. 2.2(b) are set to be the same.

FEM stress distributions along the interfaces near Point A* of different mesh size are shown in Tables 2.2a and b. Results of inclusion model when $l_{in} = 500\mu m$ and pull-out model when $l_{in} = 100\mu m$ are shown as example. As shown in Table 2.2(a) $\sigma_{I,FEM}^A(r)$ is FEM stress distribution, corresponding to λ_1^A , of glass fiber/epoxy as shown in Table 2.1, when $l_{in} = 100\mu m$ in pull-out model. $\sigma_{I,FEM}^{A*}(r)$ is FEM stress distribution, corresponding to λ_1^A , of the same material combination, when $l_{in} = 500\mu m$ in the reference model, whose ISSF can be calculated by BFM. Similarly, $\sigma_{II,FEM}^A(r)$ in the pull-out model and $\sigma_{II,FEM}^{A*}(r)$ in the reference model, corresponding to λ_2^A are shown in Table 2.2(b). In addition, the FEM stress ratios $\sigma_{I,FEM}^A(r)/\sigma_{I,FEM}^{A*}(r)$, $\sigma_{II,FEM}^A(r)/\sigma_{II,FEM}^{A*}(r)$ are calculated from the above mentioned FEM stress distributions.

As shown in Tables 2.2a and b, the stress distributions $\sigma_{I,FEM}^A(r)$, $\sigma_{II,FEM}^A(r)$ are different depending on the mesh size. However, the stress ratio between unknown model and reference model, i.e. $\sigma_{I,FEM}^A(r)/\sigma_{I,FEM}^{A*}(r)$ and $\sigma_{II,FEM}^A(r)/\sigma_{II,FEM}^{A*}(r)$ are independent of mesh size, and keep in converges within four significant digits. In fact, the stress at the edge of the interface is infinite. Therefore, the value of the stress varies greatly depending on the mesh size. From the data shown in Tables 2.2a and b, it is found that the stress ratio between the pull-out problem and the reference problem can be obtained accurately independent of the mesh size. Then the ISSF of pull-out problem can be obtained from the FEM stress ratio and the ISSF of reference

problems, as shown in equation (2.7).

Table 2.2(a). FEM Stress ratio of symmetrical type with $\lambda_1^A = 0.7784$ when $l_{in} = 100\mu\text{m}$ in Fig. 2.2(a) and $l_{in} = 500\mu\text{m}$ in Fig. 2.2(b) for the material combination in Table 2.1.

Smallest mesh size $e_{min} = 3^{-9}$ [mm]			Smallest mesh size $e_{min} = 3^{-10}$ [mm]		
$\frac{r}{e_{min}}$	$\sigma_{I,FEM}^A(r)$ [MPa]	$\sigma_{I,FEM}^A(r)$ $\sigma_{I,FEM}^{A*}(r)$	$\frac{r}{e_{min}}$	$\sigma_{I,FEM}^A(r)$ [MPa]	$\sigma_{I,FEM}^A(r)$ $\sigma_{I,FEM}^{A*}(r)$
0.0	1.290	0.117	0.0	1.647	0.117
0.5	1.038	0.117	0.5	1.328	0.117
1.0	0.779	0.116	1.0	0.998	0.117
1.5	0.699	0.116	1.5	0.896	0.116
2.0	0.692	0.115	2.0	0.889	0.116

Table 2.2(b). FEM stress ratio of skew-symmetrical type with $\lambda_2^A = 0.6158$ when $l_{in} = 100\mu\text{m}$ in Fig. 2.2(a) and $l_{in} = 500\mu\text{m}$ in Fig. 2.2(b) for the material combination in Table 2.1.

Smallest mesh size $e_{min} = 3^{-9}$ [mm]			Smallest mesh size $e_{min} = 3^{-10}$ [mm]		
$\frac{r}{e_{min}}$	$\sigma_{II,FEM}^A(r_1)$ [MPa]	$\sigma_{II,FEM}^A(r_1)$ $\sigma_{II,FEM}^{A*}(r_1)$	$\frac{r}{e_{min}}$	$\sigma_{II,FEM}^A(r_1)$ [MPa]	$\sigma_{II,FEM}^A(r_1)$ $\sigma_{II,FEM}^{A*}(r_1)$
0.0	10.161	0.104	0.00	15.497	0.104
0.5	4.279	0.104	0.5	6.524	0.104
1.0	1.821	0.104	1.0	2.773	0.104
1.5	2.913	0.104	1.5	4.438	0.104
2.0	3.048	0.104	2.0	4.642	0.104

2.3 Singular stress field and the ISSF at the fiber entry point

The singular stress field at Point E* as shown in Fig. 2.2(a) is different from that of Point A* but similar to the interface end for lap joints^{48),71)}. The value of singular indexes (λ_1^E, λ_2^E)

around the corner E can be determined by solving the characteristic equation (2.8)^{13),14)}. For most of the material combinations the singular indexes λ_i^E have two real roots λ_1^E and λ_2^E corresponding to two different singular fields²⁹⁾.

$$4\sin^2(\pi\lambda) \left\{ \sin^2\left(\frac{\pi\lambda}{2}\right) - \lambda^2 \right\} \beta^2 + 4\lambda^2 \sin^2(\pi\lambda) \alpha\beta + \left\{ \sin^2\left(\frac{\pi\lambda}{2}\right) - \lambda^2 \right\} \alpha^2 + 4\lambda^2 \sin^2(\pi\lambda) \beta + 2 \left\{ \lambda^2 \cos(2\pi\lambda) + \sin^2\left(\frac{\pi\lambda}{2}\right) \cos(\pi\lambda) + \frac{1}{2} \sin^2(\pi\lambda) \right\} \alpha + \sin^2\left(\frac{3\pi\lambda}{2}\right) - \lambda^2 = 0 \quad (2.8)$$

Here, α and β are defined by equation (1.3). Table 2.1 shows for the Glass/Epoxy material combination, $\alpha = 0.9071$, $\beta = 0.2016$, $\lambda_1^E = 0.6592$, $\lambda_2^E = 0.9992$. Note that the singular index $\lambda_2^E = 0.9992$ for $K_{\sigma,\lambda_2^E}^E$ is very close to 1, corresponding to almost no singularity having little effect on the singular stress distribution.

The singular stress field at the vicinity of Point E* in Fig. 2.1 can be expressed as equation (2.9). This singular stress field is identical to that of lap joints^{48),71)}.

$$\begin{cases} \sigma_x^E(r_3) = \frac{K_{\sigma,\lambda_1^E}^E}{r_3^{1-\lambda_1^E}} + \frac{K_{\sigma,\lambda_2^E}^E}{r_3^{1-\lambda_2^E}} \\ \tau_{xy}^E(r_3) = \frac{K_{\tau,\lambda_1^E}^E}{r_3^{1-\lambda_1^E}} + \frac{K_{\tau,\lambda_2^E}^E}{r_3^{1-\lambda_2^E}} \end{cases} \quad (2.9)$$

As the reference solution Reciprocal work contour integral method (RWCIM) can be used^{12),26),48),71)}. Recently, Miyazaki et al.^{12),49)} proposed a technique of how to obtain two ISSFs corresponding to two distinct singular stress fields by applying proportional method. To apply this method to the pull-out problem, Fig. 2.4 illustrates 3 kinds of the pull-out models used in this technique.

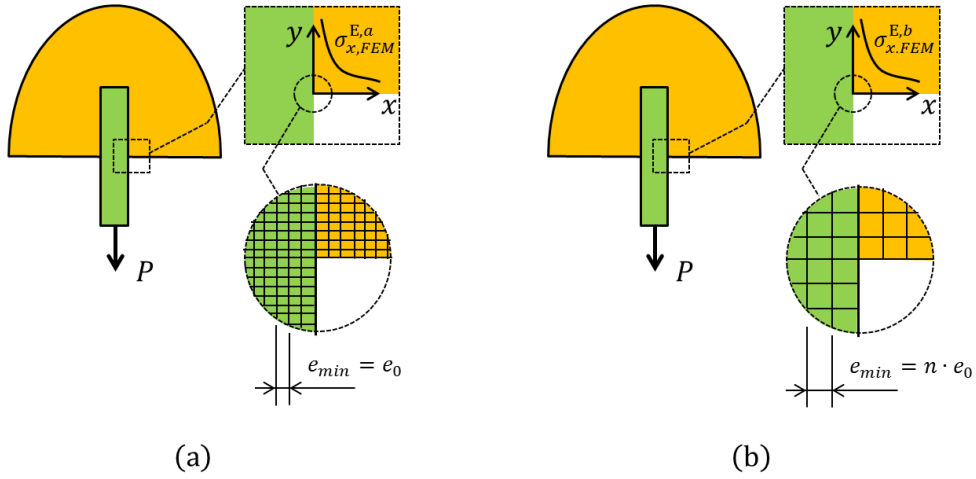


Fig. 2.4(a) and Fig. 2.4(b). Schematic illustration of Point E* FEM models

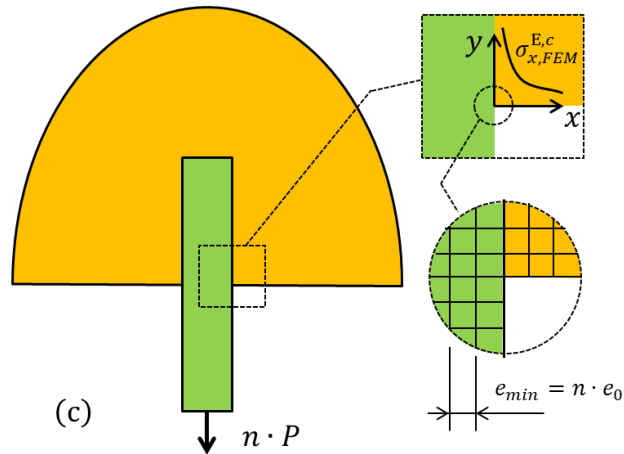


Fig. 2.4(c). Schematic illustration of Point E* FEM models

The model (a) has minimum elements whose size $e_{min} = e_0$. The FEM stress of the model (a) is denoted by $\sigma_{x,FEM}^{E,a}(r_3)|_{e_{min}=e_0}$ and the ISSFs in model (a) are denoted by $K_{\sigma,\lambda_1^E}^{E,a}$ and $K_{\sigma,\lambda_2^E}^{E,a}$. Here, r_3 is the distance from the corner edge Point E* in Fig. 2.2(a). The model (b) has the same size of the model (a) but having larger minimum elements $e_{min} = n \cdot e_0$ compared to model (a). The FEM stress of model (b) is denoted by $\sigma_{x,FEM}^{E,b}(r_3)|_{e_{min}=n \cdot e_0}$ and the ISSFs in model (b) are denoted by $K_{\sigma,\lambda_1^E}^{E,b}$ and $K_{\sigma,\lambda_2^E}^{E,b}$. The model (c) is n times larger than models (a) including all elements and therefore having the same minimum mesh size of model

(b). The FEM stress of model (c) is denoted by $\sigma_{x,FEM}^{E,c}(r_3)|_{e_{min}=n \cdot e_0}$. It can be verified that the stress $\sigma_{x,FEM}^{E,c}$ at $n \cdot r_0$ is equal to the stress $\sigma_{x,FEM}^{E,a}$ at r_0 . The ISSFs in model (c) are denoted by $K_{\sigma,\lambda_1}^{E,c}$ and $K_{\sigma,\lambda_2}^{E,c}$. The FEM stress $\sigma_{x,FEM}^{E,a}$ should be divided into $\sigma_{x,FEM,\lambda_1}^{E,a}$ and $\sigma_{x,FEM,\lambda_2}^{E,a}$ to calculate two ISSFs K_{σ,λ_1}^E and K_{σ,λ_2}^E .

$$\sigma_{x,FEM}^{E,a} = \sigma_{FEM,\lambda_1}^{E,a} + \sigma_{FEM,\lambda_2}^{E,a} \quad (2.10)$$

Similarly, $\sigma_{x,FEM}^{E,b}$ and $\sigma_{x,FEM}^{E,c}$ should be divided.

$$\sigma_{x,FEM}^{E,b} = \sigma_{FEM,\lambda_1}^{E,b} + \sigma_{FEM,\lambda_2}^{E,b} \quad (2.11a)$$

$$\sigma_{x,FEM}^{E,c} = \sigma_{FEM,\lambda_1}^{E,c} + \sigma_{FEM,\lambda_2}^{E,c} \quad (2.11b)$$

The stress distribution $\sigma_{x,FEM}^{E,c}(r_3)$ at $r_3 = n \cdot r_0$ is exactly equal to the stress $\sigma_{x,FEM}^{E,a}(r_3)$ at $r_3 = r_0$ as shown in equation (2.12).

$$\frac{K_{\sigma,\lambda_1}^{E,a}}{(r_0)^{1-\lambda_1^E}} + \frac{K_{\sigma,\lambda_2}^{E,a}}{(r_0)^{1-\lambda_2^E}} = \frac{K_{\sigma,\lambda_1}^{E,c}}{(n \cdot r_0)^{1-\lambda_1^E}} + \frac{K_{\sigma,\lambda_2}^{E,c}}{(n \cdot r_0)^{1-\lambda_2^E}} \quad (2.12)$$

From equation (2.12) the following relation between $K_{\sigma,\lambda_1}^{E,a}$ and $K_{\sigma,\lambda_1}^{E,c}$ can be derived.

$$\begin{cases} \frac{K_{\sigma,\lambda_1}^{E,c}}{K_{\sigma,\lambda_1}^{E,a}} = n^{1-\lambda_1^E} \\ \frac{K_{\sigma,\lambda_2}^{E,c}}{K_{\sigma,\lambda_2}^{E,a}} = n^{1-\lambda_2^E} \end{cases} \quad (2.13)$$

Since the mesh pattern is the same at the vicinity of Point E^* in model (b) and model (c), the following relation can be verified.

$$\begin{cases} \frac{K_{\sigma,\lambda_1}^{E,c}}{K_{\sigma,\lambda_1}^{E,b}} = \frac{\sigma_{FEM,\lambda_1}^{E,c}(n \cdot r_0)}{\sigma_{FEM,\lambda_1}^{E,b}(n \cdot r_0)} \\ \frac{K_{\sigma,\lambda_2}^{E,c}}{K_{\sigma,\lambda_2}^{E,b}} = \frac{\sigma_{FEM,\lambda_2}^{E,c}(n \cdot r_0)}{\sigma_{FEM,\lambda_2}^{E,b}(n \cdot r_0)} \end{cases} \quad (2.14)$$

Substituting equation (2.13) into equation (2.14) and using the $\sigma_{x,FEM}^{E,a}(r_3)|_{r_3=r_0} = \sigma_{x,FEM}^{E,c}(r_3)|_{r_3=n \cdot r_0}$, the following equation is obtained.

$$\begin{cases} \sigma_{FEM,\lambda_1}^{E,b}(n \cdot r_0) = \frac{\sigma_{FEM,\lambda_1}^{E,a}(r_0)}{n^{1-\lambda_1^E}} \\ \sigma_{FEM,\lambda_2}^{E,b}(n \cdot r_0) = \frac{\sigma_{FEM,\lambda_2}^{E,a}(r_0)}{n^{1-\lambda_2^E}} \end{cases} \quad (2.15)$$

Substituting equation (2.15) into equation (2.11a) the following equation is obtained ^{12),49)}.

$$\begin{aligned} \sigma_{x,FEM}^{E,b} &= \sigma_{FEM,\lambda_1}^{E,b} + \sigma_{FEM,\lambda_2}^{E,b} \\ &= \frac{\sigma_{FEM,\lambda_1}^{E,a}}{n^{1-\lambda_1^E}} + \frac{\sigma_{FEM,\lambda_2}^{E,a}}{n^{1-\lambda_1^E}} \end{aligned} \quad (2.16)$$

When the simultaneous equations (2.10) and (2.16) are solved on the $\sigma_{x,FEM,\lambda_1}^{E,a}$ and $\sigma_{x,FEM,\lambda_2}^{E,a}$, the following equations are obtained. By using this method, the stress distributions corresponding to the two indexes λ_1^E , λ_2^E can be obtained in FEM.

$$\begin{cases} \sigma_{FEM,\lambda_1}^{E,a} = \frac{\sigma_{x,FEM}^{E,a}}{1-n^{\lambda_1-\lambda_2}} - \frac{\sigma_{x,FEM}^{E,b}}{n^{\lambda_2-1-n^{\lambda_1-1}}} \\ \sigma_{FEM,\lambda_2}^{E,a} = \frac{\sigma_{x,FEM}^{E,a}}{1-n^{\lambda_2-\lambda_1}} + \frac{\sigma_{x,FEM}^{E,b}}{n^{\lambda_2-1-n^{\lambda_1-1}}} \end{cases} \quad (2.17)$$

As shown in equation (2.18), if the ISSFs $K_{\sigma,\lambda_1}^{E*}$ and $K_{\sigma,\lambda_2}^{E*}$ are known in a reference problem, the ISSFs of a unknown problem can be obtained from FEM stress ratio $\sigma_{FEM,\lambda_1}^E(r)/\sigma_{FEM,\lambda_1}^{E*}(r)$ and $\sigma_{FEM,\lambda_2}^E(r)/\sigma_{FEM,\lambda_2}^{E*}(r)$. Here, $\sigma_{FEM,\lambda_1}^E(r)$ and $\sigma_{FEM,\lambda_2}^E(r)$ are FEM stress distributions in the model corresponding to unknown problem, and are divided by using equation (2.17). Similarly, $\sigma_{FEM,\lambda_1}^{E*}(r)$ and $\sigma_{FEM,\lambda_2}^{E*}(r)$ corresponding to the reference problem.

$$\begin{cases} \frac{K_{\sigma,\lambda_1}^E}{K_{\sigma,\lambda_1}^{E*}} = \frac{\sigma_{FEM,\lambda_1}^E}{\sigma_{FEM,\lambda_1}^{E*}} \\ \frac{K_{\sigma,\lambda_2}^E}{K_{\sigma,\lambda_2}^{E*}} = \frac{\sigma_{FEM,\lambda_2}^E}{\sigma_{FEM,\lambda_2}^{E*}} \end{cases} \quad (2.18)$$

Tables 2.3a and b shows FEM stress ratio $\sigma_{FEM,\lambda_1}^E(r)/\sigma_{FEM,\lambda_1}^{E*}(r)$ and $\sigma_{FEM,\lambda_2}^E(r)/\sigma_{FEM,\lambda_2}^{E*}(r)$ for Glass Fiber/Epoxy in Table 2.1 obtained by using the technique described above.

Chapter 2

Here, $\sigma_{FEM,\lambda_1}^E(r)$ is the value for $l_{in} = 100\mu\text{m}$ and $\sigma_{FEM,\lambda_2}^{E^*}(r)$ is the value for $l_{in} = 200\mu\text{m}$. In Table 2.3(a), the stress ratio is independent of the mesh size and coincides with the results of RWCIM. In Table 2.3(b), however, the stress ratio varies by about 10% error. This is because the singular index $\lambda_2^E = 0.9992 \approx 1$. Since $\lambda_2^E \approx 1$ means almost no singularity with smaller values $K_{\sigma,\lambda_2}^E/r_3^{1-\lambda_2^E}$ and $K_{\tau,\lambda_2}^E/r_3^{1-\lambda_2^E}$ in equation (2.9), the singular stress is mainly controlled only by K_{σ,λ_1}^E and K_{τ,λ_1}^E ^{44),45)}. The RWCIM can be used to obtain the reference values although a large calculation time is necessary for the integral path. The proportional method can be conveniently focusing on the singular point to calculate the ISSFs by varying the fiber dimensions.

Table 2.3(a). FEM stress ratio of the first term with $\lambda_1^E = 0.6592$ when $l_{in} = 100\mu\text{m}$ and $l_{in} = 200\mu\text{m}$ in Fig. 2.1 (a) for the material combination in Table 2.1.

Smallest mesh size $e_{min} = 3^{-9} D$			Smallest mesh size $e_{min} = 3^{-10} D$			RWCIM
$\frac{r}{e_{min}}$	$\sigma_{FEM,\lambda_1}^E(r)$ [MPa]	$\frac{\sigma_{FEM,\lambda_1}^E(r)}{\sigma_{FEM,\lambda_1}^{E^*}(r)}$	$\frac{r}{e_{min}}$	$\sigma_{FEM,\lambda_1}^E(r)$ [MPa]	$\frac{\sigma_{FEM,\lambda_1}^E(r)}{\sigma_{FEM,\lambda_1}^{E^*}(r)}$	$\frac{K_{\sigma,\lambda_1}^E}{K_{\sigma,\lambda_1}^{E^*}}$
0.0	13.022	1.34	0.0	9.114	1.34	1.34
0.5	11.102	1.34	0.5	7.770	1.34	
1.0	8.131	1.34	1.0	5.691	1.34	
1.5	6.775	1.34	1.5	4.742	1.34	
2.0	6.389	1.34	2.0	4.472	1.34	

Table 2.3(b). FEM stress ratio of the second term with $\lambda_2^E = 0.9992$ when $l_{in} = 100\mu\text{m}$ and $l_{in} = 200\mu\text{m}$ in Fig. 2.1(a) for the material combination in Table 2.1.

Smallest mesh size $e_{\min} = 3^{-9} D$			Smallest mesh size $e_{\min} = 3^{-10} D$			RWCIM
$\frac{r}{e_{\min}}$	$\sigma_{FEM,\lambda_2}^E(r)$	$\frac{\sigma_{FEM,\lambda_2}^E(r)}{\sigma_{FEM,\lambda_2}^{E*}(r)}$	$\frac{r}{e_{\min}}$	$\sigma_{FEM,\lambda_2}^E(r)$ [MPa]	$\frac{\sigma_{FEM,\lambda_2}^E(r)}{\sigma_{FEM,\lambda_2}^{E*}(r)}$	
0.0	-0.010	0.873	0.00	-0.011	0.932	0.970
0.5	-0.016	0.866	0.5	-0.016	0.908	
1.0	-0.016	0.868	1.0	-0.017	0.923	
1.5	-0.016	0.875	1.5	-0.017	0.923	
2.0	-0.016	0.879	2.0	-0.016	0.926	

2.4. Results and discussion.

In short fiber reinforced composites most fibers' aspect ratios are close to $l/D = 30$ ⁵²⁾. In this study, assume the fiber width $D = 20 \mu\text{m}$ and the total fiber length $l = 600 \mu\text{m}$. If half of the fiber length is embedded in the matrix, as shown in Fig. 2.2(a), the fiber embedded length is about $l_{in} = 300 \mu\text{m}$.

2.4.1 ISSF at Point A*

As shown in Table 2.4 for glass fiber/epoxy, mode I ISSF $K_{\sigma,\lambda_1}^A = 0.0767$ at $l_{in} = 300 \mu\text{m}$ is 36.1% smaller than $K_{\sigma,\lambda_1}^A = 0.120$ at $l_{in} = 150 \mu\text{m}$. Regarding Mode II ISSF, $K_{\sigma,\lambda_2}^A = 0.139$ at $l_{in} = 300 \mu\text{m}$ is 32.8% smaller than $K_{\sigma,\lambda_2}^A = 0.207$ at $l_{in} = 150 \mu\text{m}$. As shown in Fig. 2.5 and Table 2.4, the ISSFs K_{τ,λ_1}^A and K_{τ,λ_2}^A are also about 40% smaller than the ISSFs K_{σ,λ_1}^A and K_{σ,λ_2}^A for glass fiber/epoxy. Therefore, the ISSFs K_{σ,λ_1}^A and K_{σ,λ_2}^A will be mainly discussed.

Chapter 2

Table 2.4. ISSFs at Point A*, K_{σ,λ_1}^A , K_{σ,λ_2}^A , K_{τ,λ_1}^A , K_{τ,λ_2}^A in Fig. 2.1 for the material combination in Table 2.1.

l_{in} [μm]	K_{σ,λ_1}^A [MPa · m ^{1-0.7632}]	K_{σ,λ_2}^A [MPa · m ^{1-0.6218}]	K_{τ,λ_1}^A [MPa · m ^{1-0.7632}]	K_{τ,λ_2}^A [MPa · m ^{1-0.6218}]
50	0.220	0.343	0.128	0.175
100	0.152	0.258	0.0885	0.131
150	0.120	0.207	0.0696	0.106
200	0.101	0.177	0.0585	0.0905
250	0.0873	0.156	0.0507	0.0796
300	0.0767	0.139	0.0445	0.0706
350	0.0689	0.126	0.0400	0.0641
400	0.0627	0.115	0.0364	0.0587
450	0.0571	0.106	0.0332	0.0538
500	0.0528	0.0980	0.0307	0.0500
1000	0.0296	0.0565	0.0172	0.0288

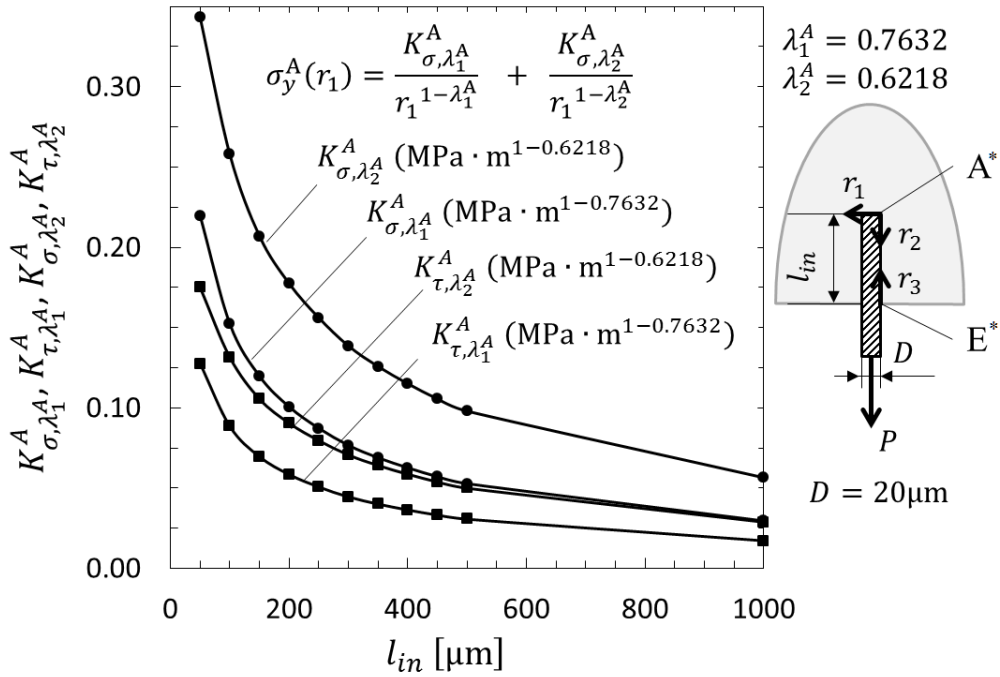


Fig. 2.5. ISSFs at Point A* vs. embedding length for Glass Fiber/Epoxy

2.4.2 ISSF at Point E*

Table 2.5 and Fig. 2.6 show the ISSFs for glass fiber/epoxy. The ISSF at Point E* decreases with increasing l_{in} . Regarding the first term K_{σ, λ_1}^E in Equation (2.9) for glass fiber/epoxy, $K_{\sigma, \lambda_1}^E = 0.339$ at $l_{in} = 300 \mu\text{m}$ is 12.9% smaller than $K_{\sigma, \lambda_1}^E = 0.389$ at $l_{in} = 150 \mu\text{m}$. The ISSF decreasing rate at Point E* becomes smaller than that at Point A* especially when l_{in} is large. Since the ISSF K_{τ, λ_1}^E is 60% smaller than the ISSF K_{σ, λ_1}^E for this material combination, K_{σ, λ_1}^E is discussed in the next section.

Table 2.5. ISSFs at Point E*, K_{σ,λ_1}^E , K_{σ,τ_1}^E in Fig. 2.1

for the material combination in Table 2.1.

l_{in} [μm]	K_{σ,λ_1}^E [$\text{MPa} \cdot \text{m}^{1-0.6591}$]	K_{τ,λ_1}^E [$\text{MPa} \cdot \text{m}^{1-0.6591}$]
50	0.530	0.197
100	0.433	0.161
150	0.389	0.144
200	0.364	0.135
250	0.349	0.130
300	0.339	0.126
350	0.332	0.123
400	0.326	0.121
450	0.322	0.120
500	0.319	0.119
1000	0.312	0.116

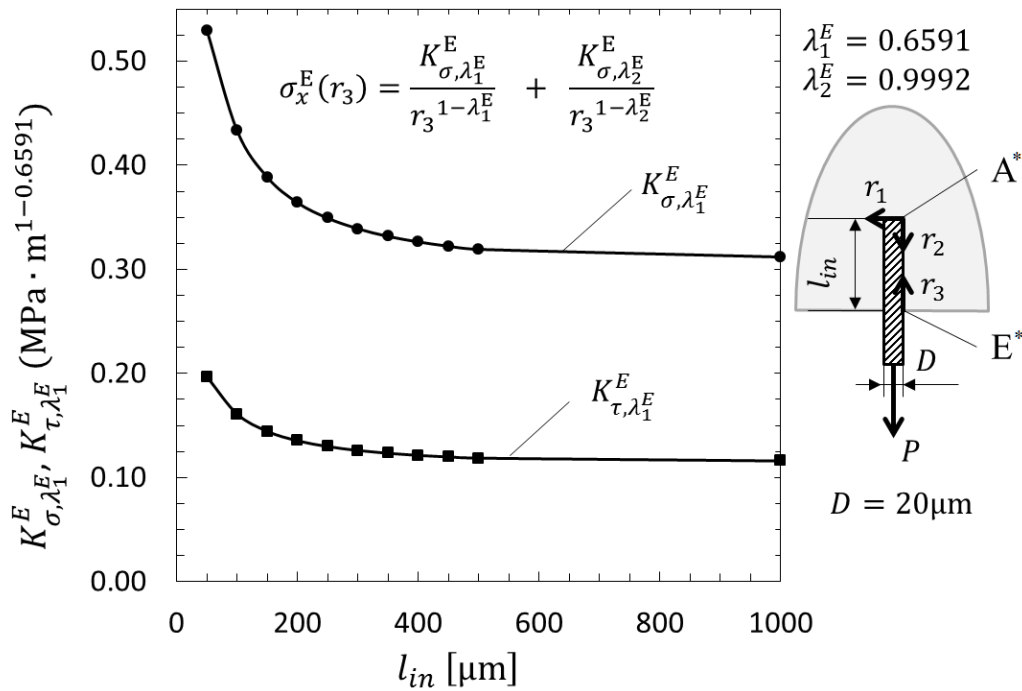


Fig. 2.6. ISSFs at Point E* vs. embedding length for Glass Fiber/Epoxy

2.4.3 Comparison between Point A* and Point E*

When the single embedded fiber is under pull-out force, singular stress fields should be compared at Point A* and Point E*. However, those singular stress fields are different in properties, it is not possible to compare those two ISSFs directly. Therefore, the normal stress distributions along the interfaces between the fiber and matrix are focused. The shear-lag theory^{40)–42)} has been widely used to discuss stress distribution, but is not enough for discuss the singular stress fields. This is because the shear-lag theory is based on a simple one-dimensional approximation of the fiber.

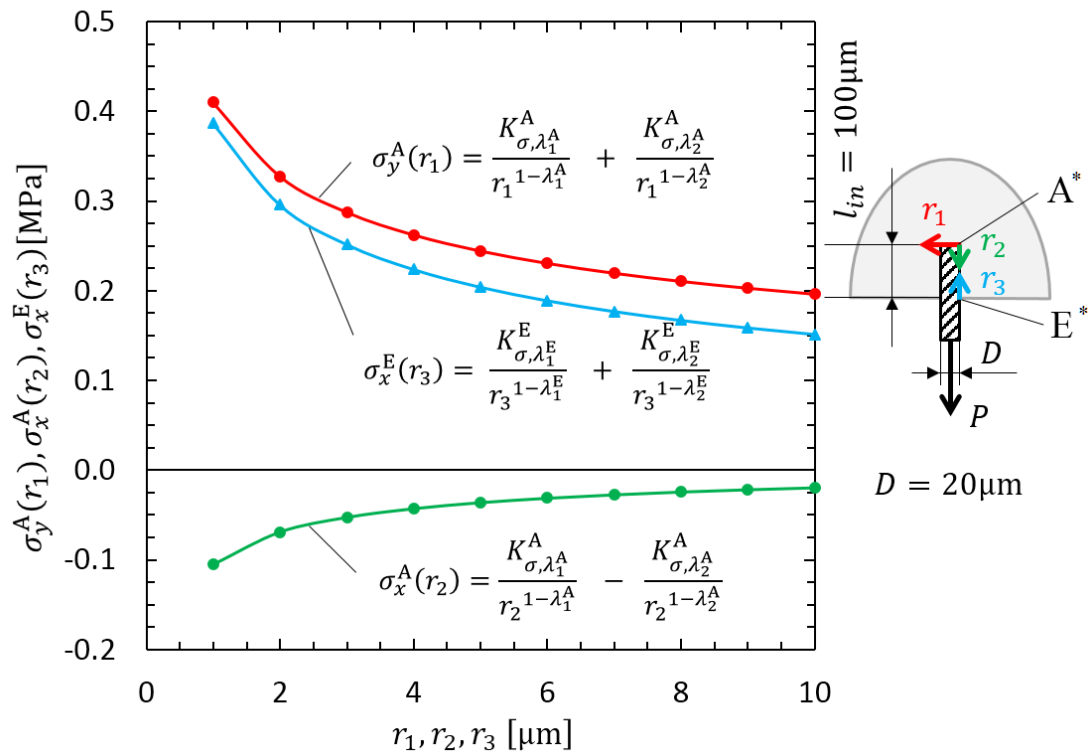


Fig. 2.7. Stress distributions when $l_{in} = 100 \mu\text{m}$ for Glass Fiber/Epoxy in Table 2.1

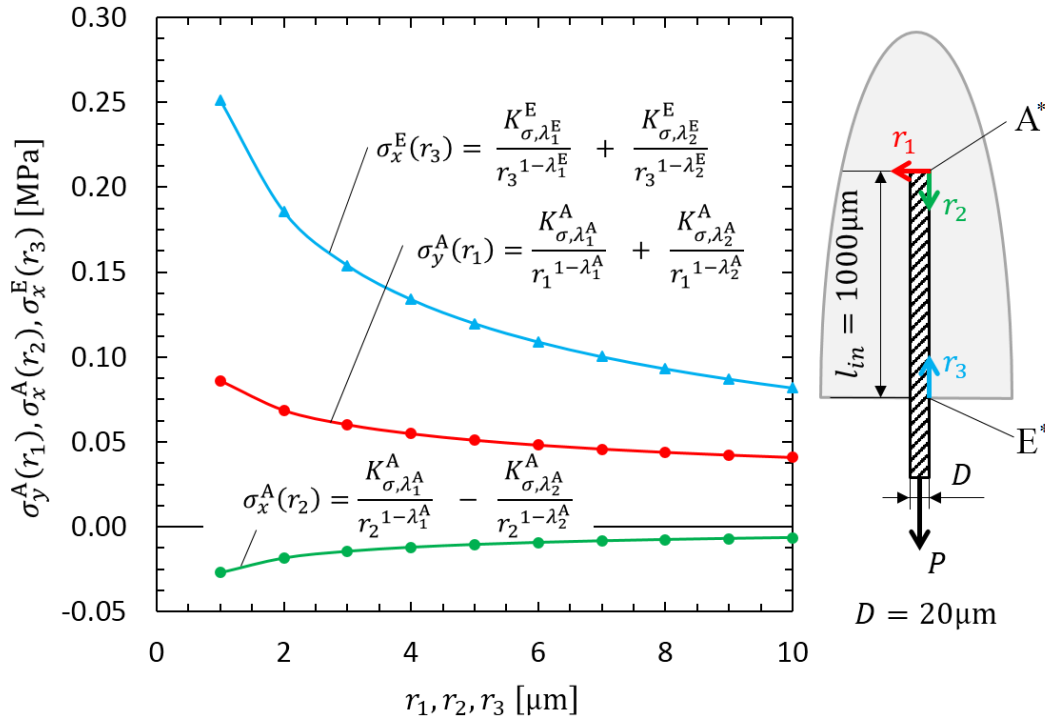


Fig. 2.8. Stress distributions when $l_{in} = 1000 \mu\text{m}$ for Glass Fiber/Epoxy in Table 2.1

The comparison of stress distributions along the interfaces are shown in Fig. 2.7 and Fig. 2.8, that is, $\sigma_y^A(r_1)$ along r_1 \square $\sigma_x^A(r_2)$ along r_2 around Point A^* in Fig. 2.1 and $\sigma_x^E(r_3)$ along r_3 around Point E^* . Equations used in Fig. 2.7 are equations (2.1), (2.2)³¹⁾ and (2.9)^{32),33)}, as shown in Fig. 2.1. Since compressive stress $\sigma_x^A(r_2)$ does not cause the debonding directly, $\sigma_y^A(r_1)$ and $\sigma_x^E(r_3)$ are mainly compared in the following discussion. As shown in Fig. 2.7 for glass fiber/epoxy when $l_{in} = 100 \mu\text{m}$, since the stress $\sigma_y^A(r_1)$ at Point A^* is larger than the stress $\sigma_x^E(r_3)$ at Point E^* , debonding may occur at Point A^* earlier. On the other hand, when $l_{in} = 1000 \mu\text{m}$ in Fig. 2.8, since the stress $\sigma_x^E(r_3)$ at Point E^* is larger than the stress $\sigma_y^A(r_1)$ at Point A^* , debonding may occur earlier at Point E^* .

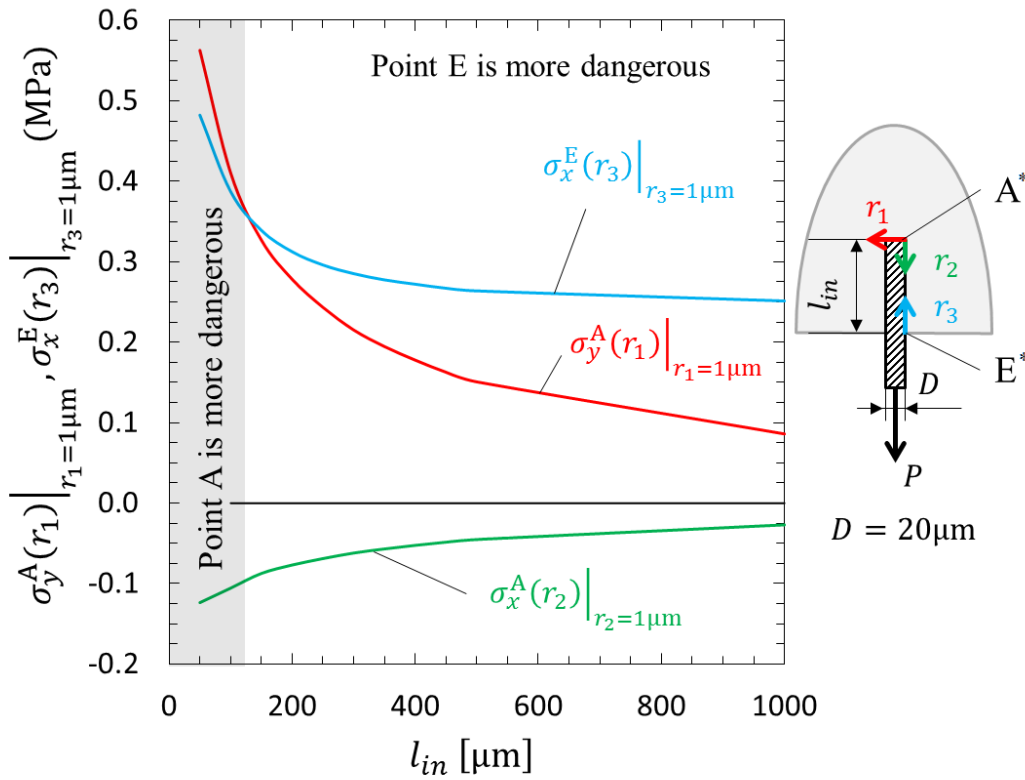


Fig. 2.9. Stress at $r = 1\mu\text{m}$ of different embedding length for Glass Fiber/Epoxy

Fig. 2.9 shows the comparison of stress $\sigma_y^A(r_1)$ at $r_1 = 1\mu\text{m}$ close to Point A* and the stress $\sigma_x^E(r_3)$ at $r_3 = 1\mu\text{m}$ close to Point E* by varying l_{in} . The fixed position $r_1 = r_3 = 1\mu\text{m}$ is selected because the singular stress having different singular indexes. In Fig. 2.9 when $l_{in} = 125\mu\text{m}$, the severity at Point A* and Point E* is almost the same for glass fiber/epoxy based on the assumption $\sigma_y^A(r_1)|_{r_1=1\mu\text{m}} = \sigma_x^E(r_3)|_{r_3=1\mu\text{m}}$. If the stress at different position $r_1 = r_3 \neq 1\mu\text{m}$ is used, for example, if the stresses at $r_1 = r_3 = 2\mu\text{m}$ are compared, the severities are almost the same when $l_{in} = 160\mu\text{m}$ at Point A* and Point E*.

2.5. Conclusions

In this chapter, a partially-embedded single-fiber under pull-out force was considered focusing on two distinct singular stress fields appearing at fiber end and entry points. To compare the severities, singular stress distributions were obtained analytically along the

interfaces along the fiber end and along the fiber entry interface. Then, the following conclusions were obtained.

(1) The mixed-mode ISSFs at the fiber end denoted by $K_{\sigma,\lambda_1}^A \square K_{\sigma,\lambda_2}^A$ decrease with increasing the fiber embedded length l_{in} . Under fixed fiber length $l = 600 \mu\text{m}$, the ISSFs at $l_{in} = (1/2)l$ is about 40% smaller than the ISSFs at $l_{in} = (1/4)l$ for glass fiber/epoxy.

(2) The two ISSFs denoted by $K_{\sigma,\lambda_1}^E \square K_{\sigma,\lambda_2}^E$ at the fiber entry point decrease with increasing the fiber embedded length l_{in} . For example, the ISSFs at $l_{in} = (1/2)l$ is about 10% smaller than the ISSFs at $l_{in} = (1/4)l$ for glass fiber/epoxy. The ISSF decreasing rate at Point E* becomes smaller than that at Point A* especially when l_{in} is large.

(3) The severities were compared at the fiber end and fiber entry point by focusing on the stress just $1\mu\text{m}$ away from the singular point by varying l_{in} (see Fig. 2.9). For glass fiber/epoxy, the severities at the fiber end and fiber entry Point A* are almost the same when $l_{in} = 125\mu\text{m}$. For shorter embedded length, the buried fiber end becomes more dangerous.

Chapter 3 Intensity of Singular Stress Field in Micro-bond Test.

3.1 Introduction

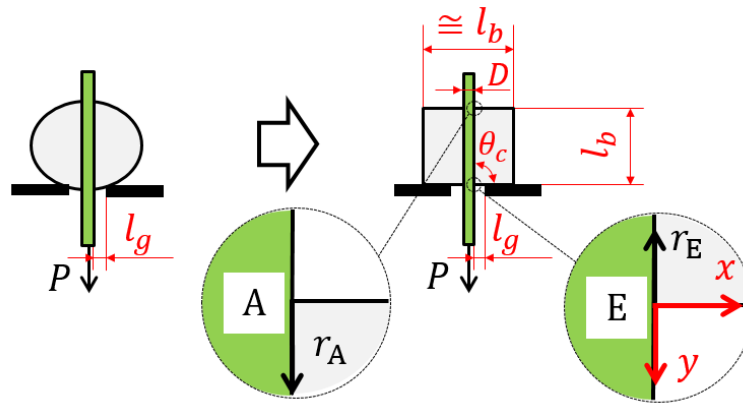


Fig. 3.1. Modelling of micro-bond test of a fiber with $D = 20\mu\text{m}$ and $P/D = 1 \text{ [N} \cdot \text{mm}^{-1}]$

Fig. 3.1 shows a micro-bond test commonly used to investigate fiber/matrix bonding behavior. The green part represents the fiber and the grey portion represents matrix. Point E denotes the fiber entry point closer to the load and constraints; Point A denotes the fiber exit point. Notation l_b denotes the axial length of the bonded area from Point A to Point E before applying load P . Here, the dark portion means constraints. Notation l_g denotes the knife gap opening, that is, the horizontal distance from the constraint knife tip to the fiber surface assuming the symmetry on both sides. Fig. 3.2 shows the single fiber pull-out test treated in the previous paper^{44),72)} whose ISSF will be compared to Fig. 3.1.

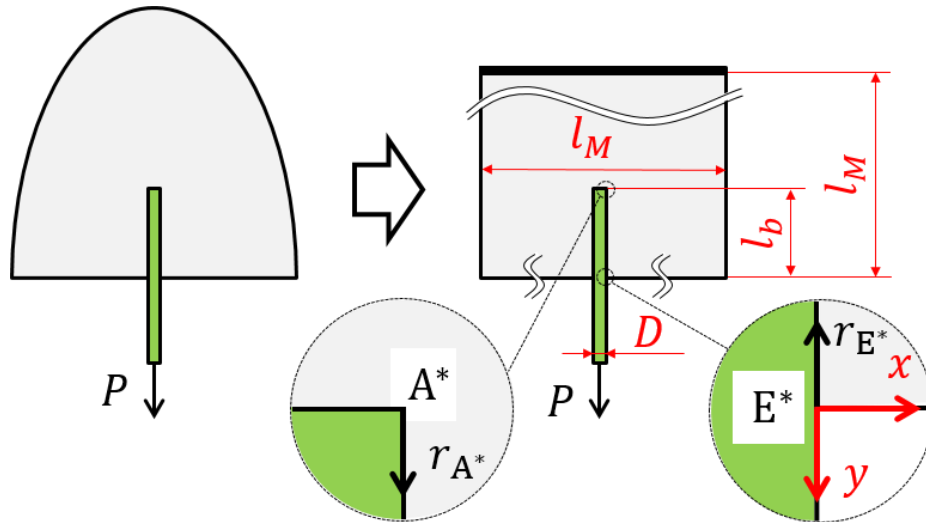


Fig. 3.2. Modelling of pull-out test with $D = 20\mu\text{m}$ and $P/D = 1 \text{ [N} \cdot \text{mm}^{-1}]$ ⁷²⁾

The micro-bond test in Fig. 3.1 can be used more conveniently than the pull-out test in Fig. 3.2 where large matrix region should be prepared by molding during the cure procedure [2,35]. This is the reason why most of the previous experiments employed the micro-bond test instead of the pull-out test ³⁶⁾. In the micro-bond test, the experimental results are strongly affected by the equipment geometries. Under the same fiber/matrix combination, the experimental results of in micro-bond test in Fig. 3.1 is quite different from that in pull-out test in Fig. 3.2. The difference can be characterized by the ISSFs controlling the fiber/matrix interface initial debonding.

In this paper, therefore, the ISSF of the micro-bond test will be analyzed at the fiber entry/exit points. Then, the results will be compared with the ISSF of the pull-out test [33,34] to clarify the difference between the two popular testing methods. The effects of major geometries such as bond length l_b and knife gap opening l_g on the ISSFs in micro-bond test will be also clarified to establish the most suitable testing conditions. In the previous micro-bond tests, very small knife gap opening l_g was used without considering the singular stress. The final goal of this study is to clarify the fiber pull out mechanism toward designing suitable fiber reinforced composites.

3.2. Modelling to analyze intensity of singular stress field (ISSF)

3.2.1 Modelling of micro-bond test in contrast to fiber pull-out test

Fig. 3.1 illustrates the modelling of the micro-bond test to calculate the ISSF. In contrast, Fig. 3.2 illustrates the modelling of the fiber pull-out test whose detail is indicated in the previous paper [33]. As shown in Fig. 3.1 and Fig. 3.2, a similar rectangular shaped fiber is assumed. A smaller rectangular shaped region is assumed for the droplet in Fig. 3.1 in contrast to a larger rectangular shaped region for the matrix in Fig. 3.2. In real micro-bond test, the resin droplet is an irregular sphere shape restrained by the knife-edge. Although the contact angle in micro-bond test is usually $\theta_c = \pi/6 \sim \pi/4$ ³⁵⁾ in Fig. 3.1, in this simulation the contact angle $\theta_c = \pi/2$ is assumed to compare with the ISSFs under the pull-out test in Fig. 3.2. Under this assumption, the singular index is the same at Point E and Point E*. In both models in Fig. 3.1 and Fig. 3.2, perfectly bonded interface is assumed between the resin and the fiber with zero interface thickness. In other words, the material properties around the interface vary in a stepwise manner. Notations E_F , ν_F , E_M , ν_M represent the Young's modulus and Poisson's ratio of fiber and matrix, respectively. Notation D denotes the diameter of the fiber, which is the width of the fiber in the present 2D modelling. A uniform tensile stress is distributed at the end of the fiber, and the total force is P . In other words, $P/D = 1$ [$N \cdot mm^{-1}$] is normalized to analysis the ISSF. The rectangular shaped droplet is assumed as shown in Fig. 3.1 with the large width of the droplet in the x-direction as $l_b/2$ on each side. In other words, in this study, the 2D square shape of the droplet is assumed. Usually, the bonded area $l_b \leq 250\mu m$ is used in the previous micro-bond experiments ^{34),35),56),57),73)–75)}.

In this study, the ISSF in Fig. 3.1 is mainly discussed by varying l_b and l_g under plane strain. In the Cartesian x- and y-coordinates shown in Fig. 3.1 and Fig. 3.2, the y-direction corresponds to the axial direction of the fiber, and the x-direction corresponds to the radial direction of the fiber. Notation r_i , ($i = A, E, E^*$), denotes the distance from Point i , ($i = A, E, E^*$) in the y direction and $r_i = 0$ means Point i . It should be noted that shear-lag theory is widely used for considering shear stress distributions along fiber interface ^{40)–42)}.

However, this theory is simply based on one dimensional assumption of the fiber and cannot express the ISSF. For example, although experiment results of the IFSS is proportional to the bonded length, the real ISSF at the entry point is not proportional to the bonded length ^{44),72)}. In this analysis software MSC Marc is used to analyze the micro-bond model in Fig. 3.1.

3.2.2 Singular stress field at the fiber entry/exit points

The normal singular stress, which may cause debonding at the entry point, can be expressed as follows: ¹²⁾

$$\sigma_x^i = \frac{K_{\sigma, \lambda_1}^i}{r_i^{1-\lambda_1}} + \frac{K_{\sigma, \lambda_2}^i}{r_i^{1-\lambda_2}}, \quad (i = A, E, E^*) \quad (3.1)$$

Here λ_1 and λ_2 are singular indexes, which can be calculated by solving the following characteristic equations ^{13),14)}. Singular indexes at Point E in Fig. 3.1 and Point E* in Fig. 3.2 are same, but singular indexes at Point A in Fig. 3.1 and Point A* in Fig. 3.2 are different. In micro-bond test, Point A and Point E have same singular indexes. Therefore, the ISSFs at Point A, Point E and Point E* can be compared. But they cannot be directly compared with Point A*.

$$\begin{aligned} & 4\sin^2(\pi\lambda)\left\{\sin^2\left(\frac{\pi\lambda}{2}\right)-\lambda^2\right\}\beta^2+4\lambda^2\sin^2(\pi\lambda)\alpha\beta \\ & +\left\{\sin^2\left(\frac{\pi\lambda}{2}\right)-\lambda^2\right\}\alpha^2+4\lambda^2\sin^2(\pi\lambda)\beta \\ & +2\left\{\lambda^2\cos(2\pi\lambda)+\sin^2\left(\frac{\pi\lambda}{2}\right)\cos(\pi\lambda)+\frac{1}{2}\sin^2(\pi\lambda)\right\}\alpha \\ & +\sin^2\left(\frac{3\pi\lambda}{2}\right)-\lambda^2=0 \end{aligned} \quad (3.2)$$

Here, α , β denote bi-material parameters of Dundurs ¹⁵⁾, and G_F and G_M are shear modulus, which can be transformed from Young's modulus E_F , E_M and Poisson's ratios ν_F , ν_M . Subscripts M, F represent the matrix and the reinforcing fiber, respectively. In this study, analysis is carried out under plane strain.

$$\begin{aligned} \alpha &= \frac{G_F(\kappa_M+1)-G_M(\kappa_F+1)}{G_F(\kappa_M+1)+G_M(\kappa_F+1)}, & \beta &= \frac{G_F(\kappa_M-1)-G_M(\kappa_F-1)}{G_F(\kappa_M+1)+G_M(\kappa_F+1)} \\ \kappa_i &= \begin{cases} (3-\nu_i)/(1+\nu_i) & (\text{Plain stress}) \\ (3-4\nu_i) & (\text{Plain strain}) \end{cases} \quad (i = M, F) \end{aligned} \quad (3.3)$$

For the material combination as shown in Table 3.1, $\alpha = 0.9071$, $\beta = 0.2016$, $\lambda_1 =$

0.6592, $\lambda_2 = 0.9992$. Here, λ_2 is close to 1, which means that equation (3.1) can be written as equation (3.4).

$$\sigma_x^i = \frac{K_{\sigma,\lambda_1}^i}{r_i^{1-\lambda_1}} + \frac{K_{\sigma,\lambda_2}^i}{r_i^{1-\lambda_2}} \cong \frac{K_{\sigma,\lambda_1}^i}{r_i^{1-\lambda_1}}, \quad (i = A, E, E^*) \quad (3.4)$$

Table 3.1. Mechanical properties of Glass fiber/Epoxy

	Fiber	Matrix (Droplet)
Material	Glass fiber	Epoxy
Young's Modulus (GPa)	75	3.3
Poisson's Ratio	0.17	0.35
Dundurs' Parameter	$\alpha = 0.9071$	
	$\beta = 0.2016$	
Singular Index	$\lambda_1 = 0.6592$	
	$\lambda_2 = 0.9992$	

Here, K_{σ,λ_1}^i and K_{σ,λ_2}^i denote ISSFs for the normal stress at the vicinity of Point i on the interface r_i ($i = A, E, E^*$). As the λ_2 for most material in reality is close to 1 under this geometry ⁷⁶⁾, the second term K_{σ,λ_2}^i can be omitted, ISSF K_{σ}^i in this study can be expressed by K_{σ,λ_1}^i corresponding with λ_1 . Definition of K_{σ}^i are shown in equation (3.5).

$$K_{\sigma}^i \cong K_{\sigma,\lambda_1}^i = \lim_{r \rightarrow 0} [\sigma_x^i(r_i) \cdot r_i^{1-\lambda_1}], \quad (i = A, E, E^*) \quad (3.5)$$

3.2.3 Proportional method by using FEM

Finite element method (FEM) analysis should be well conducted and may require experience and skills for engineering applications ¹⁶⁾⁻²⁴⁾. In this analysis, a mesh independent proportional method is used to calculate the ISSF K_{σ}^i defined in equation (3.5). Since λ_2 is close to 1, the second term can be omitted, the ISSF can be calculated from the ratio of FEM stress $\sigma_{x,i}^{FEM}(r_i)$ as shown in equation (3.6) ^{12)-14),25)}.

$$\frac{K_{\sigma}^i}{K_{\sigma}^j} \cong \frac{\sigma_{x,FEM}^i(r_i)}{\sigma_{x,FEM}^j(r_j)}, \quad (i, j = A, E, E^*) \quad (3.6)$$

Chapter 3

Table 3.2 shows the FEM stress $\sigma_{x,FEM}^E(r_E)$ near Point E and the FEM stress ratio $\sigma_{x,FEM}^E(r_E)/\sigma_{x,FEM}^A(r_A)$. Although $\sigma_{x,FEM}^E(r_E)$ varies depending on the FEM mesh size, the FEM stress ratio $\sigma_{x,FEM}^E(r_E)/\sigma_{x,FEM}^A(r_A)$ is almost the same independent of mesh size. This is because the same mesh pattern is applied to the singular stress region to cancel the FEM error. The FEM stress ratio in Table 3.2 can be regarded as the real stress ratio although the FEM stress cannot express the real singular stress. Since the stress ratio can be obtained accurately in Table 3.2, the ISSF can be obtained from the ISSF of reference solutions with the ratio as shown in equation (3.6). The ISSF of the pull-out test in Fig. 3.2 can be used as the reference solutions whose FEM modelling is indicated in the Chapter 2^{44),72)}. In Appendix 3.B, an example of the FEM mesh of micro-bond test is indicated in Fig. 3.B.1. It should be noted that the FEM stress $\sigma_{x,FEM}^i(r_i)$ indicated in Table 3.2 is mainly controlled by the minimum element size e_{min} around the singular point.

Table 3.2. FEM Stress ratio with $\lambda_1^i = 0.6592$ when $l_b = 100\mu\text{m}$ and $l_g = 20\mu\text{m}$ between Point E and Point A in Fig. 3.1 for the material combination in Table 3.1.

Smallest mesh size $e_{min} = 3^{-9}D$			Smallest mesh size $e_{min} = 3^{-10}D$		
$\frac{r_i}{e_{min}}$	$\sigma_{x,FEM}^E(r_E)$ [MPa]	$\frac{\sigma_{x,FEM}^E(r_E)}{\sigma_{x,FEM}^A(r_A)}$	$\frac{r_i}{e_{min}}$	$\sigma_{x,FEM}^E(r_E)$ [MPa]	$\frac{\sigma_{x,FEM}^E(r_E)}{\sigma_{x,FEM}^A(r_A)}$
0.0	1.211	-1.376	0.0	1.724	-1.371
0.5	1.033	-1.371	0.5	1.469	-1.368
1.0	0.756	-1.365	1.0	1.075	-1.366
1.5	0.630	-1.359	1.5	0.896	-1.364
2.0	0.594	-1.356	2.0	0.845	-1.363

3.3. Results and Discussion

3.3.1 Bond length l_b effect on ISSF in micro-bond test

Fig. 3.3 and Table 3.3 indicate the ISSF K_σ^E at the entry point and the ISSF K_σ^A of the exit point in comparison with the ISSF K_σ^{E*} of the pull-out test in Fig. 3.2 at the entry point by varying the bond length l_b . Here, other dimensions are fixed as knife gap opening $l_g = 20\mu\text{m}$, fiber diameter $D = 20\mu\text{m}$ and contact angle $\theta_c = \pi/2$ for Glass fiber/Epoxy in Table 3.1. Those ISSFs K_σ^E , K_σ^A , K_σ^{E*} decrease with increasing l_b . As shown in the interface stress distribution in Appendix B, the tensile stress appears near the entry Point E and the compressive stress appears near the exit Point A. From Fig. 3.3 and Table 3.3, no matter how the l_b changes, the entry Point E in micro-bond test is more severe for debonding.

In the pull-out test, a similar tensile ISSF appears the entry point E^* as shown in Fig. 3.3 and also a similar compressive ISSF appears near the end Point A^* in Fig. 3.2. The ISSFs at Point E and Point E^* decrease in a similar way by increasing l_b .

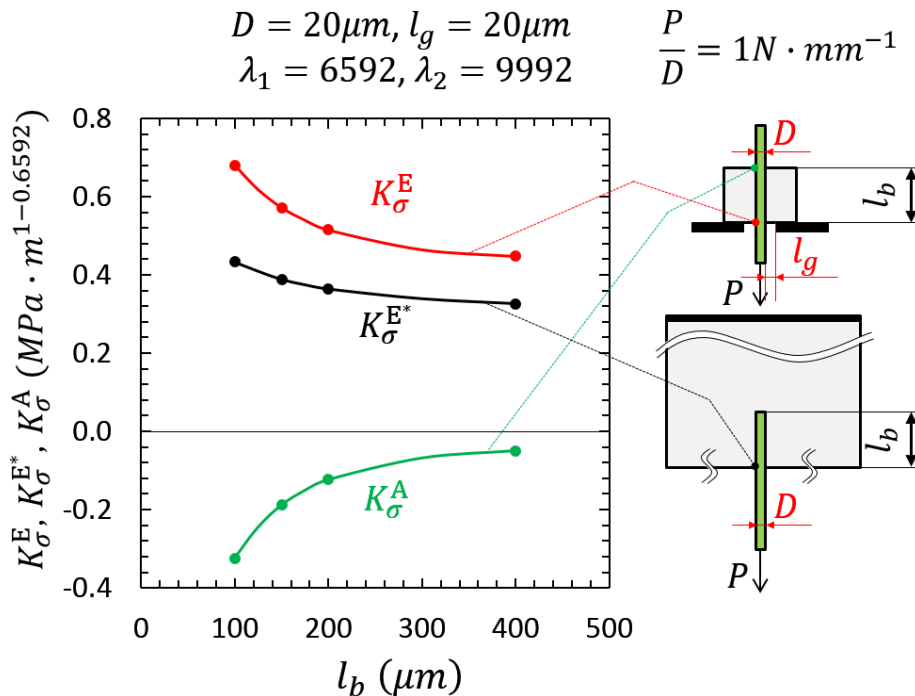


Fig. 3.3. ISSF variations K_σ^A , K_σ^E , K_σ^{E*} by varying l_b when $l_g = 20\mu\text{m}$ in micro-bond test

Chapter 3

Table 3.3. ISSF variations $K_{\sigma}^A, K_{\sigma}^E, K_{\sigma}^{E^*}$ [$MPa \cdot m^{1-0.6592}$] by varying l_b when $l_g = 20\mu m$ in micro-bond test, (): ISSF ratio variations $K_{\sigma}^A/K_{\sigma}^E$ and $K_{\sigma}^{E^*}/K_{\sigma}^E$ by varying l_b

l_b [μm]	K_{σ}^E ($K_{\sigma}^E/K_{\sigma}^E$)	K_{σ}^A ($K_{\sigma}^A/K_{\sigma}^E$)	$K_{\sigma}^{E^*}$ ($K_{\sigma}^{E^*}/K_{\sigma}^E$)
100	0.680 (1.000)	-0.324 (-0.476)	0.433 (0.637)
150	0.562 (1.000)	-0.179 (-0.318)	0.389 (0.691)
200	0.515 (1.000)	-0.124 (-0.240)	0.364 (0.707)
400	0.448 (1.000)	-0.0498 (-0.111)	0.326 (0.728)

To clarify the relation between K_{σ}^E at Point E in micro-bond test and $K_{\sigma}^{E^*}$ at Point E* in pull-out test, Table 3.3 and Fig. 3.4 shows ISSF ratios $-K_{\sigma}^A/K_{\sigma}^E$ and $K_{\sigma}^{E^*}/K_{\sigma}^E$. As shown in Table 3.3 and Fig. 3.4, the ratio $-K_{\sigma}^A/K_{\sigma}^E$ decreases significantly with increasing l_b . Instead, the ratio $K_{\sigma}^{E^*}/K_{\sigma}^E$ is almost constant as $K_{\sigma}^{E^*}/K_{\sigma}^E \cong 0.75$. In other words, the ISSF at Point E in micro-bond test is about 1.5 times of that at Point E* in pull-out test. As, pull-out is relatively complex compared to the micro-bond test. The pull-out test require large size of the matrix and a complex cure procedure^{35),39)}. While the micro-bond test is relatively simpler and easier compared to the pull-out test. Besides, there is more experiment study of micro-bond tests available. From the ISSF results, the micro-bond test and pull-out test are almost proportional under idealized situation. Therefore, the results of the pull-out test can be predicted by the results of micro-bond test of same material and fiber geometry.

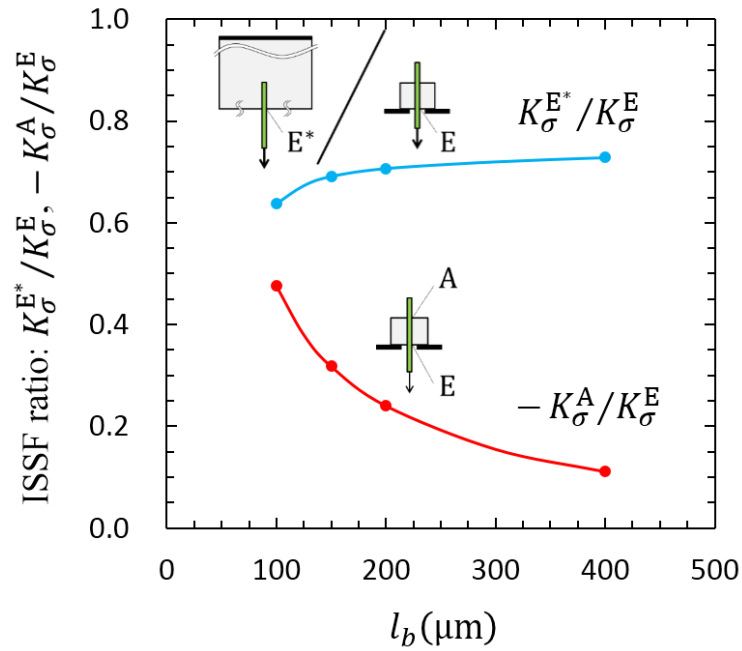


Fig. 3.4. ISSF ratio variations by varying l_b when $l_g = 20\mu\text{m}$

3.3.2 Effect of knife gap opening l_g on ISSF in micro-bond test

Table 3.4 and Fig. 3.5 illustrate the ISSF K_{σ}^E by varying knife gap opening l_g assuming the droplet dimensions $l_b = 100\mu\text{m}, 200\mu\text{m}, 400\mu\text{m}$. The result $l_b = 100\mu\text{m}$ can be shown in the range $l_g \leq 40\mu\text{m}$ because larger $l_g > 40\mu\text{m}$ cannot support the smaller droplet size $l_b = 100\mu\text{m}$. In the previous experiment^{(34),(35),(56),(57),(73)–(75)}, the bonded length l_b , which is nearly equal to the droplet size, was in the range $l_b = 50\mu\text{m} \sim 400\mu\text{m}$ in most cases.

In Fig. 3.5, when $l_g \leq 10\mu\text{m}$, the ISSF K_{σ}^E increases significantly with decreasing the knife gap opening l_g . In other words, when $l_g \leq 10\mu\text{m}$, the ISSF K_{σ}^E is sensitive to l_g although when $l_g \geq 10\mu\text{m}$, the ISSF K_{σ}^E is nearly independent of l_g . When $l_b = 100\mu\text{m}$, the ISSF increases slightly with increasing l_g because of the bend deformation of the small size droplet $l_b = 100\mu\text{m}$. Since many previous tests were conducted under $l_g \leq 10\mu\text{m}$ ^{(77)–(79)}, the initial debonding condition varies depending on l_g whose slight change affects the ISSF. Therefore, as a conclusion, the micro-bond testing geometry $l_g \geq 10\mu\text{m}$ is recommended since the ISSF K_{σ}^E becomes almost constant as shown in Fig. 3.5. In the experiments, no droplet fracture should be confirmed instead of the interface debonding since the sphered

droplet shape is deformed due to the knife edge support.

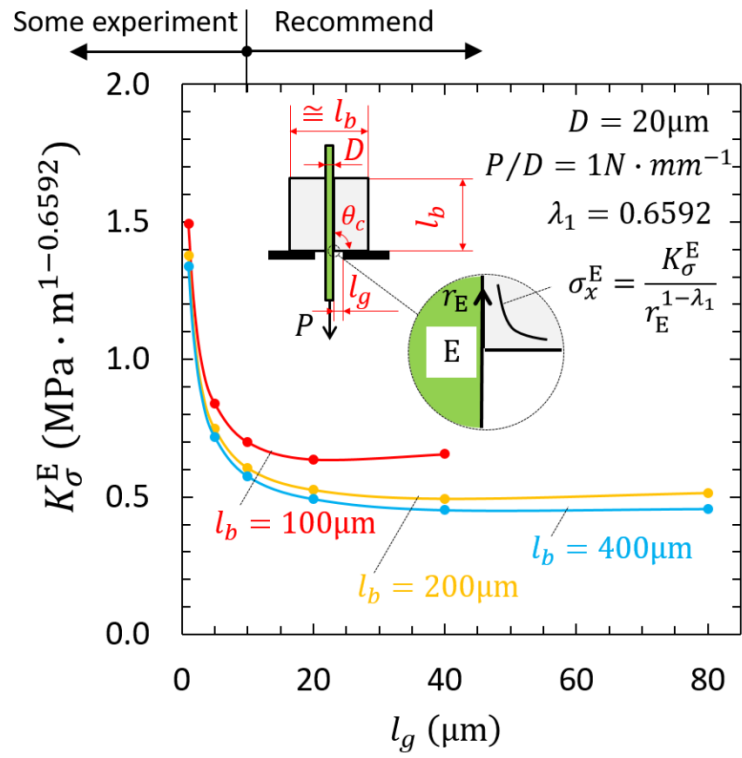


Fig. 3.5. ISSF variation K_σ^E by varying l_g when $l_b = 100\mu\text{m}, 200\mu\text{m}, 400\mu\text{m}$

Table 3.4. ISSF variation K_{σ}^E [$MPa \cdot m^{1-0.6592}$] by varying l_g (·):
 $K_{\sigma}^E|_{l_b}/K_{\sigma}^E|_{l_b=100\mu m}$.

l_b [μm]	l_g [μm]	1	5	10	20	40	80
100		1.492	0.840	0.700	0.637	0.656	–
		(1.000)	(1.000)	(1.000)	(1.000)	(1.000)	(–)
200		1.377	0.749	0.606	0.526	0.494	0.515
		(0.923)	(0.891)	(0.866)	(0.826)	(0.753)	(–)
400		1.337	0.718	0.576	0.493	0.452	0.457
		(0.896)	(0.855)	(0.822)	(0.773)	(0.689)	(–)

3.3.3 Resin deformation and fiber elongation in micro-bond test

To understand the geometrical effect in micro-bond test, the matrix surface deformation is studied in this section. Fig. 3.6 illustrates the displacement $u_y^E(x)$ when $P = 1MPa \times 0.02mm \times 1mm = 0.02N$, $l_b = 100\mu m$ and $l_b = 400\mu m$ using the cartesian coordinate system in Fig. 3.6 where the x-axis is the distance from Point E ($x = 0$) until the knife edge ($x = l_g$). At the knife edge $x \geq l_g$, the displacement in the y-direction is constrained with no shear stress as $u_y = 0$, $\tau_{xy} = 0$. The deformation when $l_b = 400\mu m$ is relatively smaller than the deformation when $l_b = 100\mu m$.

Table 3.5 shows displacement $u_y^E(0)$ at the entry Point E, displacement $u_y^A(0)$ at the exit Point A, and fiber elongation $u_y^E(0) - u_y^A(0)$. Table 3.5 also shows the contact angle change defined as $\Delta\theta_C = \tan^{-1}[du_y^E(0)/dx]$ at Point E. Fig. 3.7 shows $u_y^E(0)$ and $u_y^A(0)$ both of which increase with increasing l_g although Table 3.5 shows K_{σ}^E decreases with increasing l_g . Since the ratio $u_y^E(0)/K_{\sigma}^E$ is not constant as shown in Table 3.5, $u_y^E(0)$ is not controlled by the ISSF K_{σ}^E . Instead, as shown in Table 3.5 and Fig. 3.8, the ratio $K_{\sigma}^E/\Delta\theta_C$ is almost constant, and therefore, K_{σ}^E is almost controlled by $\Delta\theta_C$.

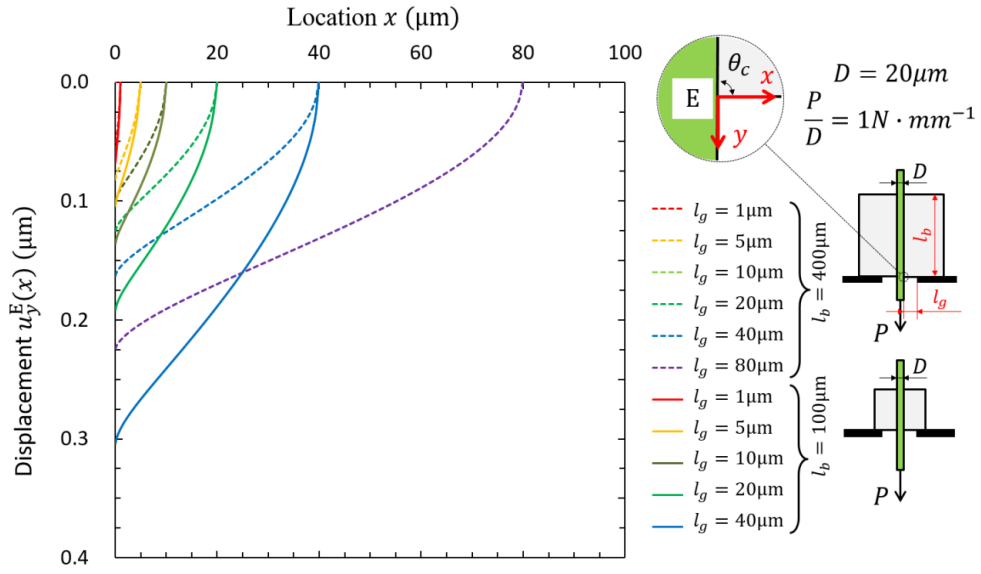


Fig. 3.6. Fiber deformation at the unrestrained surface by varying knife gap opening l_g for $l_b = 100\mu\text{m}$ and $l_b = 400\mu\text{m}$

Chapter 3

Table 3.5a. Fiber deformation when $l_b = 100\mu\text{m}$

Knife gap opening l_g (μm)	1	5	10	20	40	80
K_σ^E	1.492	0.840	0.700	0.637	0.656	—
Displacement $u_y^E(0)$ (μm)	0.0675	0.1041	0.1362	0.1919	0.3042	—
Displacement $u_y^A(0)$ (μm)	0.0593	0.0908	0.1201	0.1729	0.2831	—
Fiber elongation $\Delta l_b = u_y^E - u_y^A$	0.0082	0.0133	0.0161	0.0190	0.0211	—
θ_C after deformation	67.1°	76.7°	78.8°	79.8°	79.5°	—
$\Delta\theta_C$ $= \tan^{-1} \left[\frac{du_y^E(0)}{dx} \right]$	22.9°	13.3°	11.2°	10.2°	10.5°	—
$u_y^E(0)/K_\sigma^E$	0.0452	0.1240	0.1945	0.3013	0.4636	—
$K_\sigma^E/\Delta\theta_C$	0.0652	0.0632	0.0625	0.0625	0.0625	—

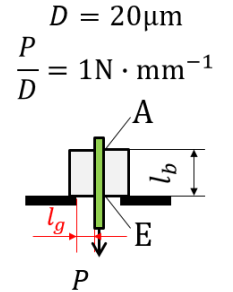
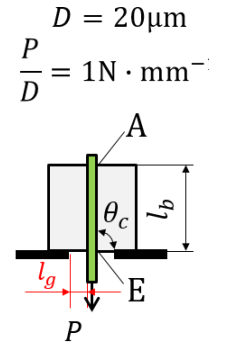


Table 3.5b. Fiber deformation when $l_b = 400\mu\text{m}$

Knife gap opening l_g (μm)	1	5	10	20	40	80
K_σ^E	1.337	0.718	0.576	0.493	0.452	0.457
Displacement $u_y^E(0)$ (μm)	0.0575	0.0821	0.1004	0.1254	0.1628	0.2241
Displacement $u_y^A(0)$ (μm)	0.0349	0.0495	0.0611	0.0781	0.1058	0.1566
Fiber elongation $\Delta l_b = u_y^E - u_y^A$	0.0226	0.0326	0.0393	0.0473	0.0570	0.0675
θ_C after deformation	70.2°	79.2°	81.4°	82.8°	83.5°	83.8°
$\Delta\theta_C$ $= \tan^{-1} \left[\frac{du_y^E(0)}{dx} \right]$	19.8°	10.8°	8.6°	7.2°	6.5°	6.2°
$u_y^E(0)/K_\sigma^E$	0.0430	0.1144	0.1744	0.2545	0.3598	0.4906
$K_\sigma^E/\Delta\theta_C$	0.0674	0.0667	0.0672	0.0682	0.0700	0.0740



The reason why the ISSF K_σ^E becomes larger as $l_g \rightarrow 0$ in Fig. 3.5 can be explained from the surface angle after deformation defined as $\Delta\theta_C = \tan^{-1} \left[\frac{du_y^E(0)}{dx} \right]$. When the knife edge gap $l_g \rightarrow 0$ in micro-bond test, the surface angle after deformation $\Delta\theta_C = \tan^{-1} \left[\frac{du_y^E(0)}{dx} \right]$ becomes larger as shown in Table 3.5 and Fig. 3.6. This is because the fiber is pulled-out under

the small knife gap opening $l_g \rightarrow 0$ (see Fig. 6, for example, when $l_g = 1\mu\text{m}$). Some previous experimental studies suggested that the knife edge gap l_g should be as small as possible ^{77)–79)}. To obtain the general results independent of l_g , however, a certain gap should be kept in micro-bond test in Fig. 3.1.

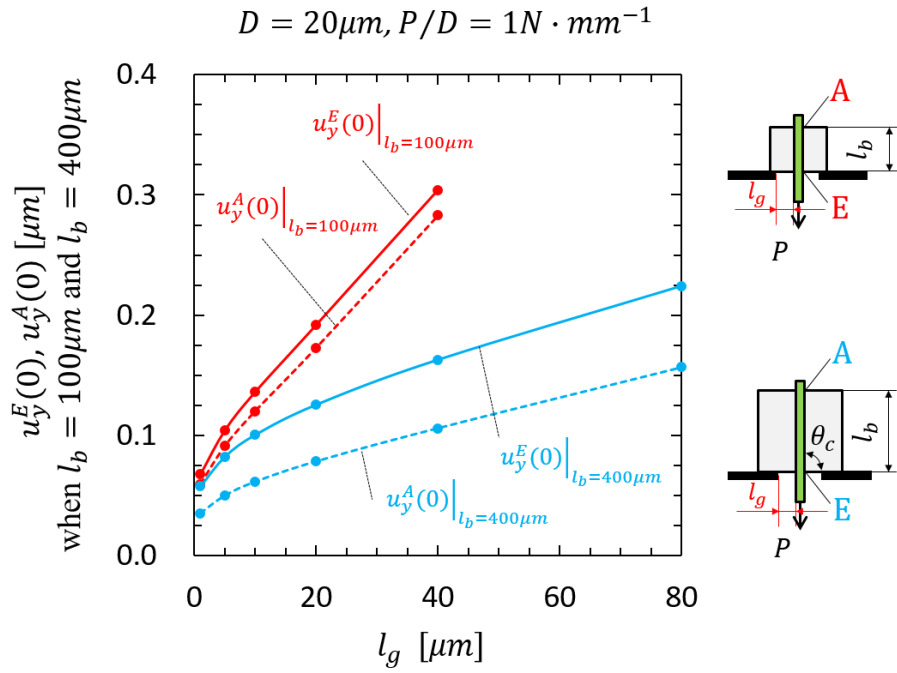


Fig. 3.7. Surface displacement $u_y^E(0)$ and $u_y^A(0)$ by varying knife gap opening l_g when $l_b = 100\mu\text{m}$ and $l_b = 400\mu\text{m}$.

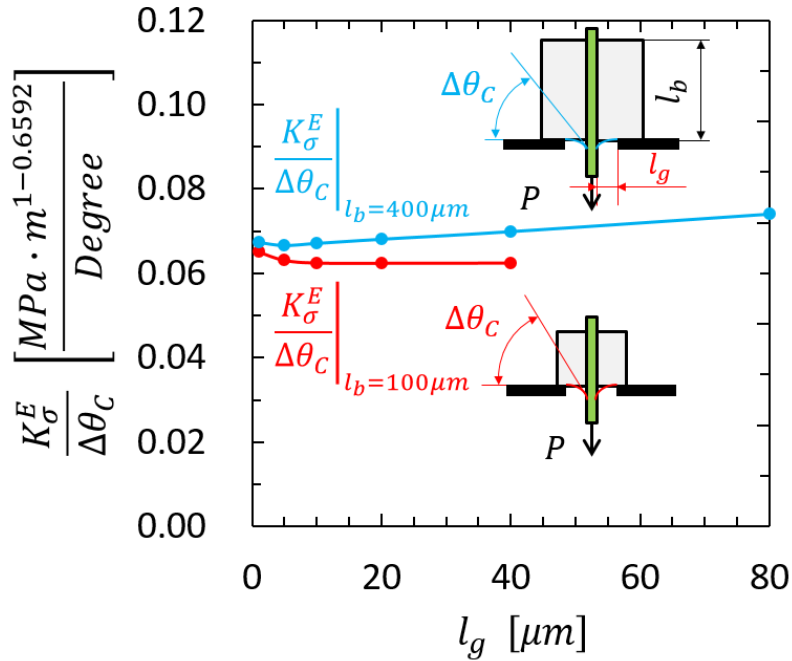


Fig. 3.8. ISSF ratio $K_\sigma^E/\Delta\theta_C$ is almost constant independent of l_g

3.3.4 Effect of knife edge friction on ISSF in micro-bond test

In the above discussion, no friction condition $\mu = 0$ is assumed by applying $u_y = 0$, $\tau_{xy} = 0$ along the knife edge shown in black in Fig. 3.1. In real micro-bond test, however, the knife edge restrains the y-displacement as $u_y = 0$ with a certain frictional stress as $\tau_{xy} \neq 0$. Since the friction coefficient μ is unknown, in this section, along the knife edge, assume another condition $u_y = 0$, $u_x = 0$, which is corresponding to $\mu \rightarrow \infty$ along the knife edge. Fig. 3.9 compares the two different boundary conditions under the fixed dimensions $D = 20\mu\text{m}$ and $l_b = 400\mu\text{m}$. The solid line represents the ISSF K_σ^E when the droplet is supported as $u_y = 0$, $\tau_{xy} = 0$ by the knife edge. And the dashed line represents the ISSF K_σ^E when the droplet is supported as $u_y = 0$, $u_x = 0$. The ISSF of real experiment with friction can be plotted between those two lines expressing extreme cases. Since the ISSF K_σ^E under $u_y = 0$, $\tau_{xy} = 0$ is the most severe, this boundary condition is adopted in this study.

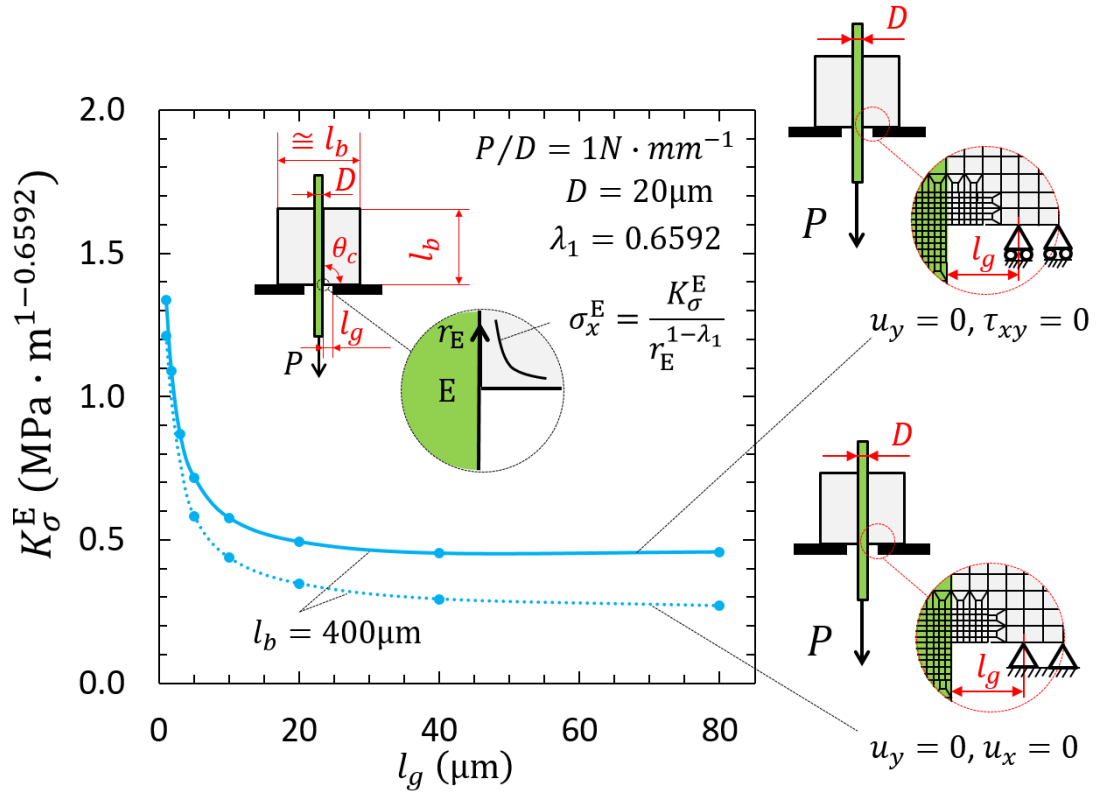


Fig. 3.9. Effect of friction on the knife edge on the ISSF in micro-bond test by comparing $\mu = 0$ ($u_y = 0, \tau_{xy} = 0$) and $\mu \rightarrow \infty$ ($u_y = 0, u_x = 0$)

3.4. Conclusions

Micro-bond test has been used to investigate fiber/matrix bonding behavior without considering the singular stress. This paper newly analyzed the intensity of singular stress field (ISSF) at the fiber entry point under tension and the ISSF at the fiber exit point under compression. The results showed that no matter how the fiber bond length l_b changes, the fiber entry point is more dangerous in micro-bond test. Instead, in a fiber pull-out test, the fiber end point can be more dangerous if the embedded length is shorter. The ISSF at the entry point in micro-bond test is about 1.5 times of the ISSF of pull-out test at the entry point under the same geometries D and l_b . By using this knowledge, the ISSFs of pull-out test can be predicted from micro-bond test. Care should be taken for the small knife gap opening $l_g \leq 10\mu\text{m}$ popularly used in micro-bond testing because the ISSF K_{σ}^E is sensitive to l_g . Instead, testing geometry

$l_g \geq 10\mu\text{m}$ can be recommended since the ISSF K_σ^E is nearly independent of l_g .

Appendix 3.A: Modelling of a single fiber pull-out embedded in a semi-infinite region.

Fig. 3.2 shows the pull-out test of a single fiber partially embedded in a semi-infinite resin matrix region studied in the previous paper [33, 34]. Here, Point A^* denotes the fiber end, and Point E^* denotes the fiber/surface entry point. Notation l_b denotes the axial bonded length from the end Point A^* to the entry Point E^* before applying load P . Notation l_M denote the size of the matrix. ISSF at Point A^* and Point E^* in pull-out model were discussed. Point E^* is more severe than Point A^* , if l_b is large enough. A two-dimensional rectangular shaped fiber was considered in the matrix whose size l_M in Fig. 3.2 is set as $l_M = 4000D$ ⁷²). Table 3.A.1 shows the stress $\sigma_{x,FEM}^{E^*}(r_{E^*})$ near Point E^* in Fig. 3.2 by varying the matrix size l_M . It is seen that $l_M = 4000D$ is large enough to express the semi-infinite region since the stress $\sigma_{x,FEM}^{E^*}(r_{E^*})$ is the same when $l_M \geq 4000D$.

Table 3.A.1 FEM Stress $\sigma_{x,FEM}^{E^*}(r_{E^*})$ [MPa] in Fig. 3.2.

l_M	2000D	4000D	6000D
$r_{E^*}/e_{min} = 0.0$	0.763	0.771	0.771
$r_{E^*}/e_{min} = 0.5$	0.651	0.658	0.658
$r_{E^*}/e_{min} = 1.0$	0.477	0.482	0.482
$r_{E^*}/e_{min} = 1.5$	0.397	0.401	0.401
$r_{E^*}/e_{min} = 2.0$	0.374	0.378	0.378

Appendix 3.B: An example of FEM mesh and stress distributions for the micro-bond test.

Fig. 3.B.1 shows an example of FEM mesh. Smaller mesh is applied at the interface corner. The minimum element size $e_{min} = 3^{-9}D$ and $e_{min} = 3^{-10}D$ are chosen confirming the mesh independency. To represent the knife edge support in Fig. 3.1, the y-direction displacement is fixed with no shear stress as shown in Fig. 3.B.1. The distance from the knife edge to the fiber surface is denoted by l_g .

Fig. 3.B.2 (a) shows the FEM stress $\sigma_{x,FEM}$ distribution when $e_{min} = 3^{-9}D$, $l_b = 100\mu\text{m}$ and $l_g = 20\mu\text{m}$ focusing on Point E and Point A. The stress $\sigma_{x,FEM}$ around Point E is under

tension and the stress $\sigma_{x,FEM}$ around Point A is under compression. Fig. 3.B.3 shows the stress $\sigma_{x,FEM}(y)$ and the shear stress $\tau_{yx,FEM}(y)$ along the entire fiber/droplet interface. Here, the y -coordinate indicates the location from Point A at $y = 0$ to Point E at $y = 100\mu\text{m}$. Since the stress at the vicinity of Point A and Point E goes to infinity, minimum element size $e_{min} = 3^{-9}D$ is used around the singular points in Fig. 3.B.1.

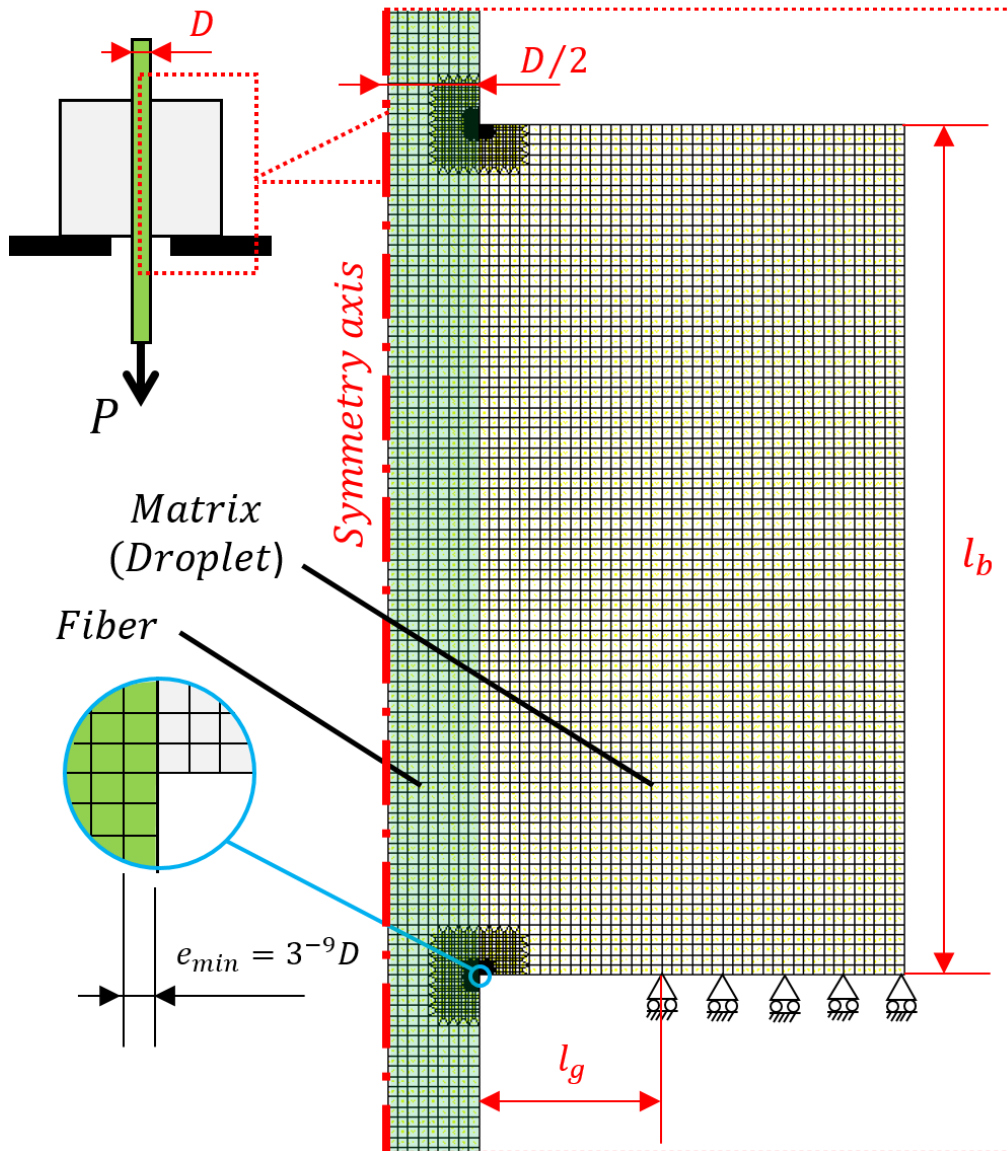


Fig. 3.B.1 An example of FEM mesh whose minimum element size $e_{min} = 3^{-9}D$.

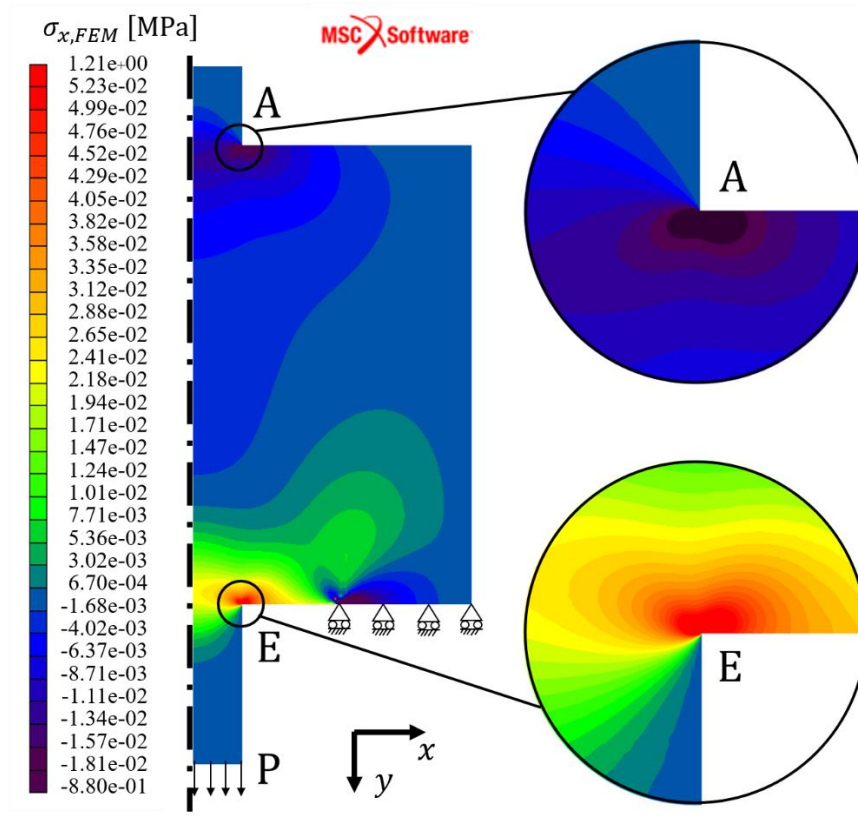


Fig. 3.B.2 FEM stress $\sigma_{x,FEM}^{A,E}$ when $e_{min} = 3^{-9}D$, $l_b = 100\mu\text{m}$ and $l_g = 20\mu\text{m}$

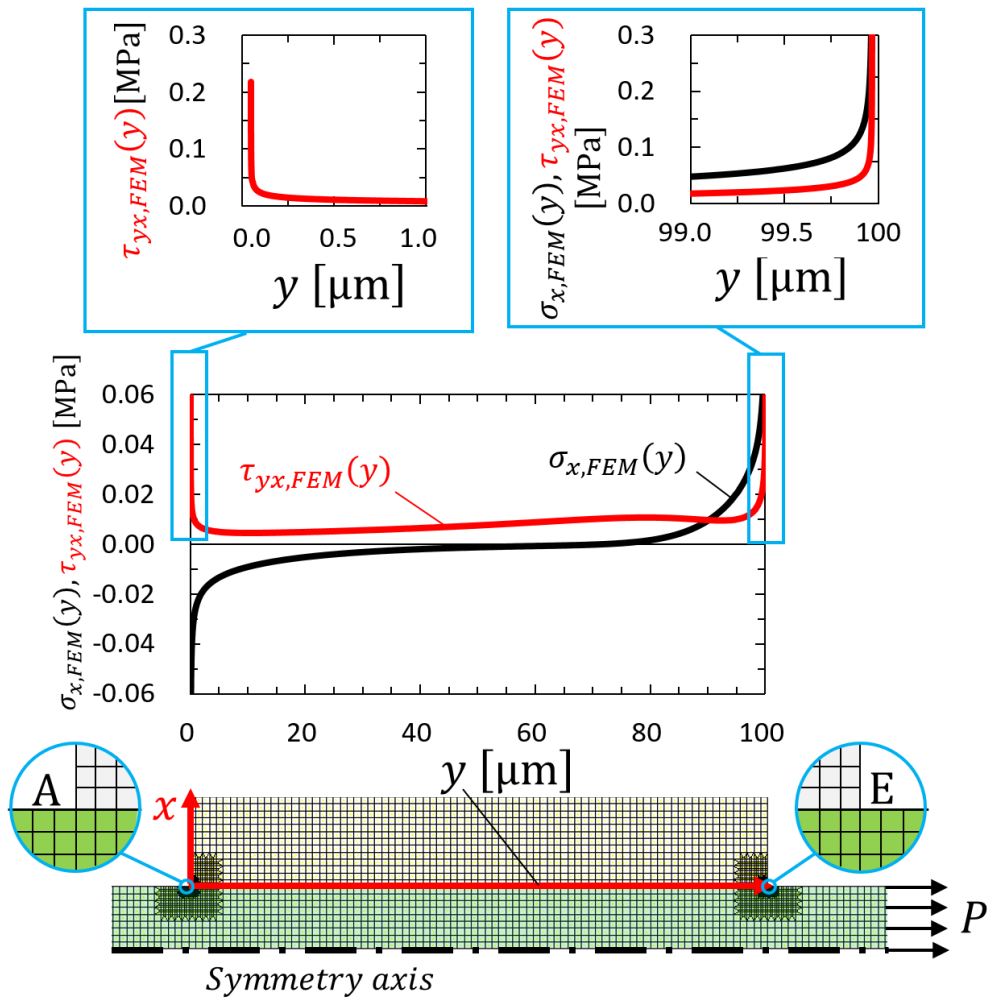


Fig. 3.B.3 FEM stress $\sigma_{x,FEM}^{A,E}$ and $\tau_{xy,FEM}^{A,E}$ when $e_{min} = 3^{-9}D$, $l_b = 100\mu\text{m}$ and $l_g = 20\mu\text{m}$ along the entire fiber/matrix interface.

Chapter 4 Material Combination Effects on ISSFs in Pull-out Test and Micro-bond Test

4.1 Carbon fiber/Epoxy vs. Glass fiber/Epoxy

In Chapter 2, the ISSFs in pull-out test were studied for Glass fiber/Epoxy as shown in Table 4.1. ISSFs in micro-bond test for Glass fiber/Epoxy were studied in Chapter 3. In this chapter, ISSFs in pull-out test and micro-bond test will be studied for Carbon fiber/Epoxy, to investigate the material combination effects on the ISSFs. Detail mechanical properties of the two material are shown in Table 4.1.

Table 4.1. Mechanical properties

Fiber/Matrix	(a): Carbon Fiber/ Epoxy	(b): Glass Fiber/ Epoxy
E_F (GPa)	276	75
E_M (GPa)	3.03	3.3
ν_F	0.30	0.17
ν_M	0.35	0.35
α	0.9775	0.9071
β	0.2250	0.2016
λ_1^A	0.7784	0.7632
λ_2^A	0.6158	0.6218
λ_1^E	0.6751	0.6592
λ_2^E	0.9999	0.9992
D (μm)	20	20

4.1 ISSF at Point A in pull-out test

Table 4.2 and Fig. 4.1(a) show the ISSFs denoted by $K_{\sigma, \lambda_1^A}^A, K_{\sigma, \lambda_2^A}^A, K_{\tau, \lambda_1^A}^A, K_{\tau, \lambda_2^A}^A$ ³¹⁾ at Point A for carbon fiber/epoxy by varying l_{in} varies from 50 μm to 1000 μm . And Fig. 4.1(b) show the ISSFs for glass fiber/epoxy. It is seen that ISSFs decrease with increasing l_{in} . This is consistent with the experimental results showing that the maximum pull-out force increases with increasing l_{in} ^{34),75)}.

By assuming the total fiber length of $l = 600 \mu\text{m}$, the ISSFs are compared when $l_{in} = 150 \mu\text{m}$ (1/4 embedded length) and $l_{in} = 300 \mu\text{m}$ (1/2 embedded length). As shown in Table 4.2 for carbon fiber/epoxy, mode I ISSF, $K_{\sigma,\lambda_1^A}^A = 0.0875$ at $l_{in} = 300 \mu\text{m}$ is 30.6% smaller than $K_{\sigma,\lambda_1^A}^A = 0.126$ at $l_{in} = 150 \mu\text{m}$ and the mode II ISSF $K_{\sigma,\lambda_2^A}^A = 0.134$ at $l_{in} = 300 \mu\text{m}$ is 27.6% smaller than $K_{\sigma,\lambda_2^A}^A = 0.185$ at $l_{in} = 150 \mu\text{m}$.

For glass fiber/epoxy, mode I ISSF $K_{\sigma,\lambda_1^A}^A = 0.0767$ at $l_{in} = 300 \mu\text{m}$ is 36.1% smaller than $K_{\sigma,\lambda_1^A}^A = 0.120$ at $l_{in} = 150 \mu\text{m}$. Regarding Mode II ISSF, $K_{\sigma,\lambda_2^A}^A = 0.139$ at $l_{in} = 300 \mu\text{m}$ is 32.8% smaller than $K_{\sigma,\lambda_2^A}^A = 0.207$ at $l_{in} = 150 \mu\text{m}$.

Table 4.2. ISSFs at Point A, $K_{\sigma,\lambda_1^A}^A$, $K_{\sigma,\lambda_2^A}^A$, $K_{\tau,\lambda_1^A}^A$, $K_{\tau,\lambda_2^A}^A$ in Fig. 2.1 for Carbon fiber/Epoxy in Table 4.1(a).

l_{in} [μm]	$K_{\sigma,\lambda_1^A}^A$ [$\text{MPa} \cdot \text{m}^{1-0.7784}$]	$K_{\sigma,\lambda_2^A}^A$ [$\text{MPa} \cdot \text{m}^{1-0.6158}$]	$K_{\tau,\lambda_1^A}^A$ [$\text{MPa} \cdot \text{m}^{1-0.7784}$]	$K_{\tau,\lambda_2^A}^A$ [$\text{MPa} \cdot \text{m}^{1-0.6158}$]
50	0.214	0.288	0.126	0.182
100	0.154	0.224	0.0907	0.141
150	0.126	0.185	0.0742	0.117
200	0.109	0.163	0.0642	0.103
250	0.0970	0.147	0.0572	0.0929
300	0.0875	0.134	0.0516	0.0846
350	0.0805	0.124	0.0475	0.0785
400	0.0749	0.116	0.0441	0.0733
450	0.0698	0.109	0.0411	0.0687
500	0.0658	0.103	0.0388	0.0650
1000	0.0430	0.0689	0.0253	0.0435

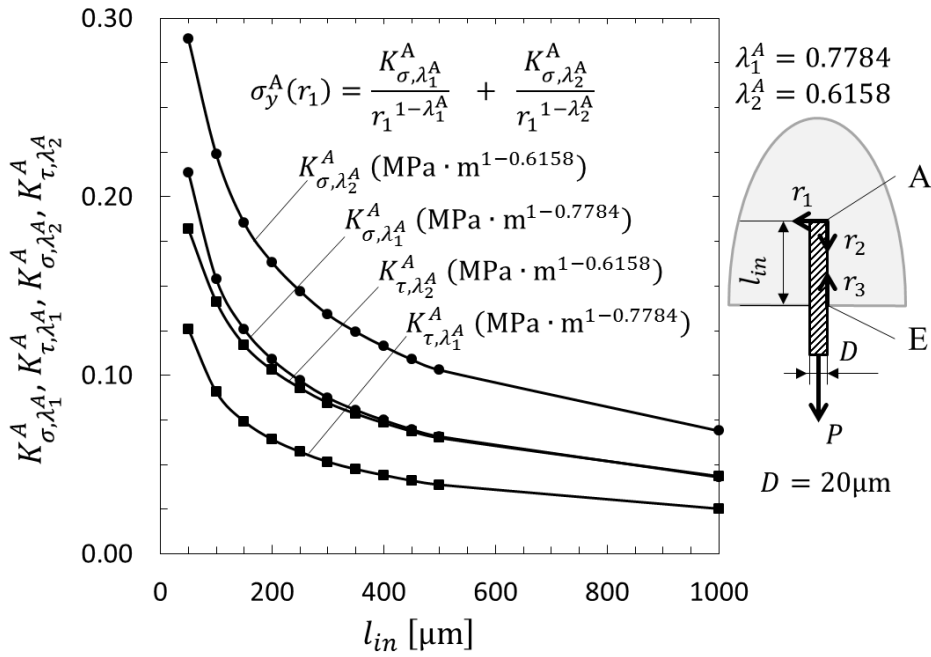


Fig. 4.1(a). ISSFs at Point A vs. embedding length for Carbon Fiber/Epoxy

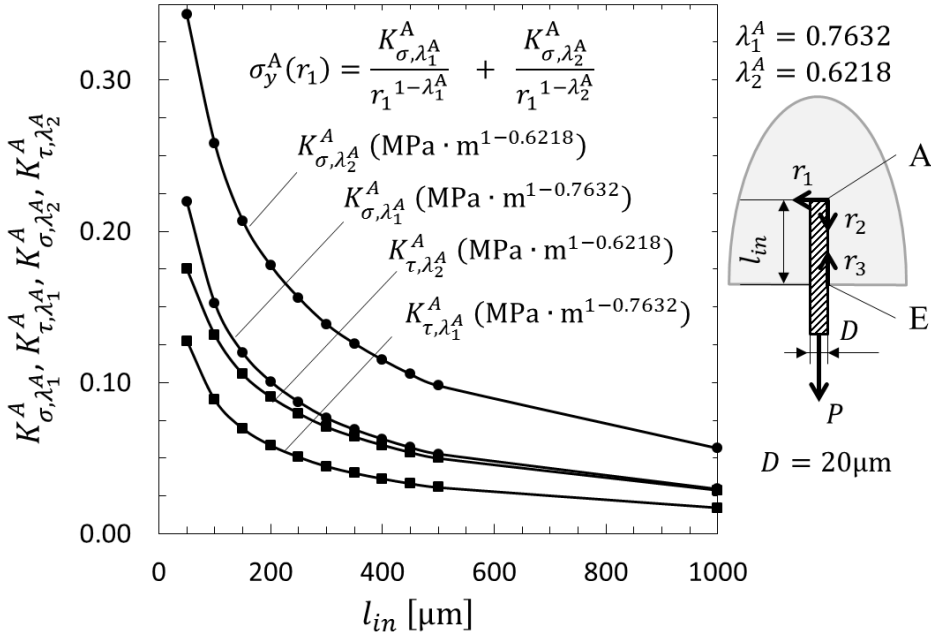


Fig. 4.1(b). ISSFs at Point A vs. embedding length for Glass Fiber/Epoxy

4.2 ISSF at Point E in Pull-out test

Table 4.3 and Fig. 4.2(a) shows ISSFs $K_{\sigma,\lambda_1^E}^E \square K_{\sigma,\lambda_2^E}^E$ at Point E for carbon fiber/epoxy by varying l_{in} from 50 μm to 1000 μm . Regarding the first term $K_{\sigma,\lambda_1^E}^E$ in Equation (2.9) for carbon fiber/epoxy, $K_{\sigma,\lambda_1^E}^E = 0.223$ at $l_{in} = 300 \mu\text{m}$ is 23.4% smaller than $K_{\sigma,\lambda_1^E}^E = 0.291$ at $l_{in} = 150 \mu\text{m}$.

For glass fiber/epoxy, $K_{\sigma,\lambda_1^E}^E = 0.339$ at $l_{in} = 300 \mu\text{m}$ is 12.9% smaller than $K_{\sigma,\lambda_1^E}^E = 0.389$ at $l_{in} = 150 \mu\text{m}$.

Table 4.3. ISSFs at point E, $K_{\sigma,\lambda_1^E}^E$, $K_{\sigma,\tau_1^E}^E$ in Fig. 2.1 for Carbon fiber/Epoxy in Table 4.1(a).

l_{in} [μm]	$K_{\sigma,\lambda_1^E}^E$ [$\text{MPa} \cdot \text{m}^{1-0.6752}$]	$K_{\tau,\lambda_1^E}^E$ [$\text{MPa} \cdot \text{m}^{1-0.6752}$]
50	0.470	0.166
100	0.346	0.122
150	0.291	0.103
200	0.259	0.0915
250	0.238	0.0840
300	0.223	0.0787
350	0.212	0.0747
400	0.203	0.0717
450	0.196	0.0693
500	0.191	0.0674
1000	0.170	0.0599

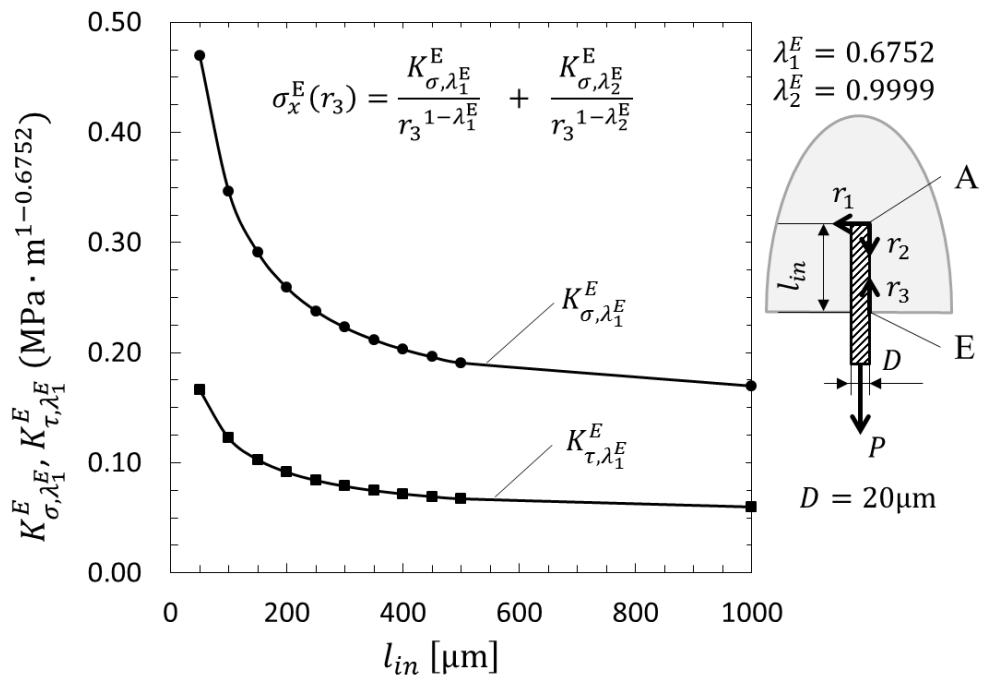


Fig. 4.2(a). ISSFs at Point E vs. embedding length for Carbon Fiber/Epoxy

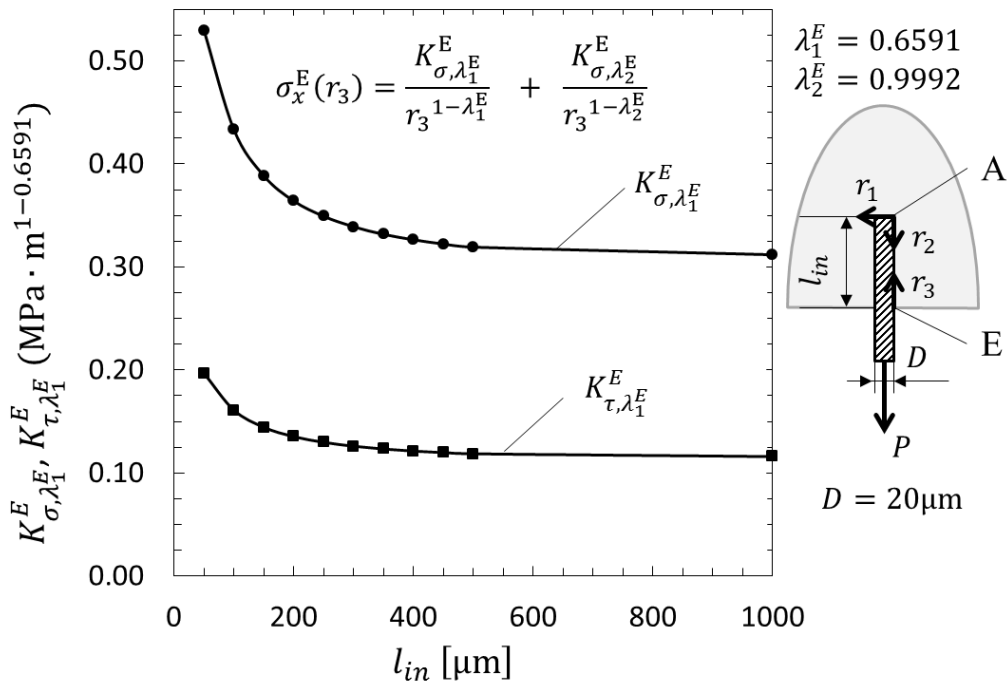


Fig. 4.2(b). ISSFs at Point E vs. embedding length for Glass Fiber/Epoxy

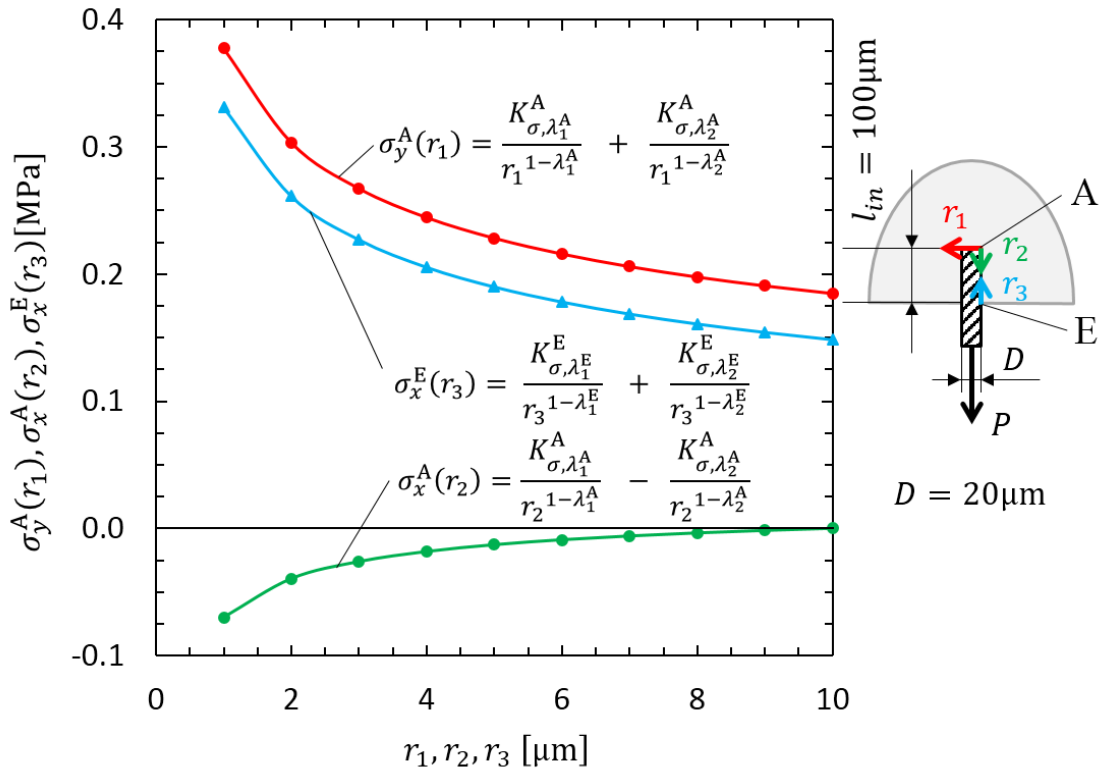


Fig. 4.3. Stress distributions when $l_{in} = 100 \mu\text{m}$ for Carbon Fiber/Epoxy

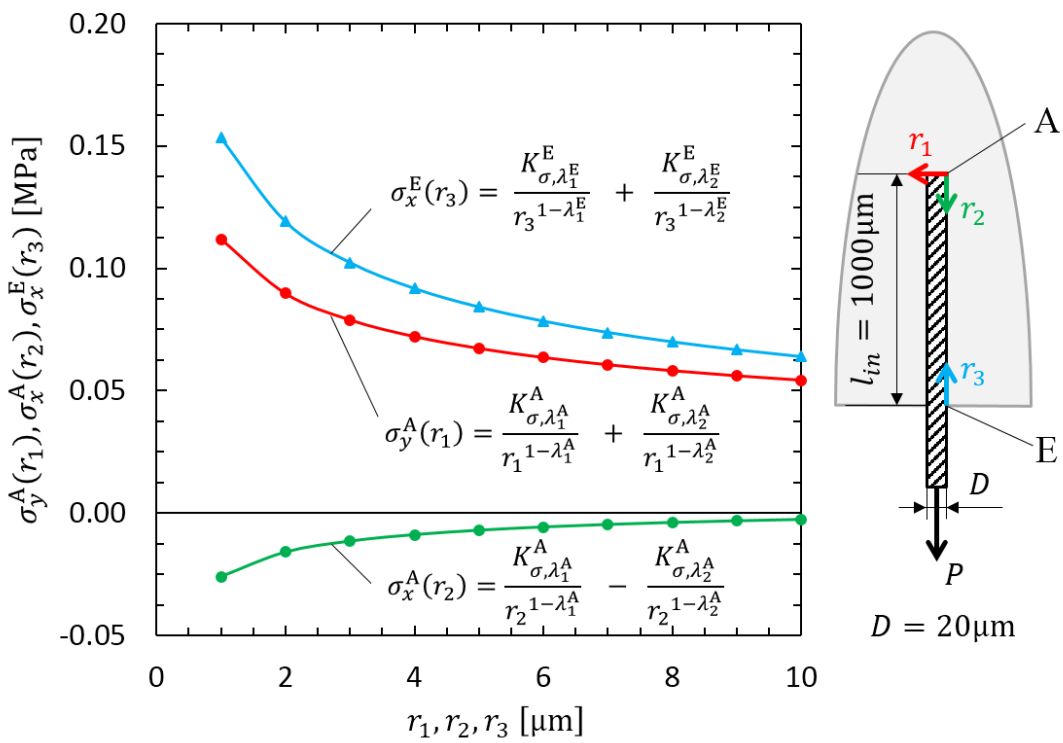


Fig. 4.4. Stress distributions when $l_{in} = 1000 \mu\text{m}$ for Carbon Fiber/Epoxy

Similar to the Glass fiber/Epoxy, the normal stress distributions along the interfaces between the fiber and matrix are studied for Carbon fiber/Epoxy. Normal stress distribution $\sigma_y^A(r_1)$ and $\sigma_x^E(r_3)$ are mainly compared in the following discussion. As shown in Fig. 4.3 for carbon fiber/epoxy when $l_{in} = 100 \mu\text{m}$, since the stress $\sigma_y^A(r_1)$ at Point A is larger than the stress $\sigma_x^E(r_3)$ at Point E, debonding may occur at Point A earlier. On the other hand, when $l_{in} = 1000 \mu\text{m}$ in Fig. 4.4, since the stress $\sigma_x^E(r_3)$ at point E is larger than the stress $\sigma_y^A(r_1)$ at point A, debonding may occur earlier at Point E. These phenomena is same for the two material combination as shown in Table 4.1.

Fig. 4.5 shows the comparison of stress $\sigma_y^A(r_1)$ at $r_1 = 1\mu\text{m}$ close to Point A and the stress $\sigma_x^E(r_3)$ at $r_3 = 1\mu\text{m}$ close to Point E by varying l_{in} . The fixed position $r_1 = r_3 = 1\mu\text{m}$ is selected to compare the different results of Carbon fiber/Epoxy and Glass fiber/Epoxy. In Fig. 4.5(a) when $l_{in} = 450\mu\text{m}$, the severity at Point A and Point E is almost the same for carbon fiber/epoxy based on the assumption $\sigma_y^A(r_1)|_{r_1=1\mu\text{m}} = \sigma_x^E(r_3)|_{r_3=1\mu\text{m}}$. As shown in Fig. 4.5(b), when $l_{in} = 150\mu\text{m}$, the severities of Point A and Point E are almost the same for glass fiber/epoxy.

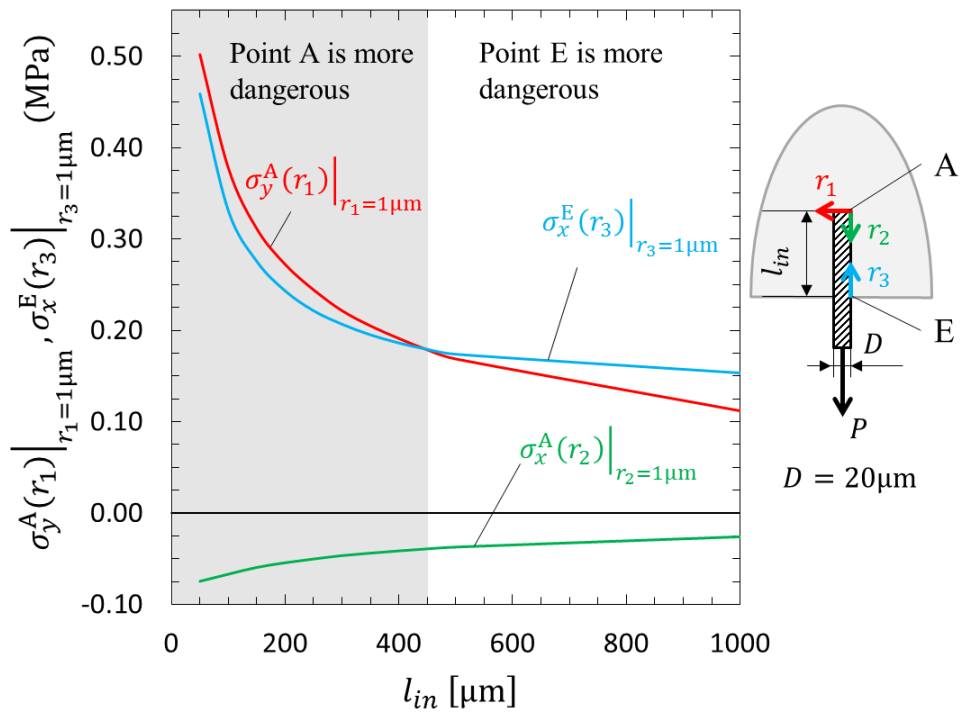


Fig. 4.5(a). Stress at $r = 1 \mu\text{m}$ of different embedding length for Carbon Fiber/Epoxy

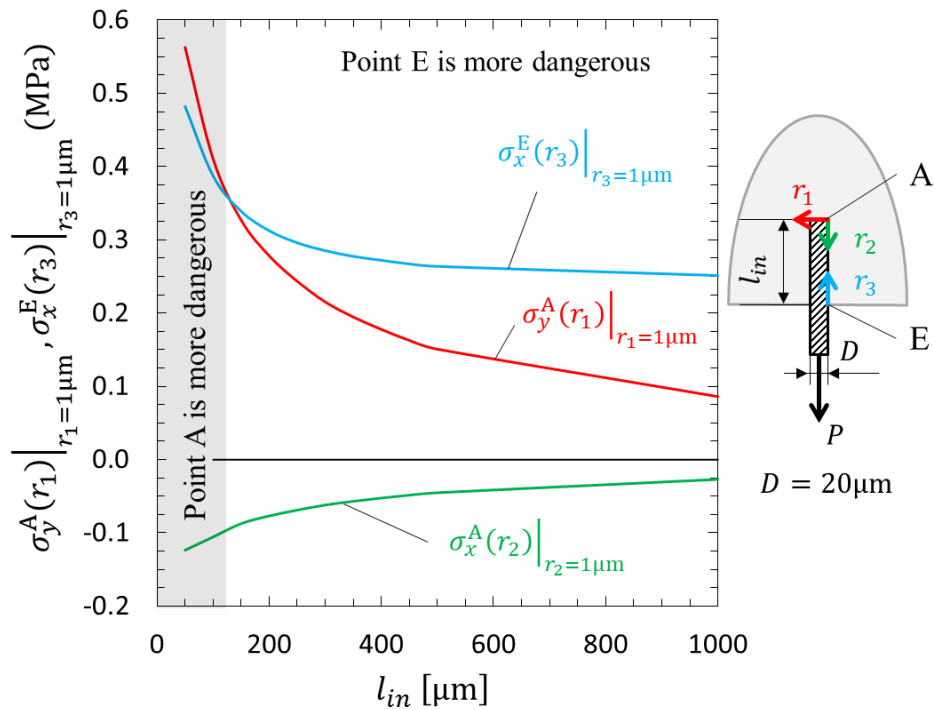


Fig. 4.5(b). Stress at $r = 1 \mu\text{m}$ of different embedding length for Glass Fiber/Epoxy

4.3 ISSF in micro-bond test for Carbon fiber/Epoxy in comparison with Glass fiber/Epoxy

In Chapter 3, for the glass fiber/epoxy in Table 4.1(b), the effect of knife gap opening l_g on the ISSF K_σ^E was discussed. Then, it was found that when $l_g \leq 10\mu\text{m}$ commonly used, the ISSF K_σ^E is very sensitive to l_g . As a conclusion, $l_g \geq 10\mu\text{m}$ is recommended for suitable testing geometry since the ISSF K_σ^E becomes almost constant. To verify this conclusion, for carbon fiber/epoxy in Table 4.1(a), the effect of knife gap opening l_g on the ISSF K_σ^E was discussed as shown in Table 4.4 and Fig. 4.6(a). Here, the singular index for Carbon fiber/Epoxy at Point E is $\lambda_{1,C} = 0.6751$ instead of the singular index for Glass fiber/Epoxy $\lambda_{1,g} = 0.6592$. Table 4.4 and Fig. 4.6(a) illustrate the ISSF K_σ^E by varying knife gap opening l_g when the droplet dimensions $l_b = 100\mu\text{m}, 200\mu\text{m}, 400\mu\text{m}$ in a similar way of Fig. 4.6(b) of Glass fiber/Epoxy. Effect of l_g on the ISSF results in Fig. 4.6(a) is similar to Fig. 4.6(b) since the ISSF K_σ^E is sensitive to l_g when $l_g \leq 10\mu\text{m}$ and almost independent of l_g when $\geq 10\mu\text{m}$. Therefore, to improve the accuracy of micro-bond test, a certain gap l_g should be kept.

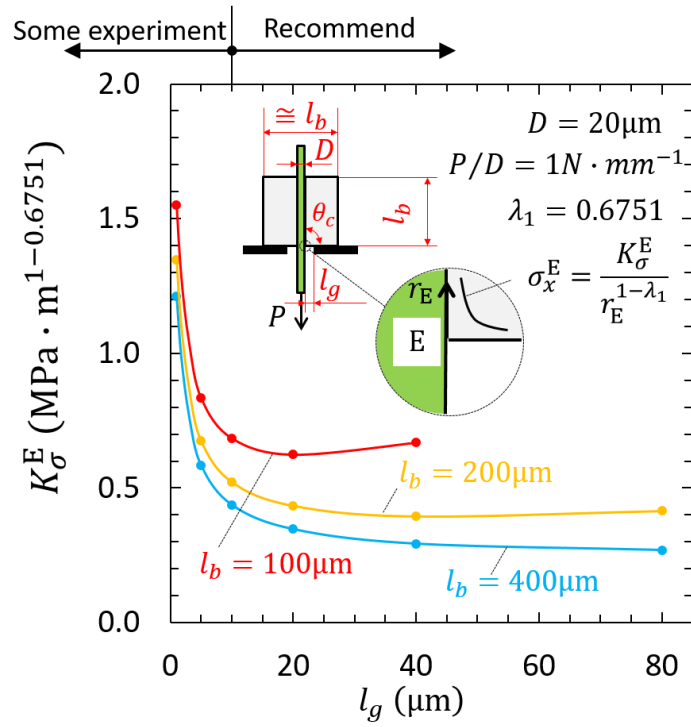


Fig. 4.6(a). ISSF K_{σ}^E variation by varying l_g for Carbon fiber/Epoxy

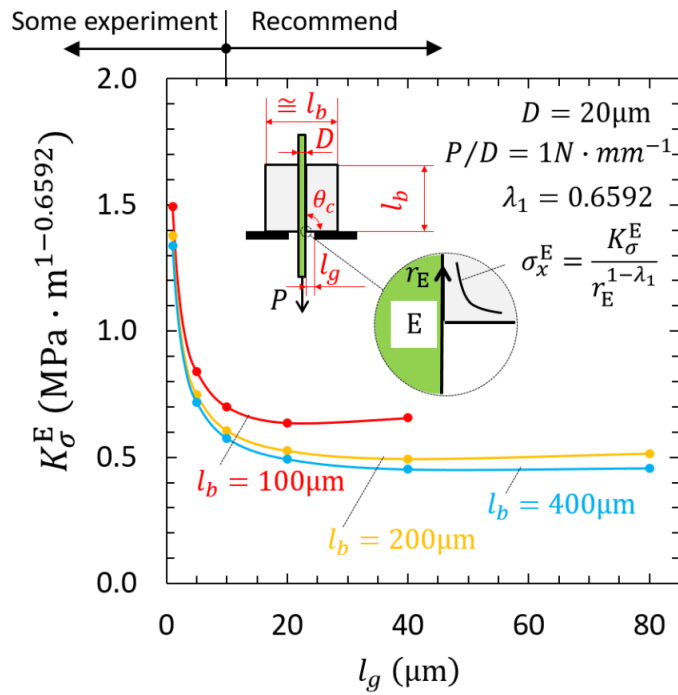


Fig. 4.6(b). ISSF K_{σ}^E variation by varying l_g for Glass fiber/Epoxy

Chapter 4

As shown in Table 4.5 and Fig. 4.7 for Carbon fiber/Epoxy in Table 4.1(a), the ISSF ratio $K_{\sigma}^{E^*}/K_{\sigma}^E$ is investigated. The ISSF ratio $K_{\sigma}^{E^*}/K_{\sigma}^E \cong 0.60$ for Carbon fiber/Epoxy. In other words, the ISSF at Point E in micro-bond test is about 1.66 times of that at Point E* in pull-out test. For Glass fiber/Epoxy, the ISSF ratio $K_{\sigma}^{E^*}/K_{\sigma}^E$ is almost constant as $K_{\sigma}^{E^*}/K_{\sigma}^E \cong 0.75$. In other words, the ISSF at Point E in micro-bond test is about 1.5 times of that at Point E* in pull-out test. In Fig.4.7, both ISSF ratios are nearly constant independent of l_b as $K_{\sigma}^{E^*}/K_{\sigma}^E \cong 0.60 \sim 0.75 \cong 0.66$. The ISSF of pull-out test can be roughly estimated from the ISSF of micro-bond test.

Table 4.4. ISSF variation K_{σ}^E [$MPa \cdot m^{1-0.6751}$] by varying l_g for Carbon fiber/Epoxy. (): $K_{\sigma}^E|_{l_b}/K_{\sigma}^E|_{l_b=100\mu m}$.

l_b [μm]	l_g [μm]	1	5	10	20	40	80
100		1.552	0.834	0.685	0.624	0.669	—
		(1.000)	(1.000)	(1.000)	(1.000)	(1.000)	(—)
200		1.346	0.675	0.523	0.434	0.395	0.415
		(0.867)	(0.809)	(0.763)	(0.696)	(0.591)	(—)
400		1.213	0.583	0.437	0.347	0.293	0.269
		(0.782)	(0.699)	(0.638)	(0.556)	(0.438)	(—)

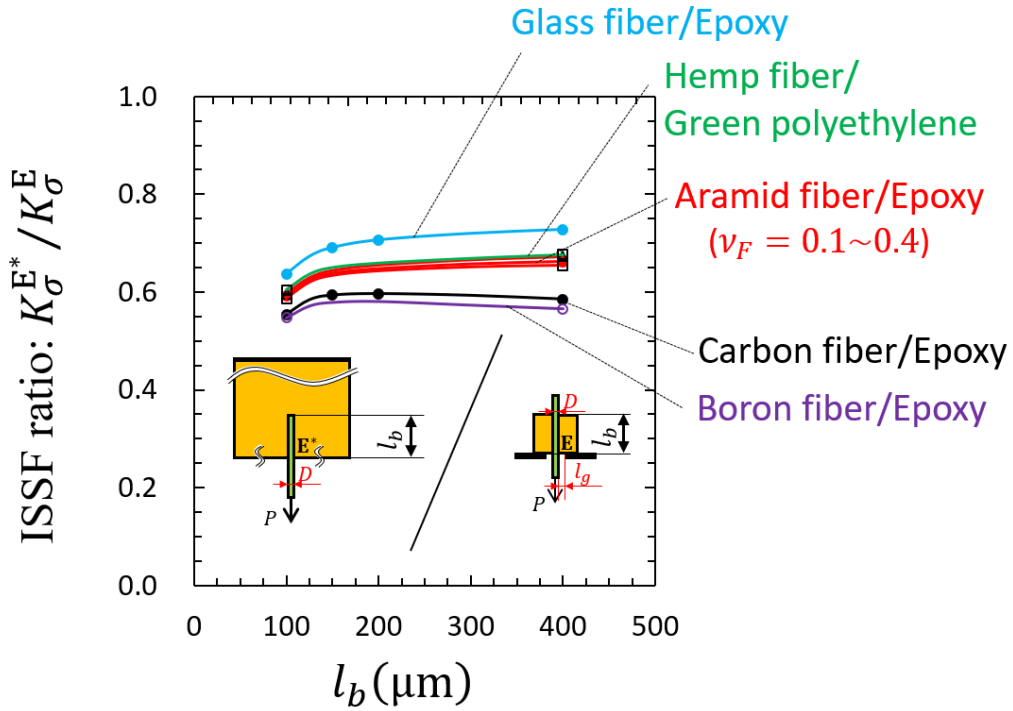


Fig. 4.7. ISSF ratio $K_{\sigma}^{E^*}/K_{\sigma}^E$ of pull-out test and micro-bond test when $l_g = 20\mu\text{m}$

Table 4.5. ISSF K_{σ}^E in micro-bond test when $l_g = 20\mu\text{m}$ and $K_{\sigma}^{E^*}$ in pull-out test of Carbon fiber/Epoxy

l_b [μm]	100	150	200	400
$K_{\sigma}^{E^*} [\text{MPa} \cdot \text{m}^{1-0.6751}]$	0.346	0.291	0.259	0.203
$K_{\sigma}^E [\text{MPa} \cdot \text{m}^{1-0.6751}]$	0.624	0.491	0.434	0.347
$K_{\sigma}^{E^*}/K_{\sigma}^E$	0.554	0.593	0.596	0.585

4.4 ISSFs under Arbitrary Material Combination for a Single Rectangle Fiber in an Infinite Plate Subjected to Remote Tension

In this section, the intensity of singular stress fields (ISSFs) in Fig. 2.2(b) are shown in the $\alpha - \beta$ space. Here, α, β denote Dundurs bimaterial parameters ¹⁵⁾, which are defined by equation (4.1). Here, G_F and G_M are shear modulus, which can be transformed from Young's modulus E_F, E_M and Poisson's Ratios ν_F, ν_M . Subscripts M, F represent the matrix and reinforcing fiber, respectively. In this study, analysis is carried out on the basis of plane

assumption.

$$\left\{ \begin{array}{l} \alpha = \frac{G_F(\kappa_M+1) - G_M(\kappa_F+1)}{G_F(\kappa_M+1) + G_M(\kappa_F+1)} \\ \beta = \frac{G_F(\kappa_M-1) - G_M(\kappa_F-1)}{G_F(\kappa_M+1) + G_M(\kappa_F+1)} \end{array} \right. \kappa_i = \begin{cases} (3 - \nu_i)/(1 + \nu_i) & (\text{Plain stress}) \\ (3 - 4\nu_i) & (\text{Plain strain}) \end{cases} \quad (i = M, F). \quad (4.1)$$

By using the BFM coupled with singular integral equation ^{50),51),55)}, the following ISSFs F_I^* and F_{II}^* at Point A* in Fig. 2.2(b) can be calculated. Here, the fiber's total length is fixed as the aspect ratio $l/D = 10$. For the material combination (a) in Table 4.1, the convergency of the solution is shown in Table 4.6 by varying the number of collocation M increasing the order of polynomial approximation at each boundary division. Four digits accuracy can be seen. The normalized ISSFs in Fig. 2.2(b) defined by equation (2.5) are shown in Table 4.7 and Fig. 4.8 under arbitrary material combination.

Singular indexes λ_1^A and λ_2^A around the corner A and corner A* can be calculated by solving equations (4.2a) and (4.2b) on λ , respectively ^{50),55)}.

Here, the singular indexes λ_1^A and λ_2^A have real values in the range $0 < \text{Re}(\lambda_i^A) < 1$ if $\beta(\alpha - \beta) > 0$. In equations (4.2), we can put $\gamma = \pi/2$ representing the angle between interfaces r_1 and r_2 .

$$\begin{aligned} D_1(\alpha, \beta, \gamma, \lambda) = & (\alpha - \beta)^2 \lambda^2 [1 - \cos(2\gamma)] - 2\lambda(\alpha - \beta) \sin(\gamma) \{ \sin(\lambda\gamma) + \sin[\lambda(2\pi - \gamma)] \} \\ & + 2\lambda(\alpha - \beta) \beta \cdot \sin(\gamma) \{ \sin[\lambda(2\pi - \gamma)] - \sin(\lambda\gamma) \} \\ & + (1 - \alpha^2) - (1 - \beta^2) \cos(2\lambda\pi) + (\alpha^2 - \beta^2) \cos[2\lambda(\gamma - \pi)] = 0 \end{aligned} \quad (4.2a)$$

$$\begin{aligned} D_2(\alpha, \beta, \gamma, \lambda) = & (\alpha - \beta)^2 \lambda^2 [1 - \cos(2\gamma)] + 2\lambda(\alpha - \beta) \sin(\gamma) \{ \sin(\lambda\gamma) + \sin[\lambda(2\pi - \gamma)] \} \\ & - 2\lambda(\alpha - \beta) \beta \cdot \sin(\gamma) \{ \sin[\lambda(2\pi - \gamma)] - \sin(\lambda\gamma) \} \\ & + (1 - \alpha^2) - (1 - \beta^2) \cos(2\lambda\pi) + (\alpha^2 - \beta^2) \cos[2\lambda(\gamma - \pi)] = 0 \end{aligned} \quad (4.2b)$$

Table 4.6. Convergence of the ISSFs in Fig. 2.2(b) for the material combination in Table 4.1(a)

M	F_I^*	F_{II}^*
8	0.6780	1.132
7	0.6782	1.133
6	0.6780	1.133
5	0.6783	1.130

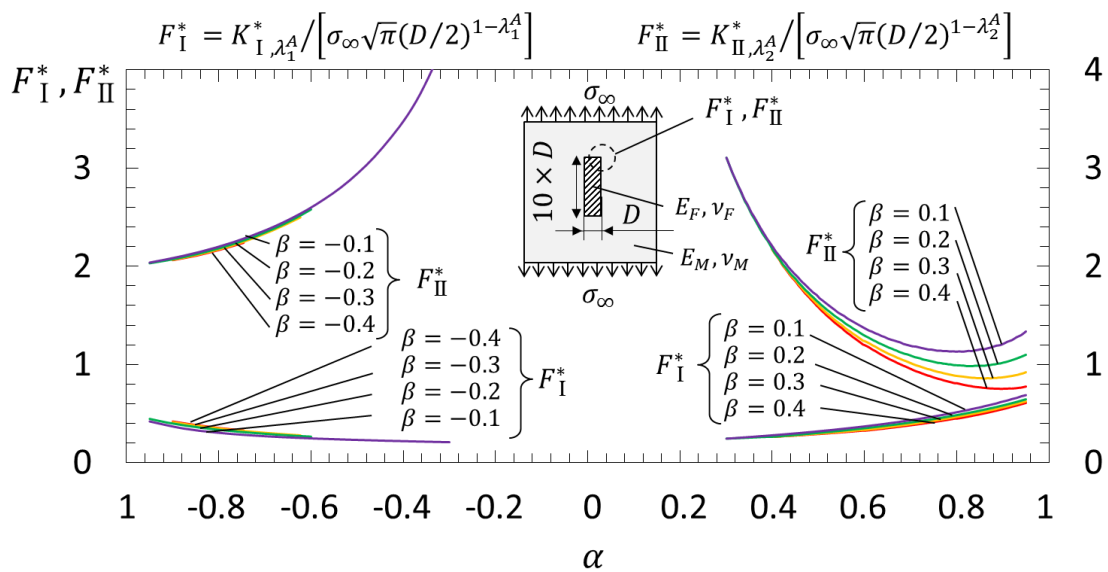


Fig. 4.8 ISSFs for a Single Rectangle Fiber in an Infinite Plate Subjected to Remote Tension in Fig. 2.2(b)

Table 4.7(a). F_I^* for a Single Rectangle Fiber in an Infinite Plate Subjected to Remote Tension in Fig. 2.2(b)

	$\alpha = 0.9$	0.8	0.7	0.6	0.5	0.4	0.3
$\beta = 0.1$	0.623	0.513	0.434	0.370	0.322	0.280	0.245
$\beta = 0.2$	0.584	0.484	0.412	0.353	0.304	0.265	-
$\beta = 0.3$	0.563	0.469	0.393	0.334	0.297	-	-
$\beta = 0.4$	0.547	0.449	0.382	-	-	-	-

Table 4.7(b). F_{II}^* for a Single Rectangle Fiber in an Infinite Plate Subjected to

Remote Tension in Fig. 2.2(b)							
	$\alpha = 0.9$	0.8	0.7	0.6	0.5	0.4	0.3
$\beta = 0.1$	1.208	1.131	1.189	1.371	1.675	2.198	3.106
$\beta = 0.2$	1.019	0.993	1.086	1.290	1.629	2.141	-
$\beta = 0.3$	0.870	0.883	1.014	1.240	1.598	-	-
$\beta = 0.4$	0.753	0.810	0.955	-	-	-	-

4.5 ISSFs under Arbitrary Material Combination for a Single Fiber Subjected to Pull-out Force from a Semi-Infinite Plate

In this section, the ISSFs in Fig. 2.2(a) at the fiber buried end under pull-out are shown in the $\alpha - \beta$ space. The fiber embedding length is fixed as $l_{in}/D = 5$. Tables 4.8.a, 4.8.b and Fig. 4.9 show the ISSF ratios for Fig. 2.2(a) and (b) obtained by using the proportional method explained in Chapter 2. Table 4.9 and Fig. 4.10 show the normalized ISSFs at Point A in Fig. 2.2(a) calculated from the ISSF ratios and the ISSFs at Point A* shown in Fig. 4.8.

Table 4.8(a). F_I / F_I^* when $l_{in}/D = 5$ in Fig. 2.2(a) and $l/D = 10$ in Fig. 2.2(b)

	$\alpha = 0.9$	0.8	0.7	0.6	0.5	0.4	0.3
$\beta = 0.1$	0.0864	0.111	0.128	0.139	0.145	0.146	0.143
$\beta = 0.2$	0.0862	0.108	0.122	0.130	0.133	0.132	-
$\beta = 0.3$	0.0851	0.105	0.116	0.122	0.123	-	-
$\beta = 0.4$	0.0832	0.100	0.110	-	-	-	-

Table 4.8(b). F_{II} / F_{II}^* when $l_{in}/D = 5$ in Fig. 2.2(a) and $l/D = 10$ in Fig. 2.2(b)

	$\alpha = 0.9$	0.8	0.7	0.6	0.5	0.4	0.3
$\beta = 0.1$	0.0766	0.0935	0.104	0.111	0.115	0.118	0.119
$\beta = 0.2$	0.0760	0.0928	0.103	0.109	0.113	0.115	-
$\beta = 0.3$	0.0749	0.0915	0.101	0.107	0.111	-	-
$\beta = 0.4$	0.0733	0.0895	0.0991	-	-	-	-

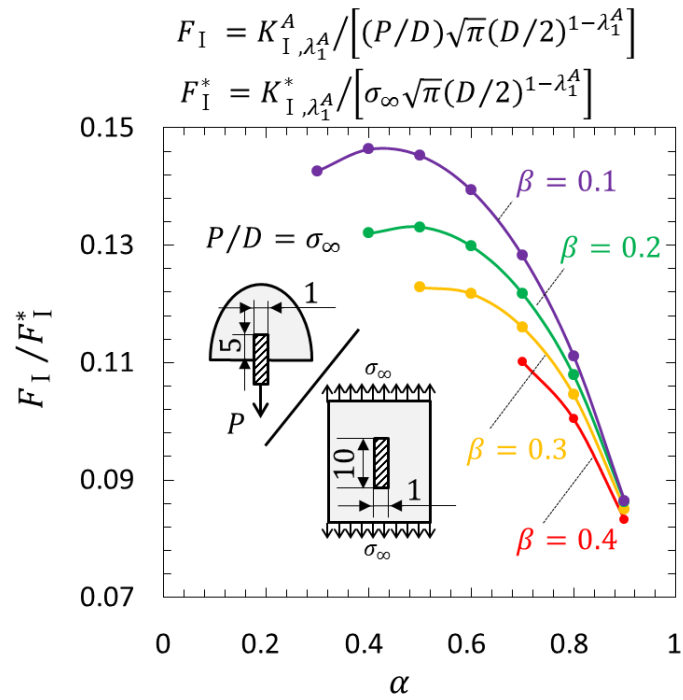


Fig. 4.9(a). FEM stress ratio

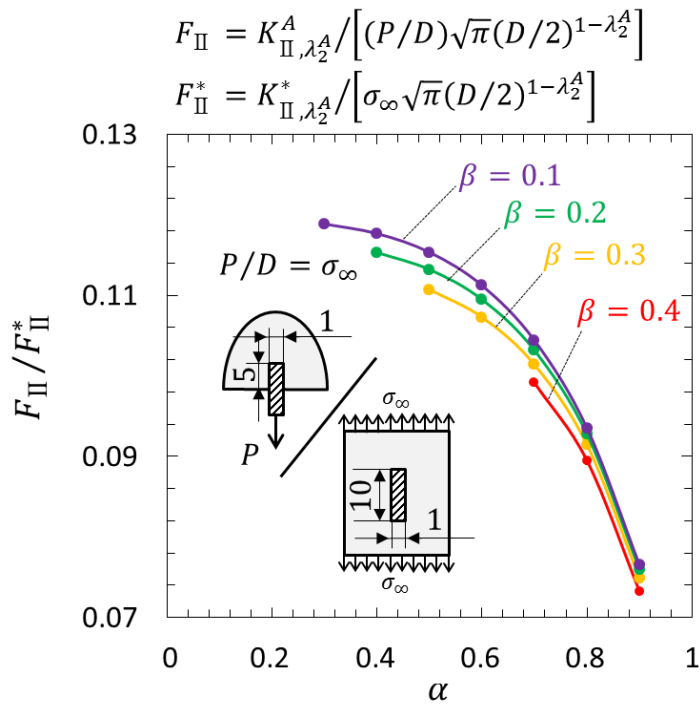


Fig. 4.9(b) FEM stress ratio

Chapter 4

Table 4.9(a). F_I when $l_{in}/D = 5$ in Fig. 2.2(a).

	$\alpha=0.9$	0.8	0.7	0.6	0.5	0.4	0.3
$\beta = 0.1$	0.05384	0.05707	0.05569	0.05163	0.04673	0.04099	0.03502
$\beta = 0.2$	0.05032	0.05220	0.05019	0.04579	0.04052	0.03501	-
$\beta = 0.3$	0.04792	0.04898	0.04562	0.04065	0.03644	-	-
$\beta = 0.4$	0.04553	0.04511	0.04209	-	-	-	-

Table 4.9(b). F_{II} when $l_{in}/D = 5$ in Fig. 2.2(a).

	$\alpha=0.9$	0.8	0.7	0.6	0.5	0.4	0.3
$\beta = 0.1$	0.09249	0.10581	0.12418	0.15250	0.19326	0.25863	0.36925
$\beta = 0.2$	0.07743	0.09214	0.11202	0.14115	0.18444	0.24687	-
$\beta = 0.3$	0.06516	0.08079	0.10280	0.13304	0.17696	-	-
$\beta = 0.4$	0.05519	0.07249	0.09466	-	-	-	-

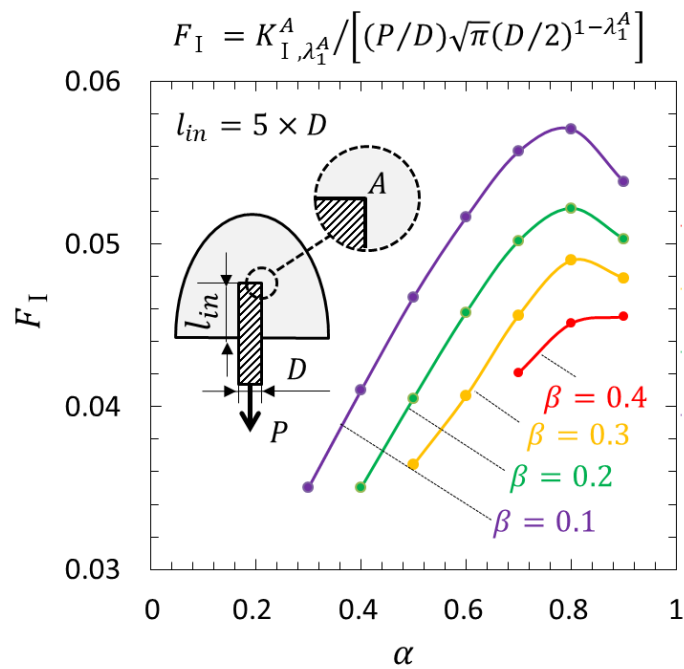


Fig. 4.10(a). F_I when $l_{in}/D = 5$ in Fig. 2.2(a)

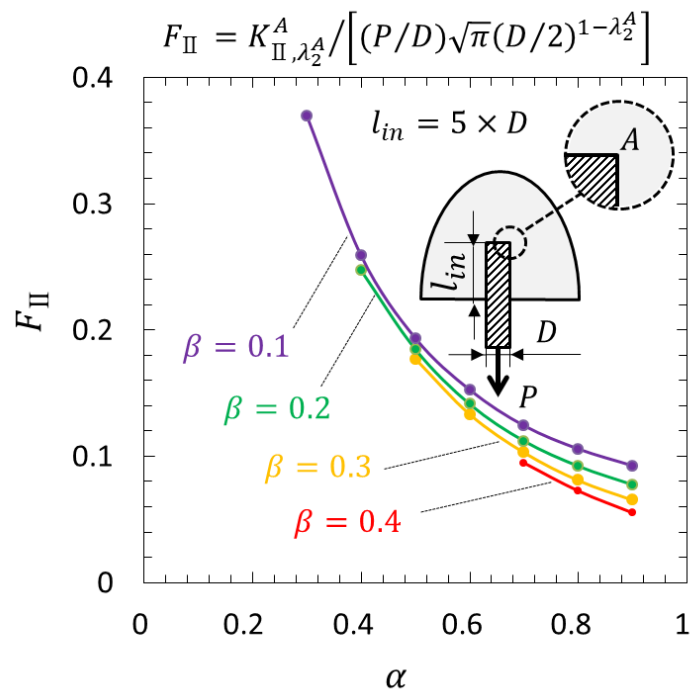


Fig. 4.10(b). F_{II} when $l_{in}/D = 5$ in Fig. 2.2(a).

4.6 Conclusions

The ISSFs in pull-out test and micro-bond test are studied for the material combination of Carbon fiber/Epoxy. For pull-out test, the buried fiber end Point A is easier to debond if the bonded length is short. The fiber entry Point E is easier to debond if the bonded length is long. This is same to Carbon fiber/Epoxy and Glass fiber/Epoxy. The ISSF ratio between pull-out test and micro-bond test is within range of 0.55~0.75, which is almost constant for different materials and independent of bonded length. Therefore, the results of pull-out test can be predicted from that of micro-bond test, if same material combination and fiber bonded length are used.

Chapter 5 Conclusions.

In fiber reinforced composites, both the fiber and the matrix retain their original physical and chemical identities, yet together they produce a combination of mechanical properties that cannot be achieved with either of the constituents acting alone. Pull-out test and Micro-bond test are most widely used to gain more insight into the properties of the fiber/matrix interface. However, among those previous studies the singular stress fields have not been considered. In this study, therefore, a partially-embedded single-fiber under pull-out force was analyzed focusing on two distinct singular stress fields appearing at fiber end and entry points in comparison with micro-bond test. Then, the following conclusions were obtained.

(1) In pull-out test, the mixed-mode ISSFs at the fiber end denoted by K_{σ,λ_1}^A , K_{σ,λ_2}^A decrease with increasing the fiber embedded length l_{in} . Under fixed fiber length $l = 600 \mu\text{m}$, the ISSFs at $l_{in} = (1/2)l$ is about 30% smaller than the ISSFs at $l_{in} = (1/4)l$ for carbon fiber/epoxy, and the ISSFs at $l_{in} = (1/2)l$ is about 40% smaller than the ISSFs at $l_{in} = (1/4)l$ for glass fiber/epoxy.

(2) In pull-out test, the two ISSFs denoted by K_{σ,λ_1}^E , K_{σ,λ_2}^E at the fiber entry point decrease with increasing the fiber embedded length l_{in} . For example, the ISSFs at $l_{in} = (1/2)l$ is about 20% smaller than at $l_{in} = (1/4)l$ for carbon fiber/epoxy. The ISSFs at $l_{in} = (1/2)l$ is about 10% smaller than the ISSFs at $l_{in} = (1/4)l$ for glass fiber/epoxy. The ISSF decreasing rate at Point E becomes smaller than that at Point A especially when l_{in} is large.

(3) In pull-out test, the severities were compared at the fiber end and fiber entry point by focusing on the stress just $1 \mu\text{m}$ away from the singular point by varying l_{in} (see Fig. 4.5). For carbon fiber/epoxy, the severities at the fiber end and fiber entry point are almost the same when $l_{in} = 450\mu\text{m}$. For glass fiber/epoxy, the severities are almost the same when $l_{in} = 125\mu\text{m}$. For shorter embedded length, the buried fiber end becomes more dangerous.

(4) In micro-bond test, no matter how the fiber bond length l_b changes, the fiber entry point

is more dangerous in micro-bond test. Instead, in fiber pull-out test, the fiber end point can be more dangerous if the embedded length is shorter. The ISSF at the entry point in micro-bond test is about 1.5 times of the ISSF of pull-out test at the entry point under the same geometries D and l_b . By using this knowledge, the ISSFs of pull-out test can be predicted from micro-bond test.

(5) In micro-bond test, care should be taken for the small knife gap opening $l_g \leq 10\mu\text{m}$ popularly used because the ISSF K_σ^E is sensitive to l_g . Instead, testing geometry $l_g \geq 10\mu\text{m}$ can be recommended since the ISSF K_σ^E is nearly independent of l_g .

(6) Reference solution coupled with proportional method were indicated to calculate the ISSF conveniently for various fiber with other geometries.

Reference

Reference

- 1) Q. Wu, M. Li, Y. Gu, Y. Li and Z. Zhang, *Compos. Part A Appl. Sci. Manuf.* 56, 143 (2014).
- 2) F. Teklal, A. Djebbar, S. Allaoui, G. Hivet, Y. Joliff and B. Kacimi, *Compos. Struct.* 201, 791 (2018).
- 3) B. Banholzer, W. Brameshuber and W. Jung, *Cem. Concr. Compos.* 28 [6], 564 (2006).
- 4) H. Ho and L. T. Drzal, *Compos. Part A Appl. Sci. Manuf.* 27 [10], 961 (1996).
- 5) N.-A. Noda, T. Miyazaki, T. Uchikoba, R. Li, Y. Sano and Y. Takase, *J. Japan Inst. Electron. Packag.* 17 [2], 132 (2014).
- 6) Y. Suzuki, *JSME Int. J.* 30 [265], 1042 (1987).
- 7) N.-A. Noda, T. Miyazaki, R. Li, T. Uchikoba, Y. Sano and Y. Takase, *Int. J. Adhes. Adhes.* 61, 46 (2015).
- 8) T. Miyazaki, N.-A. Noda, F. Ren, Z. Wang, Y. Sano and K. Iida, *Int. J. Adhes. Adhes.* 77, 118 (2017).
- 9) N.-A. Noda, F. Ren, R. Takaki, Z. Wang, K. Oda, T. Miyazaki and Y. Sano, *Int. J. Adhes. Adhes.* 85, 234 (2018).
- 10) T. Miyazaki, N.-A. Noda, Z. Wang and Y. Sano, *Trans. JSME (in Japanese)* 81 [829], 15 (2015).
- 11) N.-A. Noda, R. E. N. Fei, R. Takaki, K. Tsuboi, Y. Sano, Y. Takase and T. Miyazaki, *J. Japan Inst. Electron. Packag.* 21 [4], 299 (2018).
- 12) T. Miyazaki, N.-A. Noda and Y. Sano, *J. Japan Inst. Electron. Packag.* 21 [2], 166 (2018).
- 13) D. B. Bogy, *J. Appl. Mech. Trans. ASME* 35 [3], 460 (1964).
- 14) D. B. Bogy, *J. Appl. Mech. Trans. ASME* 38 [2], 377 (1971).
- 15) J. Dundurs, *J. Compos. Mater.* 1 [3], 310 (1967).
- 16) N.-A. Noda, X. Chen, Y. Sano, M. A. Wahab, H. Maruyama, R. Fujisawa and Y. Takase,

Reference

- Mater. Des. 96, 476 (2016).
- 17) N.-A. Noda, R. Takaki, Y. Shen, A. Inoue, Y. Sano, D. Akagi, Y. Takase and P. Galvez, Mech. Mater. 131, 141 (2019).
- 18) Z. Wang, N.-A. Noda, M. Ueno and Y. Sano, Steel Res. Int. [DOI:10.1002/srin.201600353].
- 19) M. Stern and M. L. Soni, Int. J. Solids Struct. 12 [5], 331 (1976).
- 20) C. Atkinson, J. Avila, E. Betz and R. E. Smelser, J. Mech. Phys. Solids 30 [3], 97 (1982).
- 21) G. L. Povirk and A. Needleman, J. Eng. Mater. Technol. Trans. ASME 115 [3], 286 (1993).
- 22) L. B. Freund, Eur. J. Mech. A/Solids 11 [1], 1 (1992).
- 23) X. Zhang, H.-Y. Liu and Y.-W. Mai, Compos. Part A Appl. Sci. Manuf. 35 [11], 1313 (2004).
- 24) J. W. Hutchinson and H. M. Jensen, Mech. Mater. 9 [2], 139 (1990).
- 25) K. Oda, K. Kamisugi and N. A. Noda, Nihon Kikai Gakkai Ronbunshu, A Hen/Trans Japan Soc. Mech. Eng. Part A 75 [752], 476 (2009).
- 26) W. C. Carpenter and C. Byers, Int. J. Fract. 35 [4], 245 (1987).
- 27) G. B. Sinclair, M. Okajima and J. H. Griffin, Int. J. Numer. Methods Eng. 20 [6], 999 (1984).
- 28) M. L. Williams, Bull. Seismol. Soc. Am. 49 [2], 199 (1959).
- 29) W. C. Carpenter, Int. J. Fract. 26 [3], 201 (1984).
- 30) M. Stern, E. B. Becker and R. S. Dunham, Int. J. Fract. 12 [3], 359 (1976).
- 31) D.-H. Chen and H. Nisitani, J. Appl. Mech. Trans. ASME 60 [3], 607 (1993).
- 32) D.-H. Chen and H. Nisitani, Trans. Japan Soc. Mech. Eng. Ser. A 58 [547], 457 (1992).
- 33) N.-A. Noda, R. Li, T. Miyazaki, R. Takaki and Y. Sano, Int. J. Comput. Methods

Reference

- [DOI:10.1142/S0219876218500858].
- 34) R. J. Scheer and J. A. Nairn, *J. Adhes.* 53 [1–2], 45 (1995).
- 35) E. Pisanova, S. Zhandarov, E. Mäder, I. Ahmad and R. J. Young, *Compos. Part A Appl. Sci. Manuf.* 32 [3–4], 435 (2001).
- 36) S. Zhandarov and E. Mäder, *Compos. Sci. Technol.* 65 [1], 149 (2005).
- 37) C. Marotzke and L. Qiao, *Compos. Sci. Technol.* 57 [8], 887 (1997).
- 38) C. Wang, *J. Mater. Sci.* 32 [2], 483 (1997).
- 39) K.-H. Tsai and K.-S. Kim, *J. Mech. Phys. Solids* 44 [7], 1147 (1996).
- 40) K. Goda, *Nihon Kikai Gakkai Ronbunshu, A Hen/Trans Japan Soc. Mech. Eng. Part A* 66 [643], 480 (2000).
- 41) J. M. Hedgepeth and P. Van Dyke, *J. Compos. Mater.* 1 [3], 294 (1967).
- 42) S. B. Batdorf, *Eng. Fract. Mech.* 18 [6], 1207 (1983).
- 43) B. Budiansky, A. G. Evans and J. W. Hutchinson, *Int. J. Solids Struct.* 32 [3–4], 315 (1995).
- 44) N.-A. Noda, D. Chen, R. Takaki, A. Inoue, G. Zhang and Y. Sano, *Zair. Soc. Mater. Sci. Japan* 67 [12], 1073 (2018).
- 45) Y. Zhang, N.-A. Noda, P. Wu and M. Duan, *Int. J. Adhes. Adhes.* 57 [March], 105 (2015).
- 46) H. Nisitani and T. Teranishi, *Struct. Mater.*, 2000, 6, 461–469.
- 47) H. Nisitani and T. Teranishi, *Eng. Fract. Mech.* 71 [4–6], 579 (2004).
- 48) T. Miyazaki, *Trans. Soc. Automot. Eng. Japan* 45 [5], 895 (2014).
- 49) T. Miyazaki and N.-A. Noda, in *Journal of Physics: Conference Series* (2017) Vol. 842.
- 50) N.-A. Noda, R. Shirao, J. Li and J.-S. Sugimoto, *Int. J. Solids Struct.* 44 [13], 4472 (2007).
- 51) N.-A. Noda, Q. Wang, Y. Uemura and Y. Kawashima, *JSME Int. Journal, Ser. A Mech. Mater. Eng.* 41 [3], 303 (1998).

Reference

- 52) N.-A. Noda, Y. Takase and T. Iizuka, *Nihon Kikai Gakkai Ronbunshu, A Hen/Transactions Japan Soc. Mech. Eng. Part A* 71 [8], 1132 (2005).
- 53) T. Suga, G. Elssner and S. Schmauder, *J. Compos. Mater.* 22 [10], 917 (1988).
- 54) R. Yuuki, *Mechanics of Interface* (1993).
- 55) D.-H. Chen and H. Nisitani, *Trans. Japan Soc. Mech. Eng. Ser. A* 58 [555], 2153 (1992).
- 56) L. P. Hann and D. E. Hirt, *Compos. Sci. Technol.* 54 [4], 423 (1995).
- 57) J. T. Ash, W. M. Cross, D. Svalstad, J. J. Kellar and L. Kjerengtroen, *Compos. Sci. Technol.* 63 [5], 641 (2003).
- 58) H. Brito-Santana, J. L. M. Thiesen, R. de Medeiros, A. J. M. Ferreira, R. Rodríguez-Ramos and V. Tita, *Appl. Math. Model.* 75, 250 (2019).
- 59) M. Ranjbarian, V. Mechtcherine, Z. Zhang, I. Curosu, J. Storm and M. Kaliske, *Cem. Concr. Compos.* 103, 318 (2019).
- 60) J. Storm, M. Ranjbarian, V. Mechtcherine, C. Scheffler and M. Kaliske, *Theor. Appl. Fract. Mech.* [DOI:10.1016/j.tafmec.2019.102294].
- 61) J. M. Vázquez-Rodríguez, E. A. Flores-Johnson, P. J. Herrera-Franco and P. I. Gonzalez-Chi, *Polym. Compos.* 39, E2397 (2018).
- 62) M. Frikha, H. Nouri, S. Guessasma, F. Roger and C. Bradai, *J. Mater. Sci.* 52 [24], 13829 (2017).
- 63) J. Serra, C. Bouvet, B. Castanié and C. Petiot, *Compos. Struct.* 181, 145 (2017).
- 64) Z. Poniznik, Z. Nowak and M. Basista, *Int. J. Damage Mech.* 26 [5], 711 (2017).
- 65) S. I. Kundalwal and S. Kumar, *Mech. Mater.* 102, 117 (2016).
- 66) B. K. Paul, K. Ahmed, D. Vigneswaran, F. Ahmed, S. Roy and D. Abbott, *IEEE Sens. J.* 18 [24], 9948 (2018).
- 67) M. A. Jabin, K. Ahmed, M. J. Rana, B. K. Paul, M. Islam, D. Vigneswaran and M. S.

Reference

- Uddin, IEEE Photonics J. [DOI:10.1109/JPHOT.2019.2924825].
- 68) K. Ahmed, M. J. Haque, M. A. Jabin, B. K. Paul, I. S. Amiri and P. Yupapin, Phys. B Condens. Matter 570, 48 (2019).
- 69) K. Ahmed, B. K. Paul, M. A. Jabin and B. Biswas, Ceram. Int. 45 [12], 15343 (2019).
- 70) B. K. Paul, S. Chakma, M. A. Khalek and K. Ahmed, Chinese J. Phys. 56 [6], 2782 (2018).
- 71) T. Miyazaki, N.-A. Noda, R. Li, T. Uchikoba and Y. Sano, J. Japan Inst. Electron. Packag. 16 [2], 143 (2013).
- 72) N. Noda, D. Chen, G. Zhang and Y. Sano, Int. J. Mech. Sci. 165 [August 2019], 105196 (2020).
- 73) C. Baley, Y. Grohens, F. Busnel and P. Davies, Appl. Compos. Mater. 11 [2], 77 (2004).
- 74) B. Miller, P. Muri and L. Rebenfeld, Compos. Sci. Technol. 28 [1], 17 (1987).
- 75) S.-L. Gao, E. Mäder and S. F. Zhandarov, Carbon N. Y. 42 [3], 515 (2004).
- 76) R. Li, N.-A. Noda, R. Takaki, Y. Sano, Y. Takase and T. Miyazaki, Int. J. Adhes. Adhes. 86, 45 (2018).
- 77) C. T. Chou, U. Gaur and B. Miller, Compos. Sci. Technol. 51 [1], 111 (1994).
- 78) R. A. Latour, J. Black and B. Miller, Surf. Interface Anal. 17 [7], 477 (1991).
- 79) V. Rao, P. Herrera-Franco, A. D. Ozzello and L. T. Drzal, J. Adhes. 34 [1–4], 65 (1991).